CHARACTERIZING URBAN HEAT ISLAND AND ITS EFFECTS IN HONG KONG

FUNG WING-YEE

Ph.D.

THE HONG KONG
POLYTECHNIC UNIVERSTIY

2010

The Hong Kong Polytechnic University

Department of Civil and Structural Engineering

CHARACTERIZING URBAN HEAT ISLAND AND ITS EFFECTS IN HONG KONG

FUNG Wing Yee

A thesis submitted in partial fulfillment of
the requirements for the degree of
Doctor of Philosophy

June 2010

CERTIFICATE OF ORGINALITY

I hereby declare that this thesis is my own work and that, to the best of my knowledge and belief, it reproduces no material previously published or written, nor material that has been accepted for the award of any other degree or diploma, except where due acknowledgement has been made in the text.

__________________________________ (Signed)

FUNG Wing Yee (Name of student)

ABSTRACT

Urban Heat Island (UHI) becomes a big concern, especially in a subtropical region. UHI not only changes the environment but also affect human life. More energy consumption, high disease transmission rate, and poor air quality are the possible consequences of heat island. In this study, four approaches were employed to 1) investigate the existence of heat island effect, 2) explore a linkage between atmospheric and surface heat island studies and 3) examine the impact on heat budget due to a land cover change.

The four adopted approaches were mobile transverse measurements, a remote sensing technique, fixed station method and a 1-dimensional heat budget measurement. First, a series of 20 mobile transverse measurements were conducted in 2003 – 2005. Two vehicles with temperature sensors installed were employed to be driven mainly in urban areas in order to quantify heat island intensity. Second, four satellite images were captured in a night of winter, a day of winter, a night of summer and a day of summer in year 2007 and 2008. A ground mobile in-situ temperature measurement team was simultaneously conducted when the satellite passed over Hong Kong in order to explore the temperature correlation between atmospheric and surface heat island intensities. Third, a long-term UHI intensity between two fixed stations was analyzed for 19 years (1989 – 2007). The characteristic of UHI in a subtropical city was generalized based on the data from two typical meteorological stations. Fourth, a 1-year intensive heat budget measurement was conducted at Ta Kwu Ling in 2007/2008. A comparison of heat flux of net radiation, soil heat, sensible heat and latent heat was made over grass and concrete surfaces.

There are three key contributions: (1) the characteristic of heat island in Hong Kong, (2) a useful tool for converting satellite-derived temperature to ambient temperatures and (3) impacts on heat budget, emissivity and albedo when a land cover changes from grass to concrete surfaces. Regarding the characteristic of heat island, both diurnal and seasonal variations of average heat island intensity were demonstrated. The average of daily maximum heat island intensity was around 2.7^{o}C. One hourly maximum heat island intensity of 11.5^{o}C occurred in

the early morning of winter which agreed with the surface temperature measurement results. This finding suggests that topography and urban design can contribute to heat island effect in a subtropical city.

A useful tool for converting satellite-derived temperature to ambient temperatures in a winter night was introduced. A good correlation between nighttime surface temperatures and nighttime ambient temperatures was found. Two empirical equations in urban and suburban areas were generated and these equations were recommended to apply in surface heat island studies in future case studies on winter night.

The last key findings is that a land cover changing from grass surface to concrete surface can cause an significant increase in sensible heat on clear sky days, a reduction in emissivity value by at least 6.4%, a decrease in albedo by around 6% during hot seasons and an increase in albedo by about 27% during cold seasons.

Overall, the findings of this study were able to examine the characteristic of heat island intensity in Hong Kong and justify the impact of a land surface change on heat budget, albedo and emissivity. Further research studies are recommended to fill the gaps of heat island studies.

PUBLICATIONS ARISING FROM THE THESIS

W.Y. Fung, K.S. Lam, Janet Nichol, Man Sing Wong, Derivation of night time urban air temperatures using a satellite thermal image, Journal of Applied Meteorology and Climatology, Volume 48, Issue 4, April 2009, Pages 863-872.

Janet E Nichol, **W.Y. Fung**, K.S. Lam, Man Sing Wong, Urban heat island diagnosis using ASTER satellite images and "in situ" air temperature, Atmospheric Research, Volume 94, Issue 2, October 2009, Pages 276-284.

W.Y. Fung, K.S. Lam, Edwin Ginn, Y.W. Chan, Net Radiation and albedo study at Ta Kwu Ling, Hong Kong Meteorological Society Bulletin (in press).

W.Y. Fung, K.S. Lam, Characterizing the urban heat island intensity in Hong Kong, Proceedings of the 10th International Conference on Atmospheric Sciences and Applications of Air Quality (ASAAQ 2007), Hong Kong, PRC, 14-16 May 2007.

W.Y. Fung, K.S. Lam, Impact of urbanization on temperature trend. Proceedings of 8th Annual Meeting of the EMS / 7th ECAC, 29 September – 3 October 2008.

W.Y. Fung, K.S. Lam. Exploring heat island study in a subtropical city, 2010 Western Pacific Geophysics Meeting, Taipei, Taiwan, 22-25 June 2010.

W.Y. Fung, Liu Qian, K.S. Lam. Heat flux measurement in Hong Kong, 2010 Western Pacific Geophysics Meeting, Taipei, Taiwan, 22-25 June 2010.

ACKNOWLEDGEMENTS

I would like to express my deepest gratitude to my supervisor Dr. K.S. Lam for his invaluable guidance and patient. I would also thank him for offering insightful inputs and constructive criticisms during my wiring up process. Without his understanding, encouragement, and continuous support, this project would not have been completed.

I would also like to thank my Co-supervisor Dr. W.T. Hung for his support.

I also want to sincerely thank Hong Kong Observatory and the Agriculture, Fisheries and Conservation Department of HKSAR for the provision of experimental sites and electricity supply for the heat budget measurement at Ta Kwu Ling.

A special thank must be given to Mr. Steven Poon and Mr. Cheung Chi Fai of The Hong Kong Polytechnic University for their assistance of an instrument set-up at Ta Kwu Ling.

I also want to express my gratitude for my colleagues and students of The Hong Kong Polytechnic University, particularly Dr. Wei Xiaolin and Mr. Olympian Kwok, for their assistance in conducting the field measurements.

Last but not least, I need to thank to my families and friends, for their moral and financial supports.

TABLE OF CONTENTS

LIST OF FIGURES

TABLE OF FIGURES

Nomenclature

Symbol	Description	Unit
C_a	Heat capacity of air	$Jm^{-3}K^{-1}$
C_{soil}	Heat capacity of soil surface layer	$Jm^{-3}K^{-1}$
$\frac{\partial\overline{\theta}}{\partial z}$	Change rate of the potential temperature	Km^{-1}
$\frac{\partial\overline{\rho}_v}{\partial z}$	Change rate of the vapor concentration	kgm^{-4}
$\frac{\partial\overline{T}_s}{\partial z}$	Change rate of the soil temperature	Km^{-1}
ε	Emissivity values of land cover	
E	Annual electricity consumption at specific year	TJ
k_s	Thermal conductivity of the soil	$Wm^{-1}K^{-1}$
K_H	Eddy conductivity of air temperature	m^2s^{-1}
K_v	Eddy conductivity of water vapor	m^2s^{-1}
L_λ	Spectral radiance used in thermal images	$W\ sr^{-1}m^{-2}$
L_v	Latent heat of vaporization	$K\ m^{-1}$
s	Soil moisture content	%
$T_{insitu,suf}$	In-situ surface temperatures	^oC
$T_{insitu,air}$	In-situ air temperatures	^oC
ΔT_{soil}	Temperature change in the measurement surface layer	K
$T_{180,c}$	Ambient temperature 1.8 m above the concrete ground	^oC
$T_{180,g}$	Ambient temperature 1.8 m above the grass ground	^oC
$T_{20,g}$	Ambient temperature 0.2 m above the grass ground	^oC
$T_{20,c}$	Ambient temperature 0.2 m above the concrete ground	^oC
$T_{0,c}$	Concrete temperature at the concrete ground	^oC
$T_{-5,g}$	Soil temperature 0.05 m below the grass ground	^oC
$T_{-15,c}$	Concrete temperature 0.15 m below the concrete ground	^oC
$T_{-20,g}$	Soil temperature 0.2 m below the grass ground	^oC
$T_{-20,c}$	Soil temperature 0.05 m below the concrete surface layer	^oC
$T_{-35,c}$	Soil temperature 0.2 m below the concrete surface layer	^oC
$T_{-50,g}$	Soil temperature 0.5 m below the grass ground	^oC
$T_{-65,c}$	Soil temperature 0.5 m below the concrete surface layer	^oC
$T_{-125,g}$	Soil temperature 1.25 m below the grass ground	^oC

$T_{-140,c}$	Soil temperature 1.25 m below the concrete surface layer	^{o}C
T_b	Black body temperature	K
Tc	Temperature adjustment due to calibration	^{o}C
$T_{d,i}$	Temperature adjustment due to diurnal variation	^{o}C
$T_{HKO,i}$	Temperature reading at HKO station at measured time i	^{o}C
$T_{HKO,k}$	Temperature reading at HKO station at reference time k	^{o}C
Tm	Air temperature measured by the vehicles	^{o}C
$T_{mean,HKO}$	Annual mean of daily mean temperature at HKOH	^{o}C
$T_{min,HKO}$	Annual mean of daily minimum temperature at HKOH	^{o}C
$T_{min,y}$	Annual mean of daily minimum temperature	^{o}C
$T_{sat,air}$	Satellite-derived air temperatures	^{o}C
$T_{sat,suf}$	Satellite-derived surface temperatures	^{o}C
Tr	Air temperatures in reference areas	^{o}C
Tu	Air temperatures in urban areas	^{o}C
Pop	Annual population in thousand	
Q*	Net all-wave radiation flux density	Wm^{-2}
Q_E	Latent heat flux density	Wm^{-2}
Q_H	Sensible heat flux density	Wm^{-2}
$Q_{0.1m}$	Measured soil heat flux density below the layer	Wm^{-2}
$Q_{G,g}$	Soil heat flux over grass surface	Wm^{-2}
$Q_{G,c}$	Soil heat flux over concrete surface	Wm^{-2}
$Q_{L,sky}$	Incoming long-wave radiation flux density from the sky	Wm^{-2}
$Q_{L,gd,g}$	Emitted long-wave radiation flux density over the grass surface	Wm^{-2}
$Q_{L,gd,c}$	Emitted long-wave radiation flux density over the concrete surface	Wm^{-2}
$Q_{S,sky}$	Incoming short-wave radiation flux density from the sky	Wm^{-2}
$Q_{S,gd,g}$	Emitted short-wave radiation flux density over the grass surface	Wm^{-2}
$Q_{S,gd,c}$	Emitted short-wave radiation flux density over the concrete surface	Wm^{-2}
$Q_{S,KP}$	Global solar radiation measured at King's Park	Wm^{-2}
$Q_{S,TKL}$	Global solar radiation measured at Ta Kwu Ling	Wm^{-2}
$UHII_{avg}$	Average of daily heat island intensity	^{o}C
$UHII_h$	Mean of hourly UHII	^{o}C
UHIIm	Monthly mean of daily maximum UHII	^{o}C
$UHII_{max}$	Maximum of daily heat island intensity	^{o}C
$UHII_{min}$	Minimum of daily heat island intensity	^{o}C
UHIIy	Annual mean of daily maximum UHII	^{o}C

$\overline{w'T'}$	Average of the product of w' and T' fluctuations	Kms^{-1}
$\overline{w'\rho_v'}$	Average of the product of w' and ρ_v' fluctuations	$kgm^{-2}s^{-1}$
WS_{KP}	Annual average of wind speed at King's Park	ms^{-1}

Chapter 1 : Background of heat island studies

1.0 Outline

Chapter 1 introduces the background and development of heat island studies. Section 1.2 describes the significance of this study. Section 1.3 lists the aims and objectives of this study. The last section outlines the structure of this thesis.

1.1 Introduction

Urban temperature is often higher than rural temperature in calm and clear sky days. Massive building construction in downtown areas are made of concrete that accumulates solar energy during daytime and relaxes heat during nighttime. Replacing the trees / grassland by the paved concrete layer leads to the change of heat budget including emitted long-wave radiation, latent heat, sensible heat and soil heat. Apart from natural heat source, anthropogenic heat is generated in the city and warms the city throughout the day. In contrast, the sun is the only heat source in rural areas during daytime, and plants then convert solar energy into chemical energy through photosynthesis. Therefore, in rural areas, less heat is dispersed to the surroundings during nighttime. This difference in energy budget explains briefly why urban areas are warmer and this phenomenon is called 'urban heat island effect'.

Urban heat island studies have become a hot topic in recent years. Many countries have analyzed the consequences of the heat island effect. In general, the consequences of urbanization are likely to influence climates, deteriorate air quality, increase energy demand and enhance the transmission of tropical diseases (Tong et al. 2005; Sarrat et al. 2006; Fung et al. 2006). Other observed climatic impacts include more hot warning days, more smog days, reduction in visibility, lower wind speed, less sunshine and more rain (Leung et al. 2004). Possible control measures have been recommended to lower the strengths of heat island, and the use of green roofs is one of the popular measures (Akbari 2002; Wong et al. 2003). Recently, Memon et al. (2008) reviewed the generation, determination and mitigation of urban heat island and concluded that there is a need to develop methods for determining the effectiveness of UHI mitigation. In order to establish a feasible and efficient control strategy, it is important to firstly quantify the heat island intensity in Hong Kong and then study the surface energy budget quantitatively in various regions.

To investigate the characteristics and properties of urban heat island, there are four common approaches which have been used in many research studies. Field measurement is the most common and traditional approach. This approach involves collecting temperature readings and measuring heat budget. For ambient temperature monitoring, temperature data are acquired from meteorological stations located in both urban and rural areas or measured using sensors that are mounted in moving vehicles. For heat budget measurement, heat fluxes of net solar, sensible, latent and soil heat are commonly measured using an eddy fluctuation method. Another approach is a remote sensing analysis, which has been adopting in many research studies by using thermal sensors (Nichol 1996; Streutker 2003). Surface temperature data retrieved from remote sensing images can provide an instantaneous temperature distribution over a region. The most widely used approach is numerical modelling, which is applied in studying urban climate (Borghi et al. 2000; Martilli 2002). Both global and mesoscale models are performed in exploring boundary layer climate, regional climate and temperature inversion effect. An experimental approach such as laboratory scale models and wind tunnels has also been adopted to study UHI (Oke 1981; Poreh 1996). This approach can simulate the urban environment under controlled conditions and often these results were compared with field measurement results.

1.2 Research interests

A number of heat island research topics have been explored using these four approaches. These topics include basic heat island characteristic study, key factors affecting heat island intensity, heat flux analysis, measurement technology development and heat island impacts on atmosphere and environment. In general, the characteristics of heat island intensities are examined in many cities. Higher heat island intensity usually occurs 3-4 hours after sunset on clear sky days. Key factors affecting heat island can be grouped into three: meteorological, urban design parameters and physical parameters. Low wind speed with 2-3 m/s or below can encourage the occurrence of urban heat island effect during nighttime.

Regarding heat flux analysis, net radiation, sensible heat, latent heat and soil heat are basic fluxes in studying urban heat island formation. The difference in sensible heat flux between rural and urban areas is likely the key flux change that causes temperature variation. Anthropogenic heat is an additional energy generated from human, which can strengthen the temperature variation. Apart from anthropogenic heat flux, some scientists recently raise the flux of the energy storage in plants to furbish energy conservation. The significant effect of CO_2 flux on energy balance is still doubtful. This flux definitely exists but the ratio to net radiation over the urban areas is considered less because indigenous plants were replaced by concrete long time ago.

In short, part of this study's results cover some research interests and the discussion will aid to direct the latest research in the heat island field. As UHI in Hong Kong have not been fully examined, district heat island intensities in Hong Kong are firstly quantified using the four approaches (mobile observations, remote sensing analysis, fixed station data analysis and heat budget measurement). The derivation of surface heat island intensities is further enhanced by integrating traditional approaches. In addition, the heat budget formation of heat island over concrete and grass surfaces is discussed.

1.3 Aims and objectives

The aims of this study are to explore the urban heat island in a metropolitan city (Hong Kong) and the formations of heat island in a microscale level. The results of this study would be a milestone to establish a plan to mitigate the heat island effect as well as urbanization consequences.

In this study, there are four objectives.

The first objective is to identify the existence of urban heat island in Hong Kong. Four approaches are adopted to investigate the heat island effect: mobile transverse measurement, fixed station method, remote sensing technique and 1-dimensional heat budget measurement. The UHI is verified by reporting the findings from each approach.

1. The second objective is to assess the temporal characteristics of the heat island intensity. Characteristics studied include seasonal and diurnal patterns. A short-term and long-term trend analysis of its intensity is analyzed using a fixed station analysis.

2. The third objective is to assess the spatial characteristics of the heat island intensity. The spatial characteristics are acquired by integrating mobile transverse measurement and remote sensing technique. A method to link the atmospheric and surface heat island phenomenon and analyze these characteristics is also introduced.

3. The fourth objective is to understand the heat budget characteristics over grass and concrete surfaces. Surface heat fluxes are examined based on the findings of a 1-year intensive heat budget measurement. Some physical parameters such as albedo and emissivity used in current modelling are criticized and the impact of land cover change is also discussed.

1.4 Thesis outline

The background of heat island study has been introduced in this chapter. The aims and objectives of this study are also listed. Chapter 2 reviews the literature of heat island study and the research interests of this study. Chapters 3 covers the definition of urban heat island intensity and describes four methods including mobile transverse measurement, remote sensing technique, fixed station data analysis and surface heat budget measurement. Chapters 4 to 7 report the findings from the four methods. The valuable and hot scientific issues are also discussed followed by the findings. The key findings and interpretations of this study and a few recommendations for further research are concluded in Chapter 8.

Chapter 2 : Literature review

2.0 Outline

Heat island studies originated from the microclimate research since 1960s. In the early development stage of heat island study, most research started with inversion impact and boundary layer studies and has reported heat island as one of the consequences of meteorological situations. Mitchell (1961) investigated the characteristics of heat island in U.S.A. by analyzing the temperature readings of meteorological stations and introduced a correlation between heat island intensity, and city growth rate and meteorological parameters (winds and cloud cover). A simple temperature field observation was employed in London to explore the change of meteorological parameters due to urbanization (Chandler 1965). Clarke (1969) studied the urban climate effect and examined the inversion effect on urban climate. Oke (1973) suggested a relation between city size and urban heat island intensity. Landsberg (1979) continued the study of the temperature differences in London and discussed the impact of heat budget. Since 1980, more research related to heat island has been conducted using fixed station, field observation, satellite images and heat budget modelling. UHI and its impacts have been quantified and possible strategies to mitigate the impact of rapid urbanization have been discussed.

The impacts of rapid urbanization include temperature rise, air pollution deterioration, higher energy consumption, higher epidemic potential, and poorer environment quality. Furthermore, some research findings suggested that heat island can also lead to the change of meteorological parameters such as wind flow (Khan and Simpson 2001a), precipitation (Goldreich 1995; Baik and Chun 1997) and cloud amount (Tumanov et al. 1999). In addition, land and sea breeze effect and heat island circulation are intensified (Mochida et al. 1997). This change in microclimate is expected to cause air pollution problems in urban areas in calm days (Tong et al. 2005; Sarrat et al. 2006) and play an important role in initiating thunderstorms (Rozoff et al. 2003).

This section summarized briefly the background and development of heat island study. The possible consequences of heat island effect in some metropolitan areas are also outlined. Sections 2.1 to 2.4 describe the literature review of four common methods used in heat island studies in the past 30 years separately and followed by their related scientific research interests. The first method is mobile observation (section 2.1). This method is commonly adopted to explore the temperature difference between rural and urban areas. Second, fixed station (section 2.2). Fixed station data analysis is able to study the long-term trend and the spatial distribution. Third, a remote sensing technique which has been developed since mid-1990s (section 2.3). This method is able to determine the spatial distribution of land surface heat island intensity and to measure a regional temperature profile. Last, heat budget study (section 2.4). Different types of models together with field measurement have been adopted in heat island studies to investigate the thermal difference between rural and urban areas. Section 2.5 concludes this chapter by addressing the niche of this study.

2.1 Mobile observations

Mobile Transverse measurement

Mobile transverse measurement is one of the most common and easy approaches to investigate heat island impacts in a city. It is widely known that mobile measurement could measure the direct and reliable air temperatures in a street canopy level. For those measurements, the temperature sensors were usually attached on the roof of moving objects which moved along the road or sometimes carried by researchers who walked along the street. The basic temperature difference between urban and its surrounding areas was then calculated. One of the earlier mobile transverse measurements was conducted in Tokyo in 1990 and the detailed horizontal structure of heat island in Tokyo was investigated using trains (Yamashita 1996). Other than trains, vehicles are the common moving objects for mobile transverse measurements. A mobile transverse measurement was also conducted in Tokyo in 1992 (Saitoh et al. 1996). Their results showed a nocturnal UHI intensity of approximately 8^{o}C in a winter night and that value was then used to compare with simulated surface temperature results. Afterward, other mobile transverse measurements were conducted in Pune, India (Deosthali 2000), Szeged, Hungary (Unger et al. 2001a), Tel-Aviv, Israel (Saaroni et al. 2000), Singapore (Wong and Yu 2005) and Debrecen, Hungary (Bottyán et al. 2005). Based on these observations, the highest nocturnal intensity of 7.1°C was recorded in summer in Singapore. A list of the observed heat island intensities using different methods (mobile observations, fixed station and Lidar observations) is tabulated in Table 2.1.

As expected, positive heat island intensity is usually recorded at nighttime. However, few studies remark that the intensity could be negative during daytime (Ripley et al. 1996). These studies reported that the observed cold island intensity could reach 7.9°C in the daytime of summer in Saskatoon, Canada. That means the temperature in urban areas may be lower than that in rural areas around noon, especially on clear sky days. The spatial distribution of high-rise buildings is a key reason for lower temperatures in urban areas around noon. Direct solar radiation in urban areas is usually blocked by the buildings and temperatures in urban areas therefore increase slowly compared to those temperatures in open space (rural areas) during the daytime. This phenomenon is called “Cool Island Effect” and is an opposite observation of heat island. Recently, the concept of cool island effect can lend a notion of possible mitigations of heat island (Chang et al. 2007).

As listed in Table 2.1, most studies reported the highest measured intensity during a winter night but not in summer. However, a heat island study in New Jersey, U.S.A. suggested that the potential hazard of heat island effect is likely to increase in hot seasons (Rosenzweig et al. 2005). This implies that an intensive and comprehensive heat island study in summer is needed to investigate the episode and the worst consequences of heat island effect.

Table 2.1 Summary of observed heat island intensities in selected Asian, European and American cities

City	**Latitude**	**Average heat island intensity**	**Maximum heat island intensity**	**Methods**	**References**
Asia					
Guangzhou, China	23 °8'N	0.2 to 4.7°C (1985 to 2000)		Fixed station	(Weng and Yang 2004)
Hong Kong, China	22°12'N	0.4 to 1.3°C (night, August – September 2002) -1.3 to 3.4°C (June – September 2003)		Fixed station Fixed station	(Giridharan et al. 2005) (Giridharan et al. 2007)
Nanjing, China	32°3'N	0.5 to 3.5°C (night, July – September 2005)		Fixed station	(Huang et al. 2008)
Pune, India	18 ° 32'N	2 to 3.1°C (night, 12-13 April, 1997)		Mobile survey	(Deosthali 2000)
Seoul, Koera	37°34'N	2.0 to 4.4 °C (1973 – 1996)		Fixed station	(Kim and Baik 2002)
Singapore, Singapore	1°17'N	 -1.8 to 3.8°C (March 2003 – February 2004)	4.0°C (night, 22 July 2002) 3.0°C (night, 1 December 1992) 7.1°C (night, 17 May 2003)	Mobile survey Fixed station Field measurement (fixed temperature)	(Wong and Yu 2005) (Tso 1996) (Chow and Roth 2006)
Taipei, Taiwan	25°2'N	0.39 to 0.42°C (August – September 2003) 0.45 to 0.59°C (December 2003 – February 2004)		Field measurement (portable sensors)	(Chang et al. 2007)

Tokyo, Japan	35 ^{o} 2'N		8.0^{o}C (night, 14 March 1992) 8.0^{o}C (night, 4 December 1990)	Mobile survey Tram survey	(Saitoh et al. 1996) (Yamashita 1996)
Europe					
Bucharest, Romania	44^{o}26'N		4.0^{o}C (night, May-December, 1994)	Fixed station	(Tumanov et al. 1999)
Debrecen, Hungary	47^{o}30'N	2.0 to 2.5^{o}C (night, March 2002 – March 2003)	5.8^{o}C (night, 16 June 2002)	Mobile survey	(Bottyán et al. 2005)
Granada, Spain	37^{o}11'N	1.7 to 2.5^{o}C (overall average, 1901-1990)	7^{o}C (winter month)	Fixed station	(Montávez et al. 2000)
Ĺȯdź, Poland	51^{o}47'N		8.0^{o}C (night, February 1996)	Fixed station	(Klysik and Fortuniak 1999)
Paris, France	48^{o}51'N	1.0 to 6.0^{o}C (9-10, March 1995)		Field measurement (Lidar, Sodar, meteorological instrument)	(Dupont et al. 1999)
Szeged, Hungary	46^{o}15'N	0.0 to 2.6^{o}C (night, March 1999 – February 2000)	 2.6^{o}C (night, March-August 1999)	Mobile survey Mobile survey and Fixed station	(Unger et al. 2001a) (Unger et al. 2001b)
Tel-Aviv, Israel	32^{o}6'N	3.0 to 5.0^{o}C (night, 27-28 February 1995)	6.0^{o}C (night, 27-28 February 1995)	Mobile survey and Fixed station	(Saaroni et al. 2000)

America					
Barrow, Alaska	71 °18’N	2.2 to 6.0°C(December 2001 – March 2002)	9.0°C (night, 3-6 February 2002)	Fixed station	(Hinkel et al. 2003)
Columbia, Maryland, The USA	39 °12’N		8.0°C (4 October 1974)	Mobile survey and fixed station	(Landsberg 1979)
Mexico city, Mexico	19 °26’N	1.0 to 5.0°C (May 1994 – April 1995)	7.8°C (night, February 1995)	Fixed station	(Jáuregui 1997)
New York, The USA	40°43’N	3.0 to 4.0°C (1997-1998)	8°C (night, 9-10 December 1998)	Fixed station	(Gedzelman et al. 2003)
Phoenix, Arizona, The USA	33 °26’N	9.4 to 12.9°C (3-12 April 2002)	14.6°C (night, 3-12 April 2002)	Fixed station	(Hawkins et al. 2004)
Saskatoon, Canada	52 °10’N		7.9°C (daytime, 5 August 1994)	Mobile survey	(Ripley et al. 1996)

Vertical temperature profile measurement

Apart from the ground and horizontal mobile transverse measurement in the street level study, vertical temperature profile has been performed to study the relationship between an inversion effect and heat island studies. Heat island effect generally weakens the lapse rate in urban areas and air pollutants dispersion. In 1969, an inversion effect study was carried out in both urban and rural areas using a helicopter in Cininnati, the U.S.A. and the study reported that the inversion in the rural area was stronger than that in the urban area (Clarke 1969). In 1990s, the effect of temperature inversion and cold air drainage on heat island formation was examined by integrating mobile and stationary observations (Kuttler et al. 1996). Lidar and pilot balloon measurements were carried out to study the nocturnal boundary layer formation (Dupont et al. 1999; Kolev et al. 2000) and the features of heat island (Sang et al. 2000). Some further studies have integrated vertical profile measurements with modelling to investigate the effect of heat island on vertical mixing depth in Brisbane (Khan and Simpson 2001b) and on temperature inversion effect in New York (Childs and Raman 2005). Studying vertical profile becomes an ordinary way to explain heat island formation in some episodes.

2.2 Remote sensing technique

Remote sensing technique is a cost effective and efficient method to analyze surface heat island intensity. The development of thermal sensors from the precocious meteorological sensor to the latest high resolution thermal sensor can definitely enhance surface heat island studies in terms of temporal and spatial resolutions.

Infrared camera was initially utilized to detect the thermal pattern of urban areas. The spatial resolution technique has improved from 10 km to 2 m in the past 40 years and detailed surface thermal pattern could then be examined progressively. In 1970s, the sensor in an Improved TIROS Operational Satellite (ITOS-1) with 10 km spatial resolution was acquired to identify the thermal data in urban area (Rao 1972). The Very High Resolution Radiometer (VHRR) with 0.75 km was then adopted to be used to examine the night urban and rural radiant surface temperature differences for the cities in the U.S.A. (Matson et al. 1978). A small applications explorer satellite under the Heat Capacity Mapping Mission (HCMM) at a spatial resolution of 0.5 km was utilized to quantify the day and night data surface thermal patterns of urban and rural areas in different regions of the U.S.A. (Price 1979). In1980s, the earlier Advanced Very high Resolution Radiometer (AVHRR) with 1.1 km spatial resolution on NOAA satellite was launched and this imagery data was commonly acquired for studying the radiant surface temperature in the U.S.A. (Kidder and Wu 1987, Balling and Brazel 1989). A higher resolution (90 m) of LANDSAT thermal data was then developed to examine the surface temperature over Dallas, Texes (Aniello et al. 1995) and in Singapore (Nichol 1996). Besides the space thermal sensor, airborne sensors with relatively higher spatial resolution, such as Advance Thermal and Land Application Sensor (ATLAS) with 5 m, thermal video radiometer with 2 m, were utilized to explore the correlation between heat budget and land cover / land use. The airborne sensor provides a better interpretation of surface thermal study (Lo et al. 1997; Saaroni et al. 2000) but needs high operational cost and complex techniques. Considering the economy restriction and technical feasibility, a space thermal sensor has been commonly chosen to carry out surface heat island studies, including this study. Table 2.2 summarizes a specification of thermal sensors used in the recent 10 years.

Table 2.2 Description of common thermal sensors used in the recent 20 years

Satellite sensors			Major References
Sensors	Thermal bands	Spatial Resolution	
LANDSAT TM	Band 6 (10.4 – 12.5 μm)	120 m	Weng and Yang 2004
LANDSAT ETM+	Band 6 (10.4 -12.4 μm)	60 m	Weng et al. 2004; Xu and Chen 2004
MODIS	Channels 31 – 32 (10.8 – 12.3 μm)	0.5 – 1.0 km	Zhang et al. 2005 (in Chinese)
AVHRR	Channels 4-5 (10.3 – 12.5 μm)	1.1 km	Gallo et al. 1999
ASTER	Bands 10 – 14 (8.1 mm – 11.7 μm)	90 m	Kato and Yamaguchi 2005
Airborne Remote sensor			
Thermal Infrared Multispectral scanner (TIMS)	IR band (8.0 – 11.0 μm)	50 m	Iino and Hoyano 1996
Advanced Thermal and Land Application sensor (ATLAS)	Channel 13 (9.6 – 10.2 μm)	10 m	Lo et al. 1997

Regarding surface heat island studies, satellite-derived surface temperatures are usually considered as a surrogate of traditional ambient temperature. It is expected that the ground surface temperature is generally higher than the ambient temperature. There certainly exists a correlation between surface and ambient temperature, but little research has been carried out so as to explore the link between these two temperatures for heat island studies. Price (1979) addressed that there is a need to find out the relationship between surface and air temperature to further interpret the heat island phenomenon with satellite images. Few researchers have discussed the correlation between these two temperatures under a specific weather condition in high-latitude cities (Kanto and Phoenix) (Kawashima et al. 2000; Hartz et al. 2006). However, the correlation between surface and traditional heat island studies remains unclear. A comprehensible relationship between the surface and air temperatures under different weather conditions for the tropical cities would certainly help to enhance the interpretation of surface heat island. It is worth exploring the empirical related equations to simplify the derivation of atmospheric heat island intensities from remote sensing images and complement the limitations of the other approaches.

Generally speaking, there are three main research themes using the remote sensing technique for surface heat island studies: 1) to examine the spatial structure of urban thermal patterns in regional scale and canopy scale; 2) to develop satellite-derived indexes linking a correlation between land cover change/ land use change to the properties of surface heat island intensity; 3) to examine the urban surface energy budget through coupling with urban climate models.

Facet temperature effect

In addition to the regional surface thermal temperature pattern, Voogt and Oke (1997) implied that complete surfaces temperature of buildings (vertical and horizontal surfaces) would enhance the accuracy of air temperature estimation in the facet level. Nichol (1998) discussed the temperatures in vertical and horizontal facets with the sun angle and azimuth at the image time. In recent years, Nichol and Wong (2005) have further investigated the enhancement of 3-D visualization on simulating the relationship between urban heat island and air pollution. Few studies focused on this matter of facet temperature effect but the overview of surface heat island in microscale study can approximately represent the surface heat island.

Satellite-derived Indexes

A correlation between the normalized difference vegetable index (NDVI) and surface heat island properties has started in the early stages of the remote sensing technique. The difference in the NDVI between urban and its surrounding appears to be an indicator of surface temperature differences between urban and rural areas. Numerical studies have found that NDVI is negatively correlated to temperature difference between urban and rural areas in a few U.S.A. cities (Gallo et al. 1995; Weng et al. 2004). In 1996, a new term "heat island potential" in urban canopy was introduced based on the sensible heat flux to explain heat island difference in Kawasaki, Japan (Iino and Hoyano 1996). During recent studies, new bareness index is proposed and it is positively related to UHI (Chen et al. 2006). In Hong Kong, Nichol (2005) employed IKONOS images and aerial photography to create the NDVI mapping and simulate the canopy temperature using the visualization method for daytime and nighttime satellite images. Therefore, NDVI index is a useful and traditional tool to determine the heat island effect. It will be interesting to create a new index in interpreting the surface heat island using remote sensing techniques.

Thermal Map Application

Surface heat budget plays an important role in interpreting the change of heat island. Thermal map is a way to depict a spatial heat island by combining satellite images with the model output in Salt Lake (Gluch et al. 2006). This thermal map can be applied in the urban planning and heat island mitigation (Weng and Yang 2004). In Hong Kong, an integrated measurements approach has not been used in carrying out heat island studies. It is high time to start heat budget research coupled with remote sensing techniques and/or field measurements to explore its heat island phenomenon and realize heat island formation.

2.3 Fixed station

Fixed station data analysis is a common and low cost approach to characterize the heat island, study the trend of heat island and explore factors influencing the magnitude of heat island intensity. To explore nocturnal heat island intensity, many research studies have adopted this approach and the observed nocturnal heat island intensities could reach 3°C in Singapore (Tso 1996), 7.8°C in Maxico city (Jáuregui 1997), 4.0°C in Bucharest, Romania (Tumanov et al. 1999), 12°C in Ĺỏdź, Poland (Klysik and Fortuniak 1999), 7°C in Granada, Spain (Montávez et al. 2000), 3.5°C in Nanjing, China (Huang et al. 2008), 4.4°C in Seoul, Koera (Kim and Baik 2002), 9°C in Barrow, Alaska, U.S.A. (Hinkel et al. 2003), 8°C in New York (Gedzelman et al. 2003) and 14.6°C in Phoenix (Hawkins et al. 2004). The detailed observed heat island intensities in the selected Asian, European and American cities are listed in Table 2.1. These findings showed that heat island intensities in different cities likely varied with local urban climates. Studying urban climates is able to facilitate a better understanding of heat island formation and this is one of the latest study areas.

In Hong Kong, a preliminary daytime heat island study was carried out using fixed station data in Giridharan's study (2004). Giridharan et al. (2005) then reported that the maximum nocturnal UHI intensity was between 0.4ºC and 1.3ºC in three particular estates located in the south-western part of Hong Kong Island. Air temperatures recorded in residential areas were considered as urban reference readings while air temperatures measured at one of the Hong Kong Observatory stations (located in the police training center) was reference temperatures. As such, their results may not well represent urban heat island intensity in Hong Kong because the urban reference points are not located in the center of the city. It would be of interest to examine where the highest and the most representative heat island intensities of Hong Kong are.

Studying the trend of the heat island intensity is essential to understand the impact of heat island made to the environment. In general, a time-series analysis was usually performed in urban stations and their surrounding stations in order to facilitate the understanding of urban planning and policy making. Recent research studies have investigated the features of heat island trends in large

U.S.A. cities using fixed station data analysis (Magee et al. 1999; Stone 2007). The findings in these studies found that the annual trend of heat island intensity can reach the maximum of 0.06^{o}C/year in San Juan (Velazquez-Lozada et al. 2006). In Europe, the similar trend study was conducted in Czech but the finding reported that the average annual trend of heat island intensity was lower than those in American cities (Brázdil and Budíková 1999). Kim and Baik (2002) reported one of the earlier trend studies of heat island intensity in Asian city (Seoul) using the temperatures recorded in two meteorological stations and the trend value was 0.56^{o}C over 24 years. Furthermore, the relationship between UHI intensity trend and temperature trend has been explored since mid-1990s (Camilloni and Barros 1997; Chung et al. 2004). Parker (2006) further studied the impact of heat island effect on global temperature. It is important nowadays to quantify the urbanization impact on temperature trend so as to develop sustainable urban plans in developing countries.

Regarding factors affecting heat island, multiple regression analysis is used to find a correlation between UHI intensity and variables. These variables can be grouped into three classes: physical parameters, urban design parameters and meteorological parameters. The physical parameters include surface albedo, land cover/use and solar radiation. The urban design parameters include sky view factor, glass-to-surface area, total height-to-floor area ratio, local green area, building height, surrounding built area ratio, altitude of the site and proximity to heat sink (Giridharan et al. 2007). Oke (1981) suggested that sky view factor is one of key canopy geometry parameters to simulate the UHI. Unger (2004) further explored the relationship between sky view factor and UHI intensity. Bottyán and Unger (2003) simulated UHI intensity by integrating both urban design parameters and physical parameters including built-up area and water surface ratio, sky view factor and building height. The meteorological parameters include solar radiation, wind speed, wind direction, relative humidity, cloudiness, precipitation and pressure, and pressure (Chow and Roth 2006; Fortuniak et al. 2006). A considerable amount of research has reported that both wind speed and the heat island intensity measured on the previous day are the keys to explain the temperature difference between urban and rural areas using regression model analysis in New York and in Korea (Gedzelman et al. 2003;

Kim and Baik 2004). In addition, some recent studies have supported that cold air drainage is another meteorological reason causing higher temperature readings in urban areas (Montávez et al. 2000; Bejarán and Camilloni 2003). These studies tried to interpret how the extreme high heat island intensity could occur in specific weather conditions in selected cities.

2.4 Heat Budget Study

Field measurement

Surface heat budget measurement is another common way to study the effect and formation of heat island in terms of heat flux. Four fundamental heat fluxes are net radiation, soil heat, sensible heat and latent heat. A set of fast-response instruments was usually adopted to compute sensible heat and latent heat using an eddy covariance technique. However, most studies reported the simulation results of heat budget together with data verification derived from field measurement and/or satellite-derived parameters (Carlson et al. 1981; Takahashi et al. 2004). The measured heat fluxes can directly demonstrate the heat balance over different land covers and be used to verify and enhance the model output. Hafner and Kidder (1999) suggested that the satellite-retrieved surface parameters with a high resolution can be used to improve the UHI intensity simulation. That is why researchers used the heat budget measurement study together with modelling to explore heat island studies. However, little information about the temporal profile of heat budget over different surfaces was found. A typical case of heat budget measurement is a study to investigate the change of heat flux over grass surfaces to concrete surfaces. In addition, the results of heat budget measurement can be used to verify and justify the model input parameters and the simulation outputs.

Heat Budget Model

A number of research studies have been carried out the thermodynamic models to investigate the heat island study since 1980s. Oke (1989) mentioned that heat budget studies can be generally grouped into two meteorological layers: boundary layer and canopy layer. For the boundary layer, global and mesoscale models are operated to determine the heat budget over different surfaces and both vertical and horizontal temperature profiles. For the canopy layer, different canopy microscale models have been developed and used to estimate urban temperatures and heat budgets at the ground level. In recent 20 years, Johnson et al. (1991) demonstrated a surface heat island model to simulate the radiation budget cooling of simple rural and urban canopy surfaces. This surface heat island model was subsequently applied to simulate energy changes using the thermal and physical properties of both urban and rural areas (Oke et al. 1991). An urban geometry model without anthropogenic heat was applied to discuss the effect of urban geometry (ratio of wall height to street width) on urban thermal environment (Sakakibara 1996). A building canopy model coupled with CFD was also developed (Ashie et al. 1999). Afterward, Masson (2000) developed a Town Energy Balance (TEB) model to simulate turbulent fluxes at different canopy surfaces. In 2005, two modifications of thermal and dynamical parts in the Penn State/NCAR Mesoscale Model (MM5) were made so as to improve the simulation results of temperature and heat budget in the urban boundary layer (Dandou et al. 2005). Developing microscale models can improve heat budget simulation and its accuracy in local areas.

There are five key components in heat budget model: net radiation, anthropogenic heat, soil heat, sensible heat and latent heat. Both net radiation and anthropogenic heat are generally considered as heat sources. Many studies have explored the net radiation, which can be well calculated net radiation in clear sky days based on the latitude of the cities (Terjung and Louie 1973). In the northern hemisphere, the highest simulated net radiation in the high-latitude city (Paris) was approximately 700W/m^2 in the summer day of 1994 (Lemonsu and Masson 2002). Net radiation can also be obtained by measuring four component radiation sensors or an integrated net radiometer sensor (Campbell Scientific 2009). Another heat source (anthropogenic heat flux) can be estimated from buildings sector, transportation sector and metabolism using a top-down approach (Sailor and Lu 2004). Previous studies generally agreed that an understanding of anthropogenic heat's impact on heat island studies is needed (Ichinose et al. 1999; Fan and Sailor 2005). However, until now, there is no universal method to compute an anthropogenic heat from the data set of energy consumption, power generation, number of vehicle or a combination thereof.

Reliable measurement and forecast tools can help develop urban plans in new towns and mitigate the severity of heat island impact. A number of studies have reported that anthropogenic heat caused by human in the urban areas can be main heat source for heat balance system but few studies have discussed that the anthropogenic heat on heat island study was insignificant (Bonacquisti et al. 2006). A recent study has estimated anthropogenic heat discharge and natural heat radiation from sensible heat flux using satellite remote sensing and ground meteorological data (Kato and Yamaguchi 2005). The correlation between anthropogenic heat and heat island studies has been addressed but more quantitative analyses of such impact on heat island studies is still needed.

In addition, soil heat, sensible heat and latent heat are the converted heat energy from heat sources. Soil heat flux density was also determined by considering the properties of soil temperature gradients in both urban and rural areas (Kimball et al. 1976). On the other hand, both sensible and latent heats are usually simulated using thermodynamic models or the eddy covariance measurements. According to the first law of thermodynamics, the change of sensible heat and latent heat plays an important role to explain the higher temperature measured in urban areas and the impacts of urbanization (Oke 1982). Therefore, numerical research focused on measuring, calculating and simulating the sensible heat with an ultimate aim of forecasting urbanization impact and recommending suitable mitigations. Recently, Roth (2007) reviewed the findings of subtropical urban climate studies in the recent 10-year studies and reported that the ratio of sensible heat to net radiation in rural areas was approximately 28% in rural areas and the corresponding ratio will increase to around 40% in urban areas. He also concluded that number of urban climate studies in subtropical cities is limited.

In Hong Kong, Kalma et al. (1978) simulated four components without an anthropogenic heat that the net radiation was 80 Wm^{-2} at night and 550 Wm^{-2} during the daytime in industrial land use, the peak latent heat of 440 Wm^{-2} was found consideration in mid-July 1971. Urbanization in Hong Kong have started to develop since 1980s, recent heat budget information in Hong Kong is limited. It is time to measure and/or simulate heat budget in Hong Kong again after the study in 30 years ago.

2.5 Chapter summary

In this chapter, the history of heat island studies is introduced. Previous studies on heat island intensities in different cities and the four methods in conducting heat island studies are reviewed. Based on the literature review, the main gaps in the current heat island study are identified as follow.

1. There is insufficient information in Hong Kong to identify the characteristics of local heat island and to understand its causes.
2. The correlation between surface and traditional heat island studies remains unclear. Typical conversion equations under different weather conditions are required in the current stage. Integrating traditional measurement method with remote sensing technique can provide innovative ideas and further explore heat island studies.
3. Recent researchers have attempted to find a correlation between urbanization and climate change / air quality. It would be of interest to quantify such correlation in regional scale and simulate the impact of urbanization on global temperatures and human health.
4. Beside four fundamental heat fluxes, anthropogenic heat is considered as another important source of heat island. More quantitative analyses of the correlation between anthropogenic heat and heat island studies is still needed. Some local physical parameters and specific geographical variables can also improve the accuracy of local heat budget models.

This study will contribute to scientific research on quantifying heat island intensities, enhancing the interpretation of surface heat island studies and justifying heat budget analysis.

Chapter 3 : Methodology

3.0 Outline

To explore the characteristics and formation of urban heat island studies in Hong Kong, four methods were selected to investigate the heat island formation in a coastal and complex terrain city. These methods included mobile transverse measurement, remote sensing technology, fixed station data analysis and a surface heat budget measurement. In addition, integrating two or more methods was attempted to explore the correlation between surface and ambient temperatures and investigate the formation of heat island in the complex city.

Section 3.1 introduces the definition of a term “UHI intensity” and describes urban and reference site selection. Section 3.2 describes a series of 20 mobile transverse measurements employed in this study from 2003 to 2005. A pilot in-situ temperature pairs study is also illustrated, which is used to assist the mobile transverse measurements. Section 3.3 outlines the detailed measurement of the remote sensing images and depicts image processing for a thermal sensor. Section 3.4 shows the third method: fixed station data analysis. A long-term fixed station data analysis for 20 years at six Hong Kong Observatory stations and a short-term temperature analysis for 2 years at 2 sites are presented. Section 3.5 outlines surface heat budget measurement over two surfaces in a specific site. A detail description of instruments employed in this study is also shown.

3.1UHI intensity and site selection of fixed stations

<u>*UHI intensity*</u>

In this study, the term “urban heat island intensity” (hereafter UHII) is generally defined as temperature differences between urban areas and reference areas. The average percentage of built-up area in urban/suburbs area and rural area is above 26% and less than 10% respectively.

The heat island intensity (UHII) at a specified time is expressed as

$$UHII = T_u - T_r \qquad (3.1)$$

where UHII is urban heat island intensity between urban and reference areas

T_u is the air temperatures in urban areas

T_r is the air temperatures in reference areas

However, the ground mobile measurement usually took 2 to 3 hours to complete a mobile measurement. An air temperature reading along the measurement was then adjusted to the reference time as follows

$$T_u = T_m + T_c + T_{d,i} \qquad (3.2)$$

where T_u is air temperatures used in the subsequent analysis

T_m is air temperatures measured by the vehicles

T_c is an adjustment of temperature due to calibration and

$T_{d,i}$ is an adjustment of temperature due to diurnal variation over the specified time period

Sites selection

It is highly debatable whether fixed stations are urban or rural. There are 11 meteorological stations of Hong Kong Observatory (HKO) in Hong Kong, where air temperatures have been recorded since 1946. A number of researchers suggest that the airport station is a rural area while some defined the nearest countryside station as a rural area. To clarify this point, only two (King's Park and HKO Headquarters) of HKO stations are definitely classified as urban areas while all HKO stations would be defined as suburban or rural areas. In addition, it is reasonable to suggest that Hong Kong International Airport station at Chek Lap Kok is not a suitable representative rural reference point in Hong Kong. The reason is that the Hong Kong international airport is located in a reclamation area and therefore air temperature in this case is highly dominated by urban characteristics with large concreted area.

In this study, two Hong Kong Observatory urban stations, namely HKO Headquarters (HKO) in Tsim Sha Tsui and King's Park (KP) in Homantin were located in densely populated districts in Kowloon Peninsula. Temperature readings are accredited by Hong Kong Observatory. In general, HKO is the key urban station for a long-term fixed station data analysis.

Another selected reference station is located at Ta Kwu Ling. The station is about 24 km north of Kowloon and 15m above sea level. The location is rather remote and less susceptible to both marine and urban influences. It is a small piece of flat land (about 4 km^2) surrounded by terrain. The altitude of the terrain is around 940 m in the north (Ng Tung Shan), around 490 m in the east (Robin's Nest), and around 140 m in the southwest (Sheung Shui and Wa Shan). The station is in one of the most undeveloped regions in the Pearl River Delta. It is situated in a suburban area with a low density population and low rise buildings (building heights are less than 10 m). The percentage of built-up area comprises about 14% of the land cover around the reference station. The wind strength in this area is low throughout a year. Its location was marked with a white star in Figure 3.1.

3.2 Mobile transverse measurement

3.2.1 Mobile transverses measurement (June 2003 – April 2005)

<u>Time</u>

To examine the existence of the heat island phenomenon in Hong Kong, a comprehensive mobile observation measurement was conducted to measure and identify the representative heat island intensities in three years (2003-2005). A total of 20 mobile trips were carried out on 9 clear sky days. Table 3.1 lists the dates and periods of the field trips. Where meteorological conditions allowed, mobile transverses were repeated for three periods in one day: 2:00 to 4:00 (morning), 13:00 to 16:00 (afternoon), and 20:30 to 23:30 (evening). It took about 2 to 3 hours to complete a field trip. As spring is generally cloudy, only two mobile transverses were conducted on 19 April 2005.

Table 3.1 Dates and periods of 20 mobile transverse measurements (X marks the measurement for the specified periods; the reference time in each period is marked in brackets)

Date \ Period	**Morning (3:00)**	**Afternoon (15:00)**	**Evening (22:00)**
2 June 2003		X	X
3 June 2003	X		
6 July 2003	X	X	X
24 September 2003		X	X
25 September 2003	X		
28 September 2003	X	X	X
9 January 2004	X	X	X
11 January 2004	X	X	X
19 April 2005	X	X	

The general routes of the two vehicles, the coastlines, and the land use patterns are shown in Figure 3.1. One of the routes is marked as white for Hong Kong Island while the other one is marked as black for Kowloon and the New Territories. The mobile routes covered a large part of Hong Kong, omitting only the eastern part of the New Territories and the outlying islands. The land uses along the selected routes are mostly urban. Although Hong Kong has a complex and rugged terrain and coastline, the routes shown in Figure 3.1 are relatively flat and are near sea level. Though air temperature gradually decreases with altitude, in this study the influence of altitude is considered to be insignificant.

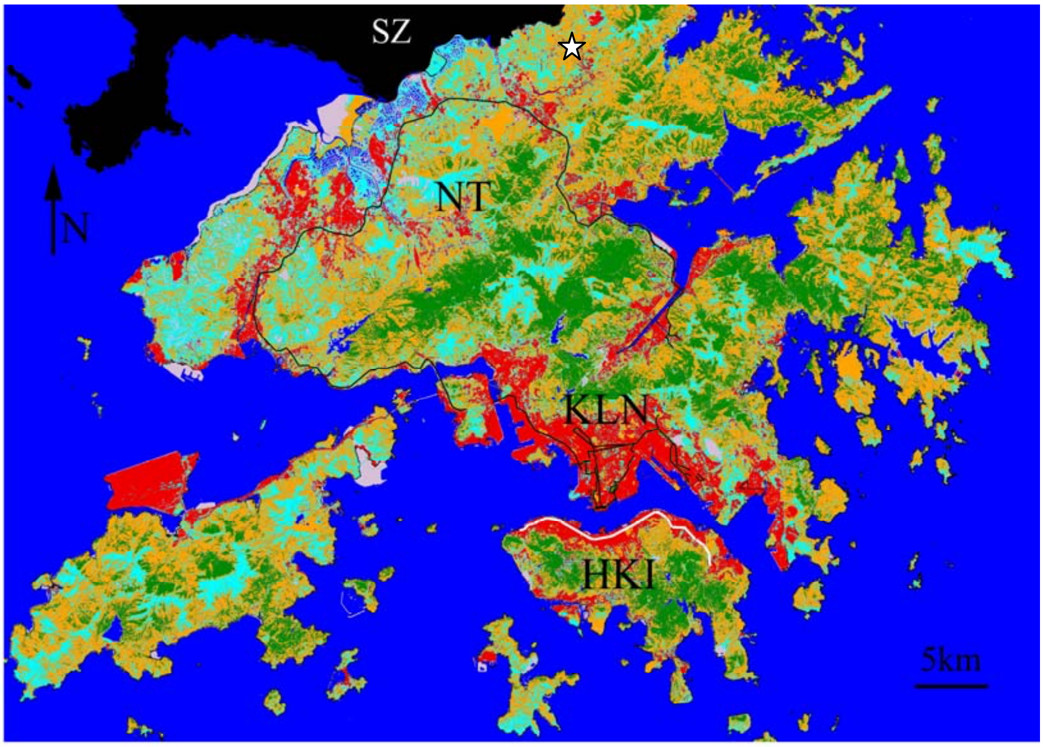

Figure 3.1 Two mobile routes (Route for Vehicle 1 – Black line; Route for Vehicle 2 – White line) and six land cover classifications (forest – green; dry forest – cyan; other vegetation – orange; soil/sand – grey; water – blue; urban – red; no data – black) [NT – New Territories; KLN – Kowloon; HKI – Hong Kong Island; SZ – Shenzhen, Mainland China; White star marker – Ta Kwu Ling HKO reference suburban station]

Instruments

For each field trip, two vehicles were employed and driven around the northern part of Hong Kong Island, Kowloon Peninsula and the New Territories. Each vehicle was equipped with two temperature sensors and a global positioning system (GPS) receiver. The two temperature sensors used were a thermister and a thermocouple. These two sensors were fixed to the roof of the vehicles and covered by a paper box (similar to a Stevenson screen) to abate solar heating and wind chill. An example of those equipment settings is depicted in Figure 3.2. The sampling frequency of the temperature sensors was set at two seconds. At an average speed of 60 $kmhr^{-1}$, the temperatures were logged once every 17m. The precision of all temperature sensors was 0.1^{o}C. The GPS receiver was connected to a notebook computer on board the vehicle for recording the real time positions. The sampling frequency of the GPS was set at one second.

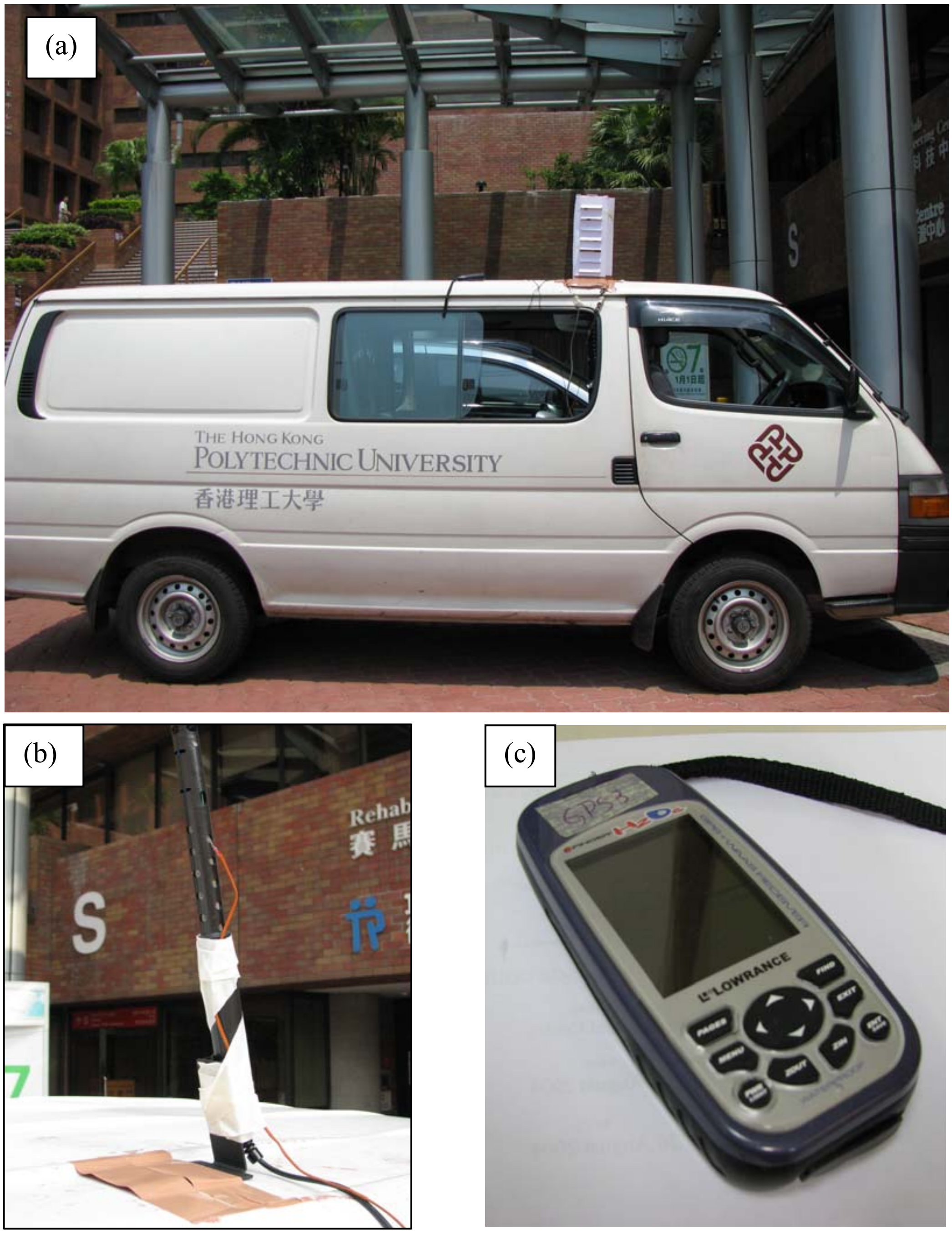

Figure 3.2 Equipments Setting (a) on the roof top of vehicle, (b) Two temperature sensors setting and (c) a GPS receiver

Quality Assurance and Quality Control

All temperature sensors were calibrated in the laboratory of The Hong Kong Polytechnic University using the OMEGA CL750A calibrator together with a standard thermometer (NIST SRM 934). Full calibrations were conducted in the winter once a year from 2005 to 2007. Zero and span checks were conducted in the summer. A total of five calibration points were acquired: 0°C, approximately 15°C, 30°C, 35°C, and 40°C. Zero and Span temperature calibration set-up is shown in Figure 3.3.

Figure 3.3 Set-up of zero and span Temperature calibration in the laboratory of The Hong Kong Polytechnic University

In addition to the above instrument error, another source of error concerns the temperature change over the time of the transverse, as each field trip lasted from two to three hours. To eliminate the variations caused by natural diurnal change, all temperature records for each field trip were adjusted to one reference time. First, the reference time for the morning, afternoon, and evening trips were set at 3:00, 15:00, and 22:00 respectively. Second, the hourly temperature profile observed at the HKO headquarters for all field trips was acquired. The temperature profile was then fitted using a polynomial curve with 14 powers (Figure 3.4). Third, the diurnal temperature adjustment $T_{d,i}$ for each data was determined from the HKO temperature difference between the reference time k and the measured time i where $T_{d,i} = T_{HKO,i} - T_{HKO,k}$ (see Equation (3.2)). Finally, each data T_m was replaced by T_m - $T_{d,i}$. $T_{d,i}$ and was between -0.5°C and +0.6°C in summer, between -0.4°C and +0.2°C in fall, and between -0.6°C and +0.9°C in winter. Overall, the temperature adjustment ranged from -0.6°C to +0.9°C. As 0.9°C is about 33% of the average UHII in Hong Kong (see Chapter 6.2), this adjustment is significant and necessary in cities with small UHII. This study revealed that neglecting the diurnal variation of ambient temperature in a mobile transverse can induce an error of up to 0.9°C. One effective way to reduce this error would be to limit the measurement time by shortening the field route or employing more vehicles for a field measurement.

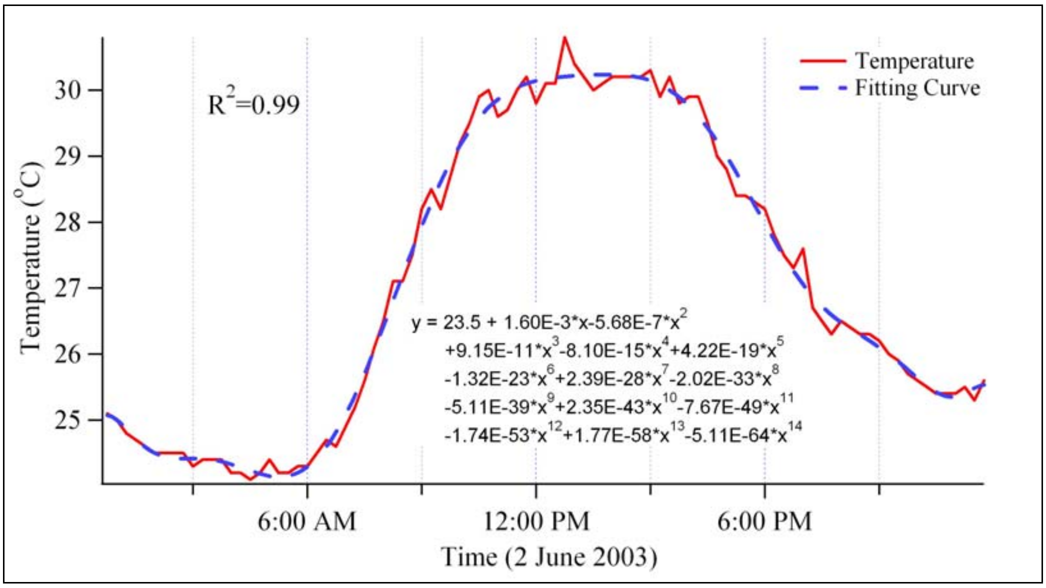

Figure 3.4 Diurnal variation of air temperature and its polynomial fitting on 2 June 2003

3.2.2 In-situ temperature pairs measurement

Another pilot study was carried out after a series of mobile measurement in the period of 2007-2008. This study integrated ground measurement and the remote sensing technique. The ground crews measured ground surface temperatures and ground air temperatures simultaneously when a satellite overpass. This provided data for the "calibration" of the satellite-derived surface temperature and allowed the computation of correlations between the surface and ambient temperatures. The set-up of ground measurement is outlined in this section and the procedures for image processing is depicted in section 3.3.2.

Sampling Dates and Time

Owing to the scarcity of acquiring a clear satellite image, a total of four integrated measurements were conducted in 2007 and 2008. They were 31 January 2007, 30 November 2007, 13 August 2008 and 13 September 2008. These four days were selected to explore the temperature correlation in both daytime and nighttime during both cold and warm seasons. Table 3.2 listed the date and time of the satellite Terra passed Hong Kong. A thermal instrument (Advanced Spaceborne Thermal Emission and Reflection Radiometer (ASTER)) was installed in the satellite to receive the long-wave radiations from the ground. Since the overpass of the satellite was scheduled by Earth Remote Sensing Data Analysis Center (ERSDAC), ground measurements were carried out between 10:00 and 13:00 for the daytime image and between 21:00 and 0:00 for the nighttime image when the satellite passed over.

Table 3.2 Dates and time of Terra satellite passed over Hong Kong

	Satellite overpass	
	11:03 LST [(1)]	22:42 LST [(1)]
Cold season	30 November 2007	31 January 2007
Warm season	13 September 2008	13 August 2008

[(1)] LST: Local Standard Time (+08:00 UTC)

To cooperate with the remote sensing focal study, the ground crews including two mobile vehicles teams and one walking team were employed. The routes of these vehicles were almost the same for four days. Both vehicles first drove to Kowloon. One vehicle then traveled to the western side of the New Territories, while the other vehicle traveled to the eastern side. The team on foot took measurements on the roofs of buildings and public parks. The objective was to record both ground surface temperatures and ground air temperatures at different land use locations that could be seen by the satellite sensor. Figure 3.5 demonstrates an example of the routes of two vehicles and the in-situ ground stations employed on 31 January 2007, which are marked as green and blue lines and pink squares respectively.

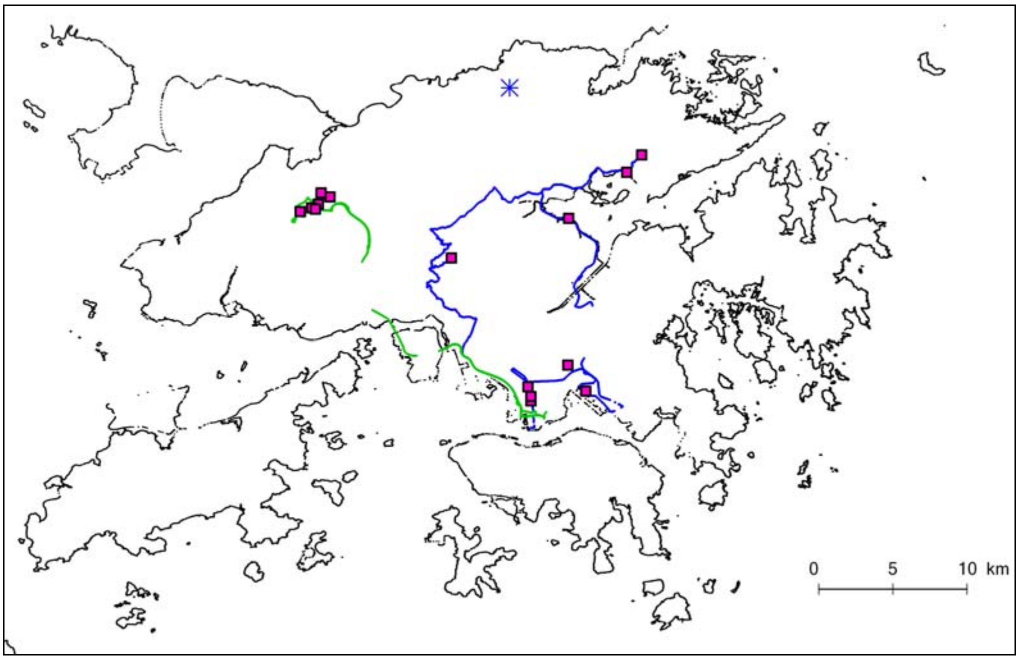

Figure 3.5 Routes of two vehicles when the Terra passed Hong Kong and the in-situ ground stations on 31 January 2007 [Blue line: Route 1; Green line: Route 2; Pink squares: in-situ ground stations; Blue star: location of reference area]

Ground measurement instruments

The equipment used by the vehicles for the air temperature measurement was the same as that reported in section 3.2.1. In addition, each vehicle also took pairs of in-situ surface and air temperature measurements en-route at about six different locations. All three teams measured both in-situ surface and air temperatures at pre-planned locations. Portable temperature sensors were used by the walking team. The resolutions of all sensors were set at 0.2^{o}C. The in-situ air temperature was measured at 1 m above ground. Each pair of in-situ surface temperature/ambient measurements was the average of three consecutive samplings. The in-situ surface/air measurements were taken in Kowloon Peninsula and the New Territories. The surface type of these sites included urban (such as roads and building roofs) grassland and sand. The in-situ surface and air temperatures were also adjusted by using Equation (3.2). In addition, sea surface temperature and lake surface temperature were collected to perform the atmospheric correction for image processing.

On 31 January 2007, the two vehicles traversed 148km, 14815 air temperatures (by vehicles) and a total of about 25 pairs of in-situ surface/air temperatures (manual) were collected. On 30 November 2007, the two vehicles traversed 194km, 12799 air temperatures (by vehicles) and a total of about 29 pairs of in-situ surface/air temperatures (manual) were collected. On 13 August 2008, the two vehicles traversed 125km, 8964 air temperatures (by vehicles) and a total of about 17 pairs of in-situ surface/air temperatures (manual) were collected. On 13 September 2008, the two vehicles traversed 127km, 8848 air temperatures (by vehicles) and a total of about 36 pairs of in-situ surface/air temperatures (manual) were collected.

3.3 Remote sensing technology

The second method employed in this study was remote sensing. There are two objectives for selecting this method for heat island studies. The first one is to study the surface temperature distribution over a large interested area in one snapshot image. The second one is to find the correlation between surface and ambient temperatures over different land uses and weather conditions by integrating this measurement with the ground measurement.

3.3.1 ASTER thermal sensor and study area

In this study, a thermal instrument (Advanced Spaceborne Thermal Emission and Reflection Radiometer (ASTER)) flying on a satellite Terra, which was launched in December 1999, was selected to acquire a high quality satellite thermal image. ASTER instrument consists of three separate telescopes (VNIR, SWIR and TIR) and each telescope is sensitive to a specific wavelength. TIR telescope is sensitive to the thermal source. The wavelengths of the five thermal bands are between 8.125μm and 11.65μm. Band 13 (10.25 to 10.95 μm) was selected due to its lower noise levels and higher atmospheric penetration (Nichol 2005). A spatial resolution of thermal bands is as high as 90m.

Terra satellite repeats a cycle every 16 days (233 orbits). Almost the same thermal images can be obtained every 16 days but no single image can capture the entire land area of Hong Kong. Kowloon Peninsular and New Territories were specified as the interested area of image selection. Although the sensor is automatically scheduled to capture thermal images, the quality of image could be affected significantly due to cloud and aerosol. When the satellite was anticipated to fly over the interested areas with less than 20% cloud amount in core urban areas, a mobile transverse measurement was employed to measure the ground temperatures. Four successful measurements were carried out on 31 January 2007, 30 November 2007, 13 August 2008 and 13 September 2008. The overpass time over Hong Kong was at 22:42 LST (local standard time) for 31 January 2007 and 13 August 2008 and was at 11:03 LST for 30 November 2007 and 13 September 2008. The coverage of daytime and nighttime images and the focus area of this study are shown in Figure 3.6. Data obtained from this method was mainly compared with the results from mobile transverse measurement. The ground in-situ measurement was carried out within 2-3 hours when the satellite passed Hong Kong.

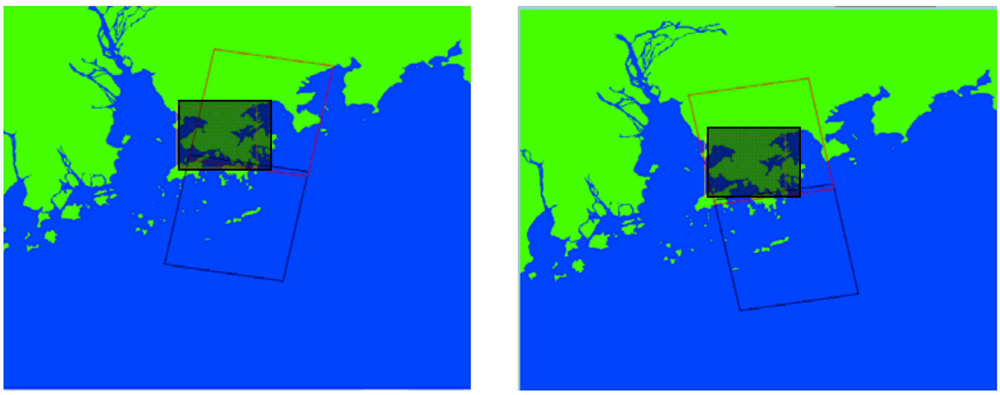

Figure 3.6 Coverage of ASTER sensor over interested areas at 11:03 LST (left) and at 22:42 LST (right) [grey area: interested areas; Red square: coverage of image]

3.3.2 ASTER image processing

ENVI, an image analysis software, was selected to process the thermal image. In general, there were four principal procedures to compute the satellite-derived surface temperatures from the raw data of the thermal image. They are geometric and radiometric correction, the conversion of spectral radiance to black body temperature, emissivity correction and atmospheric correction. These four procedures are described in the following subsections.

Geometric and Radiometric Correction

Before processing a raw data from the satellite images, most images are geometrically and radiometrically corrected to become higher level images. The level 1A data was first converted to radiance in radiometric correction and a rational function model was adopted in orthorectification (rms < 0.5). Theoretically, the spectral radiance was obtained from the digital number (DN) value as follows. The unit conversion coefficient of band 13 is 5.693 x 10^{-3} (W $sr^{-1}m^{-2}$)/DN (Abrams et al. 1998).

$$L_\lambda = (DN - 1) \text{ x unit conversion coefficient} \qquad (3.3)$$

where L_λ is the spectral radiance in W $sr^{-1}m^{-2}$

DN is Digital Number from 0 to 4095

Conversion of the spectral radiance to black body temperature

The definition of the black body is that all incident radiations falling on the body are totally absorbed and its surface emissivity is equal to 1. The black body temperature is the temperature at which a black body would emit the same radiation as is emitted by a given radiator at a given temperature. The spectral radiance was then converted to the black body temperature using the Planck radiation law,

$$T_b = \frac{K_2}{\ln(\frac{K_1}{L_\lambda} + 1)} \quad (3.4)$$

where T_b is the Black body temperature in Kelvin

K_1 = 890.01 is the calibration constant 1 in W $sr^{-1}m^{-2}$

K_2 = 1357.3 is the calibration constant 2 in K

L_λ is the spectral radiance in W $sr^{-1}m^{-2}$

Emissivity Correction

Distortions and noises in satellite images are serious impediments for quantitative analysis. Emissivity correction is carried out to enhance the accuracy of land surface temperature. The black body temperature was then transferred to a surface temperature (satellite-derived surface temperature) by emissivity correction (Sabins 1997). The emissivity of different land classes was derived from a land cover map, which is created from the previous daytime SPOTS and LANDSAT images. In this study, there were a total of six different land types and their emissivity value for band 13 (see Figure 3.1 and Table 3.3).

Table 3.3 Emissivity value used for Level 1 data for band 13 of ASTER image

Land Cover Type	**Emissivity value used for Level 1B data**
Forest	0.97
Water	0.99
Dry Grassland / dry forest	0.91
Other Vegetation	0.97
Urban	0.92
Soil/Sand	0.95

The image resolution of 90 m was enhanced to 10 m using Equation (3.5). This was achieved using the latest emissivity correction procedure (Nichol 2009).

$$T_{sat,suf} = \frac{T_b}{\{1 + [(L_\lambda T_b / \alpha) \times \ln \varepsilon]\}} \qquad (3.5)$$

where $T_{sat,suf}$ is the satellite-derived surface temperature in Kelvin

T_b is the Black body temperature in Kelvin

L_λ is the spectral radiance in W $sr^{-1}m^{-2}$

α is a constant value, 1.438×10^{-2} in mK

ε is the emissivity values of the land cover

Atmospheric Correction

Atmospheric correction is the last step to reduce the effect of atmospheric particles through absorption and scattering from the atmosphere and the earth surface. Atmospheric absorption of water vapour, CO_2 and O_3 can mainly reduce the amount of radiation from the surface due to the overlapped spectra between those gases and the selected wavelength used in the sensor. Atmospheric scattering of particles and the radiances from the ground have an additive effect on the radiation reaching the satellite sensor. Atmospheric correction is the processing to eliminate radiation from the ground and the atmospheric radiance from upper boundary layer.

In this study, atmospheric correction was carried out by adjusting the digital sea surface temperature by the true sea surface temperature acquired from HKO and the field measurements. If the addition of 10 DN values before conversion to radiance had the effect of raising $T_{sat,surf}$ value by 5°C by considering the sea surface pixels, all other image values would then be adjusted accordingly. This adjustment may be restricted to a temperature range which is related to the range of $T_{sat,surf}$ observed.

3.4 Fixed station data analysis

The previous two methods can only provide short duration information on good weather days. This section describes the fixed station data analysis method which is able to provide information on long-term trend. The first objective of using this method is to explore the basic characteristics of heat island intensity for the past 19 years. The second one is to examine the relationship between ambient and surface temperatures over different land covers in different weather conditions.

3.4.1 Long-term fixed station data analysis

<u>Six HKO fixed stations</u>

A total of six HKO stations were selected from 27 HKO stations. The locations of these six stations are marked as a blue diamond in Figure 3.7 and the brief description of these stations is listed in Table 3.4. Two of these six HKO stations were grouped as urban stations and other four as suburban stations or rural stations. The two selected urban stations were Hong Kong Observatory Headquarters (HKOH) and King’s Park (KP), the selected suburban stations were Cheung Chau (CCH), Lau Fu Shan (LFS), Ta Kwu Ling (TKL) and one rural station was Waglan Island (WGL). Table 3.5 lists three criteria used to classify the station types. Station classification will be discussed in section 6.1 in detail.

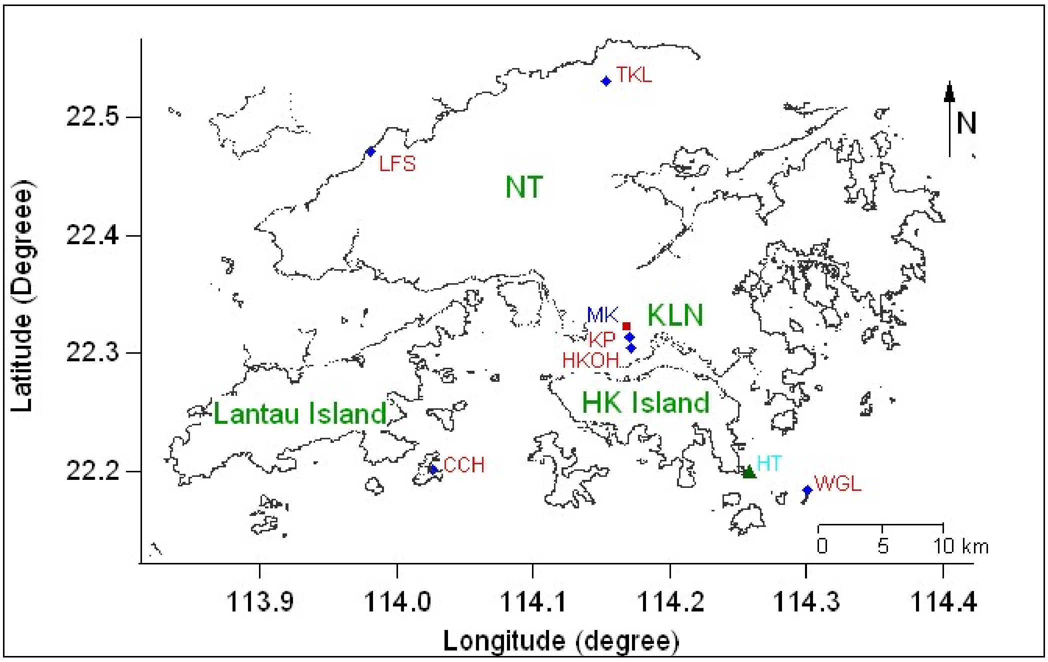

Figure 3.7 Locations of six HKO stations and two selected EPD fixed stations owned by Environment Protection Department, HKSAR (EPD) and The Hong Kong Polytechnic University (PolyU) [HKOH: Hong Kong Observatory Headquarters; KP: King's Park; CCH: Chueng Chau; WGL: Waglan Island; TKL: Ta Kwu Ling: LFS: Lau Fu Shan; MK: Mong Kok; HT: Hok Tsui] [NT: New Territories; KLN: Kowloon; HK Island: Hong Kong Island; Lantau Island: Lantau Island] [HKO stations marked in blue diamonds; EPD station marked in red square; PolyU station marked in blue triangle]

Table 3.4 Brief description of six HKO stations and two non-HKO stations

	Station	Location	Altitude of station (1)	Area Category	Data used for station comparison
HKO stations	HKO Headquarters, (HKOH)	22^o 18' 7" N 114^o 10' 27"E	32 m	Urban	1988 – 2004
	King's Park, (KP)	22^o 18' 43" N 114^o 10' 22"E	65 m	Urban	1993 – 2004
	Cheung Chau, (CCH)	22^o 12' 4" N 114^o 1' 36"E	72 m	Suburban	1993 – 2004
	Waglan Island, (WGL)	22^o 11' 56" N 114^o 18' 12"E	56 m	Suburban	1996 – 2004
	Tai Ku Ling, (TKL)	22^o 31' 43" N 114^o 09' 24"E	15 m	Suburban	1988 – 2004
	Lau Fu Shan, (LFS)	22^o 28' 8" N 113^o 59' 1"E	31 m	Suburban	1988 – 2004
Non-HKO stations	Mong Kok, (MK)	22^o 19' 21"N 114^o 10' 7"E	28 m	Urban	2006-2007
	Hok Tsui, (HT)	22^o 12' 35"N 114^o 15' 29"E	65 m	Rural	2006-2007

(1) Altitude is measured above mean sea level

Table 3.5 Criteria for station type classification

Criteria	Urban	Suburban	Rural
Built-up area (%)	>26	11-25	<10
Building type*	> 10 storey	3-10 storey	1-2 storey
Population density (people/km^2)	> 10,000	1000 – 9,999	< 1,000
Examples of HKO stations	HKOH, KP	CCH, LFS, TKL	WGL

* refers to 80% of buildings in the area

Analysis for long-term trend

Hourly temperature data from six HKO stations were acquired from 1989 to 2007. To explore the spatial characteristics of UHII, two urban stations (HKOH and KP) and four reference stations (CCH, LFS, TKL and WGL) were employed and eight combinations of heat island intensity were then generated. The period of data analysis for the spatial characteristics is from 1993 to 2004. Hourly heat island intensity was firstly computed by Equation (3.1). Daily maximum UHII was then calculated by taking the largest hourly UHII value on that day. Both diurnal and seasonal variations of UHII were studied.

To investigate the trend of heat island intensity in Hong Kong, a representative urban station (HKOH) and a representative suburban station (TKL) were selected. Frequency distribution, diurnal, seasonal and annual variations were studied for 19 years. In addition, temperature from the selected suburban TKL station was also used to verify data derived from the remote sensing method.

3.4.2 Additional short-term temperature measurement

A short-term temperature measurement over two non-HKO stations was conducted for two years (January 2006 – December 2007). The purpose is to examine temperature correlation over concrete layer in one additional urban and one additional non-urban setting. The temperatures from these two additional sites are also used to verify and calibrate with data derived from the remote sensing method.

Two additional representative sites

One of the additional sites is located in Mong Kwok (MK). It is one of the urban roadside air quality monitoring stations of Environmental Protection Department HKSAR (EPD). The other reference site was located in Hok Tsui which is operated by The Hong Kong Polytechnic University (PolyU). The location of these two stations is marked with a red square and green triangle respectively in Figure 3.7 and these stations' general descriptions are listed in Table 3.4. The criteria of selecting the urban additional site were based on building and population density in that district and the results of the mobile transverse measurement. The findings support that one of the hottest areas in Hong Kong is

Mong Kok. The site at Mong Kok is surrounded by high density of high-rise buildings and nearly 99% of surface cover around the site is concrete. This urban station was operated by EPD. The surrounding view of the MK site is shown in Figure 3.8 (a). For the Hok Tsui site, it was located at an open coastal area. This is located about 16km from the MK urban station. This coastal station is operated by PolyU. The surrounding view of HT site is shown in Figure 3.8 (b).

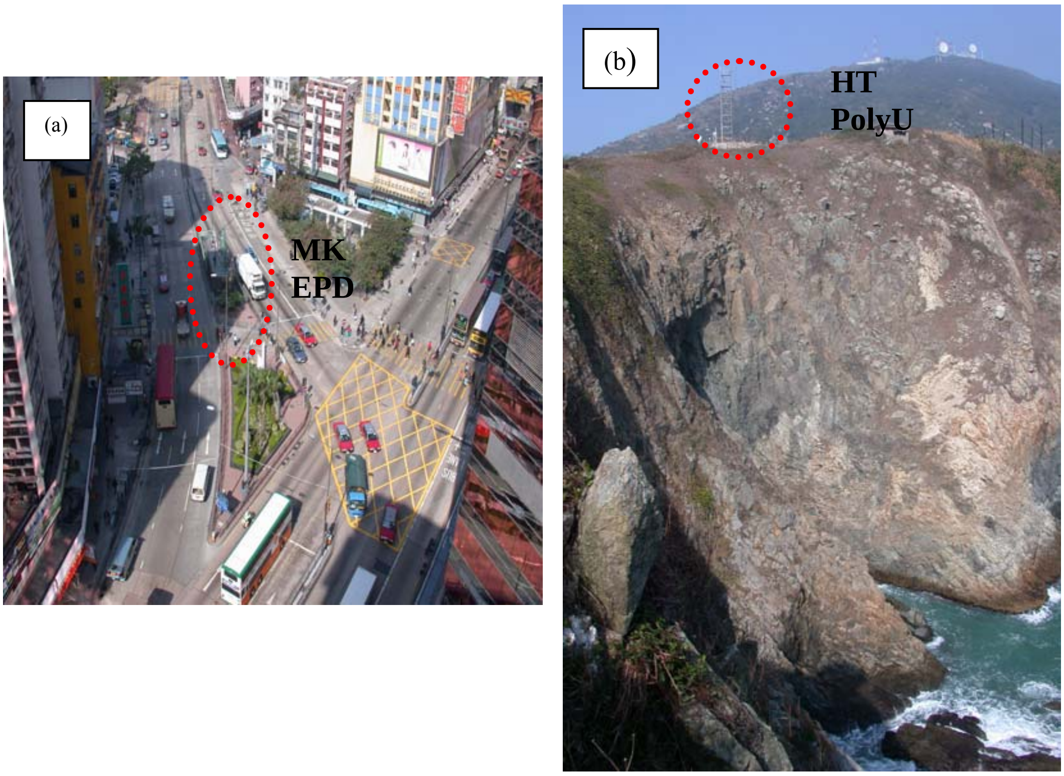

Figure 3.8 Views of two selected local sites Mong Kok, EPD roadside station (a), Hok Tsui, PolyU (b)

Instruments and Sampling

Type T thermocouple sensor measured the air temperature, surface temperature and the surface air temperature. An OMEGA data logger was used for data recording. The air temperature sensor was set 1.5m above the ground and enclosed by a Stevenson screen box to abate solar radiation heating and wind chill. The surface temperature sensor was stuck on the ground with an epoxy resin and the surface air temperature sensor was just 0.05 m above the surface temperature sensor. The sampling interval was 1 minute. The resolution of sensor was 0.1ºC. Hourly temperature readings were calculated by averaging 1-

minute readings. All temperature sensors were calibrated before and after the sampling. The detail of this calibration was described in the section 3.2.1.

3.4.3 Software

Microsoft Excel was the software adopted to handle both long-term and short-term analysis. A statistical liner regression, t-test and F-test were applied to obtain the trend of UHII and prove its significance level. In addition, both Microsoft Excel software and Igor Pro software were performed to generate the meaningful graphs showing diurnal, seasonal, annual intensity variation, correlation between ambient and surface temperatures. A 3D graph was created to present both diurnal and seasonal variation of intensity on average.

3.5 Surface heat budget measurement

The previous three methods focus on investigating temperature only. This section covers the heat budget concept of heat island formation. A surface heat budget measurement was conducted for 1 year over two typical land covers (grass and concrete surfaces) from March 2007 to February 2008. The objectives of this field measurement are to study the profile of heat budget over these two surfaces under different weather conditions and to discuss the characteristics of model input parameters. In this study, the energy variation of net radiation, sensible heat flux, latent heat flux and soil heat flux changing from over grass surface to over concrete surfaces was examined as well.

3.5.1 Thermal equations and eddy covariance measurement

In this study, the anthropogenic heat was assumed to be negligible as a selected suburban Ta Kwu Ling site was located far from urban areas and heat emission from human activities was hence limited. The energy balance equation was then simplified as follows

$$Q^{*} = Q_H + Q_E + Q_G \qquad (3.6)$$

where Q^{*} is the net all-wave radiation flux density in Wm^{-2}

Q_H is the sensible heat flux density in Wm^{-2}

Q_E is the latent heat flux density in Wm^{-2}

Q_G is the soil flux density in Wm^{-2}

Mathematical equations of four heat flux densities, namely net radiation, sensible heat flux, latent heat flux and soil heat flux, were shown in Equations (3.7) to (3.10).

$$Q^* = Q_{s,sky} + Q_{L,sky} - Q_{s,gd} - Q_{L,gd} \tag{3.7}$$

$$Q_H = -C_a K_H \left(\frac{\partial \overline{\theta}}{\partial z} \right) \tag{3.8}$$

$$Q_E = -L_v K_v \left(\frac{\partial \overline{\rho}_v}{\partial z} \right) \tag{3.9}$$

$$Q_S = -k_S \left(\frac{\partial \overline{T}_s}{\partial z} \right) \tag{3.10}$$

where C_a is the heat capacity of air at constant pressure in $Jm^{-3}K^{-1}$

K_H is the eddy conductivity for air temperature in m^2s^{-1}

$\frac{\partial \overline{\theta}}{\partial z}$ is the change rate of the potential temperature in Km^{-1}

L_v is the latent heat of vaporization in Jkg^{-1}

K_v is the eddy conductivity for water vapor in m^2s^{-1}

$\frac{\partial \overline{\rho}_v}{\partial z}$ is the change rate of the vapor concentration in kgm^{-4}

k_s is the thermal conductivity of the soil in $Wm^{-1}K^{-1}$

$\frac{\partial \overline{T}_s}{\partial z}$ is the change rate of the soil temperature in Km^{-1}

In this study, the principle of the eddy fluctuation was employed to calculate two vertical convective heat fluxes (sensible heat flux and the latent heat flux) by Equations (3.11) and (3.12) accordingly.

$$Q_H = C_a \overline{w'T'} \tag{3.11}$$

where C_a is the heat capacity of air at constant pressure in $Jm^{-3}K^{-1}$

$\overline{w'T'}$ is an average of the product of w' and T' fluctuations in Kms^{-1}

$$Q_E = L_v \overline{w'\rho_v'} \tag{3.12}$$

where L_v is the latent heat of vaporization in Jkg^{-1}

$\overline{w'\rho_v'}$ is an average of the product of w' and ρ_v' fluctuations in $kgm^{-2}s^{-1}$

A conductive soil heat flux was computed by summing the surface soil heat flux in the specific surface layers (0.1m below surfaces) and a measured soil heat flux below such layer. The equation was expressed in Equation (3.13).

$$Q_s = \frac{\Delta T_{soil} C_{soil} d}{t} + Q_{0.1m} \tag{3.13}$$

where ΔT_{soil} is a temperature change in the measurement surface layer in K

C_{soil} is the heat capacity of soil surface layer in $Jm^{-3}K^{-1}$

d is the depth of installation of a soil heat flux plate in meter, m

t is the duration of measurement interval in second, s

$Q_{0.1m}$ is a measured soil heat flux density below the layer in Wm^{-2}

Table 3.6 lists general constant values used in Equations (3.11) to (3.13). It is noted that the latent heat of vaporization is temperature dependant while the capacity of soil depends on a soil surface layer moisture. These parameters are considered to be a constant in an ambient atmosphere.

Table 3.6 Constant values used in computing the heat fluxes

Constant Parameters	**Value / Variable dependant equations**	**Unit**	**References**
C_a	1004.67	$Jm^{-3}K^{-1}$	Chen et al. 2007
L_v	(2.501-0.00237*(T_{180})*1000	Jkg^{-1}	Oke 1987
C_{soil}	1317*840+s*4180000	$Jm^{-3}K^{-1}$	Campbell Scientific Inc. 2003

where T_{180} is ambient air temperatures measured at 1.8 m above a surface in ^oC

s is a moisture content measured in a surface soil layer in %

3.5.2 Ta Kwu Ling site and sampling

This heat flux measurement was conducted at a suburban area (Ta Kwu Ling), which is located in the northern part of Hong Kong. The latitude and longitude are 22°31'43"N, 14°9'24"E. This site contains one of the Hong Kong Observatory (HKO)'s earliest automatic weather stations. HKO has been measuring temperature, wind and rainfall at this site since 1985 and historical weather data is available (Ng and Wong 1998). The detail description of TKL station was outlined in section 3.1 and the view of TKL site is shown in Figure 3.9.

Figure 3.9 Topography view of Ta Ku Ling site

One set of heat flux instruments was employed between 2 March 2007 and 28 February 2008. The measurement was carried out over a grass surface between 2 March and 5 August 2007 (Location A in Figure 3.10). The size of the grass surface was about 20 m x 20 m. The measurement was then conducted over a concrete surface between 17 August 2007 and 28 February 2008 at another Location B (about 180 meters to the northeast of Location A), see Figure 3.10. The size of the concrete surface was also about 20m x 20m. The views of two sites are shown in Figure 3.11 accordingly. The microclimate in these two areas was assumed to be the same throughout the year.

Figure 3.10 Locations of grass surface site (A) and concrete surface site (B) at Ta Kwu Ling (extracted from Google Earth)

Figure 3.11 Views of grass surface (Location A in Figure 3.10) (left side) and concrete surface (Location B in Figure 3.10) (right side)

3.5.3 Instruments

In this study, instruments included a net radiometer, a fast-response CO_2/H_2O open path gas analyzer, a fast-response three-dimensional ultrasonic anemometer, and a heat flux thermal sensor, a soil moisture sensor and a two dimensional wind sensor. These instruments were mounted on two posts and under a subsurface layer. The net radiometer was fixed on one post and all other instruments were fixed on another post. Two posts were 5 m apart. The set-up of these 2 posts over the concrete surface was the same but the instrument setting of soil heat flux meter was a little bit different between two surfaces. Over concrete surface, a 0.15 m concrete layer was paved on the top of soil, see Figure 3.12. The set-up of the soil heat flux measurement in the subsurface layer was situated between the two posts. In addition, soil temperatures were measured by using four temperature sensors and the set up of sensors was shown in Figure 3.13. All data were processed and converted to 30 minute averaged for analysis.

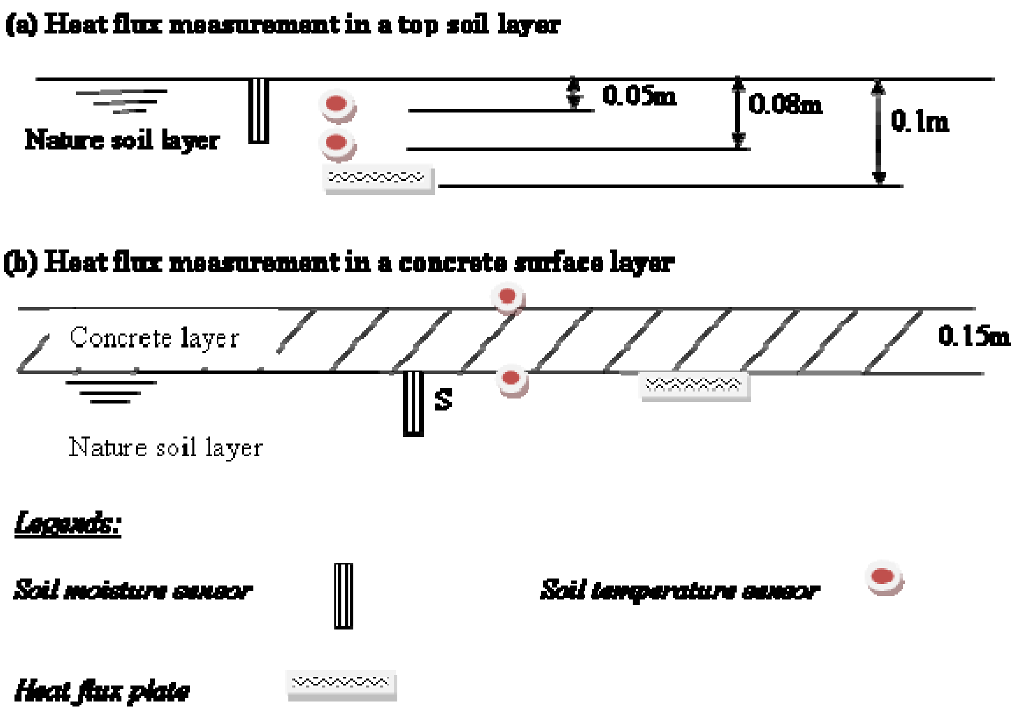

Figure 3.12 Soil heat flux equipment setting below the ground (a) over the grass surface and (b) over the concrete paved surface

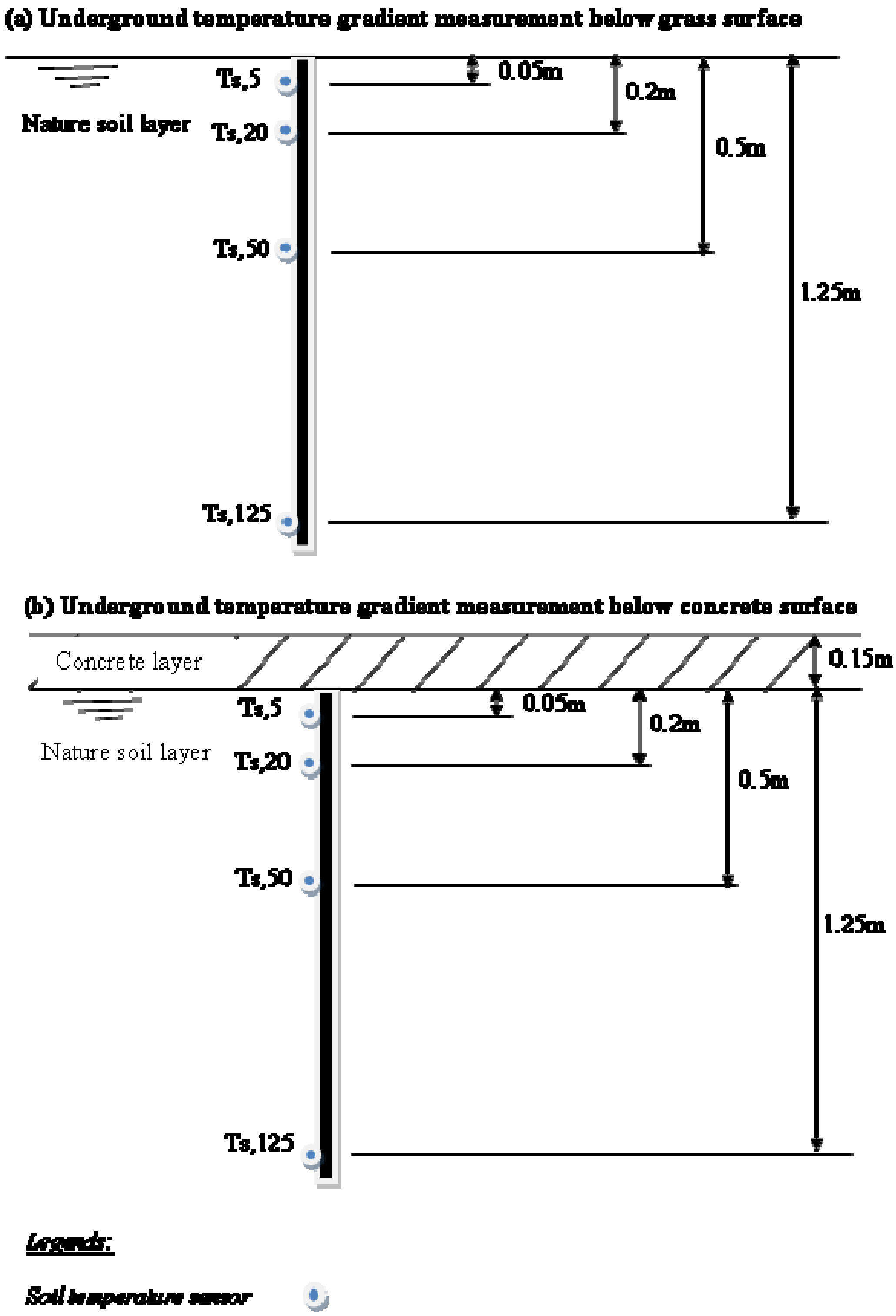

Figure 3.13 Underground temperature measurement (a) over the grass surface and (b) the concrete paved surface

Net Radiometer

A net radiometer (model CNR1, Kipp & Zonen, The Netherlands) was mounted in post 1 to measure the net radiation. The net radiometer consists of two pyranometers and two pyrgeometers. The pyranometers measured 0.3 – 3 μm spectrum of solar radiation while the pyrgeometers measured 5 – 42 μm spectrum of infrared radiation. One pair of pyranometer and pyrgeometer is facing up and the other pair facing down. It was fixed on a stainless steel vertical post and was mounted at about 1.8 m above the ground surface facing south so that the shadow of the post will not affect the measurements. Radiation sensors output was logged once every minute. Data was processed and converted to 30-minute mean subsequently. In addition, the albedo was derived from the data set where albedo is defined as the ratio of outgoing global solar radiation reflected from the earth to the incoming global solar radiation from the sky.

CO_2/H_2O Open Path Gas Analyzer

A fast-response CO_2/H_2O open path gas analyzer (LI-7500, LI-COR, Inc., Lincon, the U.S.A.) was adopted to measure the concentration of water vapor and carbon dioxide in turbulent air. The instrument was attached to stainless steel post 2 as a cantilever. The open path sensor was mounted at a slight tilt to the vertical to avoid water accumulation over the light source. The signal from the sensor was modulated at 150 Hz to minimize the effect of ambient light on operation. The wavelength absorption is 2.59 μm for water vapor measurement and 4.26 μm for CO_2 measurement accordingly. Data were captured at 10 Hz and synchronized with sonic temperature data. The data were then computed to 30-minute average latent heat flux (Q_E).

Wind sensor

A fast-response three-dimensional ultrasonic anemometer (WindMaster Pro, Gill Instruments Ltd., U.K.) was also attached to post 2 to measure three orthogonal wind components demonstrates the tailor-made horizontal mounting of ultrasonic anemometer 1.8 m above a ground surface, so that the interference to vertical wind is minimized. Sampling frequency was set at 10 Hz. Sensible heat flux (Q_H) was computed subsequently. Data was then reduced to 30-minute average of u,v,w components and Q_H. Furthermore, horizontal wind speed and wind direction were derived from three orthogonal wind components. The resolution and accuracy of wind speed are 0.01 m/s and 1% RMS respectively. The corresponding values of wind direction are 0.1^o and 0.5^o.

In addition, a two-dimensional wind sensor (Model 05305 Wind Monitor –AQ, R.M. Yong Company, the USA) was also attached on the top of post 2 to compute the horizontal wind. Sampling interval was 1 minute. Means of these data were then calculated every 30 minutes. These computed data were compared with the wind data derived from the ultrasonic anemometer.

Soil Heat flux instruments

Soil heat flux measurement contains three instruments. They were a heat flux thermal sensor (HFP01, Hukseflux, The Netherlands), a soil moisture sensor (ECH_2O EC-5, Decagon Devices, Inc., the U.S.A.) and two temperature sensors (ETC, Decagon Devices, Inc., the U.S.A.). All sensors were buried 0.1m below the ground surface. Accuracy of soil moisture sensor and temperature sensor are 3% and 0.5^oC respectively. Data from moisture sensor and temperature sensors were connected to a data logger (EM 50, Decagon Devices, Inc., the U.S.A.). Data were sampled every 1 minute. A 30-minute average of soil heat flux (Q_s) was then derived using Equation (3.13).

In addition, four underground temperatures was measured. These soil temperatures were measured by soil temperature sensors (HOBO H8, Onset Computer Corporation, the U.S.A.) and connected to a HOBO data logger. Four soil sensors were buried in the depth of 0.05 m, 0.2 m, 0.5 m and 1.25 m representatively (Figure 3.13). The accuracy of sensor is 0.5^oC. A 30-minute temperature average was processed to explore a diurnal soil temperature variation.

The net radiometer, the fast-response CO_2/H_2O open path gas analyzer, the three-dimensional ultrasonic anemometer, the two-dimensional wind sensor, the heat flux thermal sensors and the soil moisture sensor were new instruments and fully certificated by the manufacturers. All temperature sensors were calibrated in March 2008 in the laboratory of the Hong Kong Polytechnic University.

Chapter 4 : Heat island in Hong Kong

4.0 Outline

This chapter reports the heat island intensity in Hong Kong, that were obtained from mobile transverse measurements and remote sensing images. The findings of 20 mobile transverse measurements between 2003 and 2005 showed the general situation of atmospheric heat island phenomenon in Hong Kong while the remote sensing images in four episodes (mobile transverse measurement synchronized with satellite images) showed a surface heat island. These four satellite images were captured in the morning and in the evening of a winter, and in the morning and in the evening of a summer.

Section 4.1 describes the results of heat island intensity in Hong Kong by exploring both atmospheric heat island and surface heat island. Section 4.2 illustrates the findings of UHII distribution in Hong Kong and discusses a population factor. Section 4.3 outlines the results using the integrating method. Section 4.4 summarizes the significant findings of such heat island study.

4.1 Existence of heat island effect

Mobile transverse measurement and satellite remote sensing images were conducted to examine the existence of heat island effect in Hong Kong. In general, there are two types of heat island: Atmospheric heat island and Surface heat island. Both phenomena can be studied by mobile transverse measurements and remote sensing images. The detailed results are depicted in sections 4.1.1 and 4.1.2 respectively.

4.1.1 Atmospheric heat island study

Atmospheric heat island refers to heat island phenomenon between urban areas and its surrounding in terms of ambient air temperatures. Based on all 20 mobile transverse measurements between 2003 and 2005, maximum, minimum and average urban heat island intensities (UHII) at a specified period are summarized in Table 4.1. In the morning period, the range of the UHII was from -0.6^{o}C to

7.5^{o}C. The corresponding range was from -5.3^{o}C to 4.2^{o}C in the afternoon and was from -1.2^{o}C to 6.1^{o}C in the evening. On average, the mean values of average UHII over a year were 2.5^{o}C in the early morning, 0.0^{o}C in the afternoon and 2.8^{o}C in the evening. The average UHII observed in the afternoon and evening in this study are consistent with Giridharan et al. (2004, 2005), which reported that UHII observed in Hong Kong was between -1.3^{o}C and 3.4^{o}C. Their results in Giridharan's studies were based on 4-week measurements taken between 13:00 and 22:00 in the summer of 2003. Giridharan's measurements were carried out mainly in high-rise residential areas, whereas this study focuses on the most densely populated areas. In general, the findings in this study confirm that atmospheric heat island phenomenon exists in Hong Kong and mainly happens during the nighttime.

Table 4.1 Summary of maximum ($UHII_{max}$), minimum ($UHII_{min}$) and average UHII ($UHII_{avg}$) intensities for 20 mobile transverse measurements in clear sky days

Data	Season	Period	$UHII_{max}$	$UHII_{min}$	$UHII_{avg}$
6/2/2003	Summer	Evening	6.1	0.6	3.4
6/2/2003		Afternoon	4.2	-3.7	0.0
6/6/2003		Morning	3.8	-0.5	2.2
7/6/2003		Morning	7.5	1.7	5.5
7/6/2003		Afternoon	4.2	-0.2	1.9
7/6/2003		Evening	5.3	0.3	2.9
9/24/2003	Fall	Evening	3.9	0.3	2.4
9/24/2003		Afternoon	2.0	-2.5	0.1
9/25/2003		Morning	2.6	-0.6	1.6
9/28/2003		Morning	3.1	0.0	1.9
9/28/2003		Afternoon	2.7	-2.7	0.5
9/28/2003		Evening	3.6	1.2	1.9
1/9/2004	Winter	Morning	2.6	-0.1	1.2
1/9/2004		Afternoon	-1.4	-5.3	-3.0
1/9/2004		Evening	4.5	-0.8	2.7
1/11/2004		Morning	3.1	0.3	2.0
1/11/2004		Afternoon	3.2	0.1	1.7
1/11/2004		Evening	5.0	0.8	3.4
4/19/2005	Spring	Afternoon	0.0	-3.6	-1.1
4/20/2005		Morning	4.4	1.0	3.3

As shown in Figure 4.1, different bars indicate the mean values of the average UHII in different periods. Throughout the year, higher values of UHII were generally recorded during the nighttime while the lowest value was recorded during the day. It should be noted that there was a slight difference in the peak intensities among four seasons. Based on the current results, a high heat island intensity may be recorded in the evening of the spring. In the summer, higher heat island intensity was recorded in the early morning. In the fall and winter, the corresponding value was higher in the evening. It is expected that the mobile transverse measurements could capture some episodes of atmospheric heat island in Hong Kong, but it is not able to characterize the seasonal variation. To further explore the characteristics of heat island studies, the long-term fixed station data analysis was used, which is one of the common methods the similar studies employed. The results of fixed station data analysis are discussed in Chapter 6 in detail.

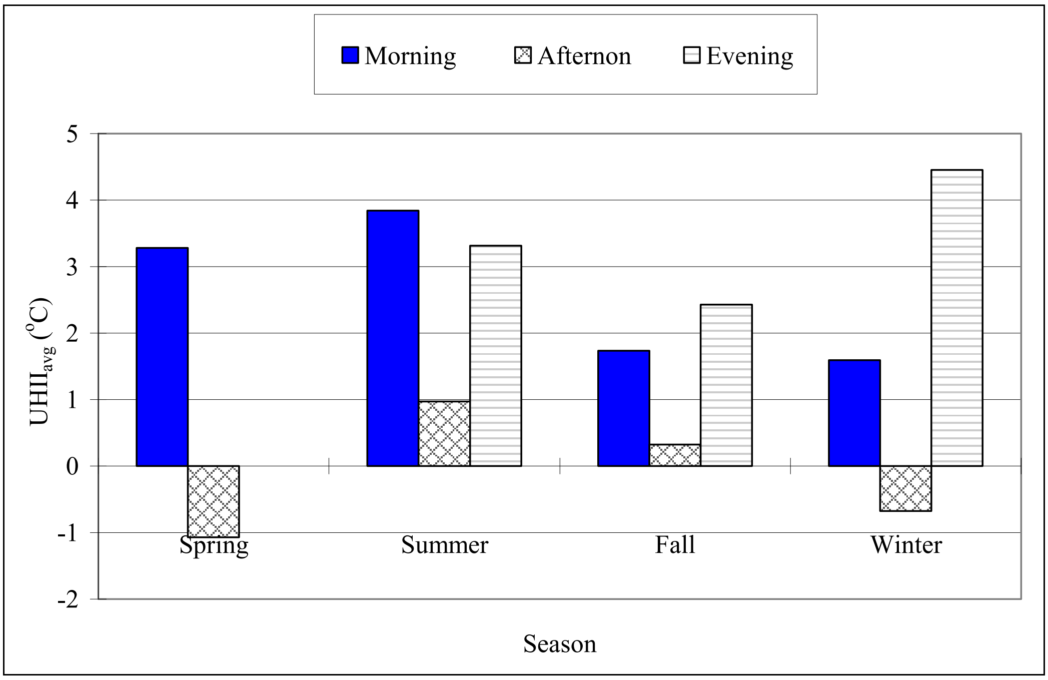

Figure 4.1 Mean values of average urban heat island intensity $UHII_{avg}$ in four seasons

There are two drawbacks of the mobile transverse measurement. One is the rather long travel time vehicles per trip. Another drawback is that the coverage of the measured areas is restricted by roads. These drawbacks may weaken the accuracy of heat island intensity and also miss the hottest spot. However, a much better methodology for the heat island study is the use of airborne scanning. Satellite Infrared thermal imaging is also a low cost alternative. Unfortunately, this methodology is plagued by the blockage of clouds and air pollution. In this study, four clear satellite images were captured in two years. The findings of surface temperatures derived from satellite remote sensing images are going to be discussed next section in 4.1.2.

4.1.2 Surface heat island study

Remote sensing technique can provide a large coverage of surface temperature information in an area at a specific time. In this study, four ASTER images were available in the morning of 30 November 2007 and 13 September 2008 and in the evening of 31 January 2007 and 13 August 2008. These four images provided an opportunity to explore daytime and nocturnal surface heat island studies in the cold and hot seasons.

Satellite-derived surface temperatures

The snapshot of a satellite-derived surface temperature on the four days is shown in Figure 4.2. The red pixels represent the hotter areas, and the blue pixels represent the colder areas. As shown in Figure 4.2 (a), the range of the satellite-derived surface temperatures was between 7.2^{o}C and 21.6^{o}C at 22:42 local time on 31 January 2007. As reported in Figure 4.2 (b), the range of the corresponding temperatures was between 14.0^{o}C and 37.8^{o}C at 11:03 local time on 30 November 2007. As depicted in Figure 4.2 (c), the range of the satellite-derived surface temperatures was between 22.9^{o}C and 36.0^{o}C at 22:42 local time on 13 August 2008. As shown in Figure 4.2 (d), the range was between 25.4^{o}C and 44.0^{o}C at 11:03 local time on 13 September 2008. These findings show that the range of the satellite-derived surface temperature was larger in daytime images. Based on the observations from four images, surface temperatures in Kowloon Peninsula and the northern part of Hong Kong Island were higher than that over the sea (not shown). Over the nighttime images, the hottest urban area was found in Mong Kok MK (which is located in the center of Kowloon Peninsula in Figures 4.2) and in Causeway Bay CWB in the northern part of Hong Kong Island. Considering the satellite-derived surface temperature over flat lands (altitude < 0.2 km), the coolest area was found in suburban areas of Ta Kwu Ling (TKL). This is one of the least urbanized areas in Hong Kong; and therefore there was no doubt to take TKL as a reference site. The surface heat island intensity was then calculated by subtracting the surface temperature at TKL from the temperature derived in urban areas.

Some caution was needed in interpreting satellite-derived surface temperatures. First, the derived surface temperatures are usually considered as a surrogate of traditional ambient temperature. Second, the implication of daytime surface heat island may be not comparable to atmosphere heat island. Third, the discrepancy of satellite-derived surface temperatures in daytime images is relatively high due to temperature algorithm and emissivity effect.

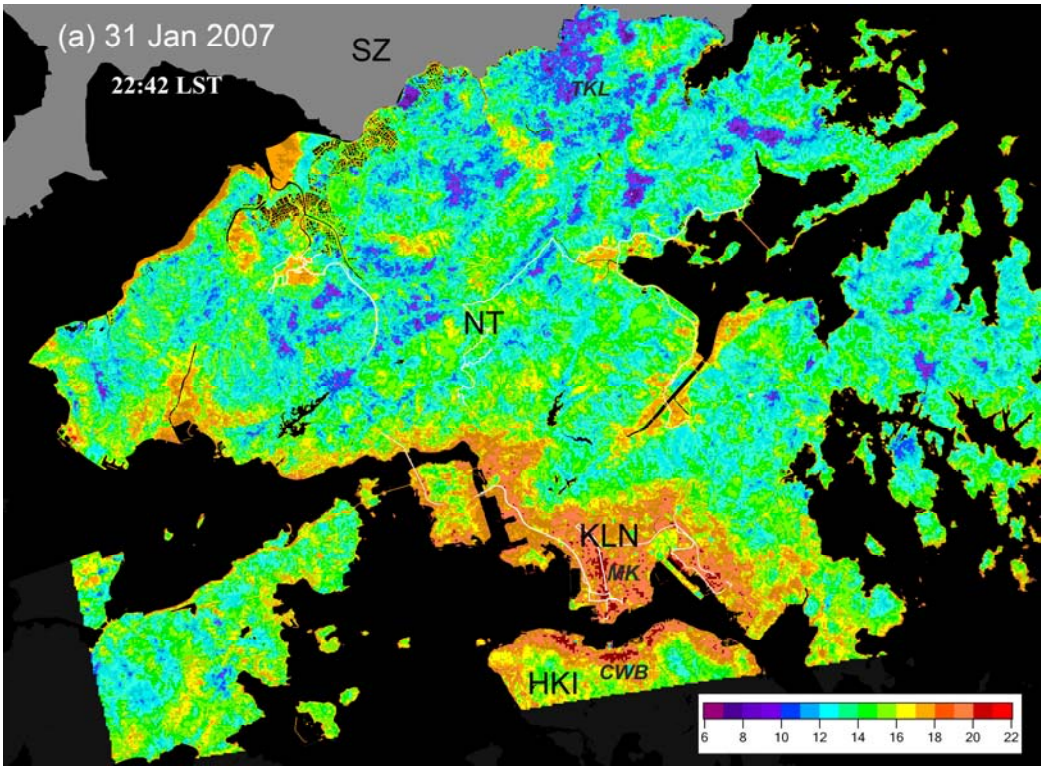
(a) 31 Jan 2007
22:42 LST
SZ
TKL
NT
KLN
MK
HKI
CWB
6 8 10 12 14 16 18 20 22
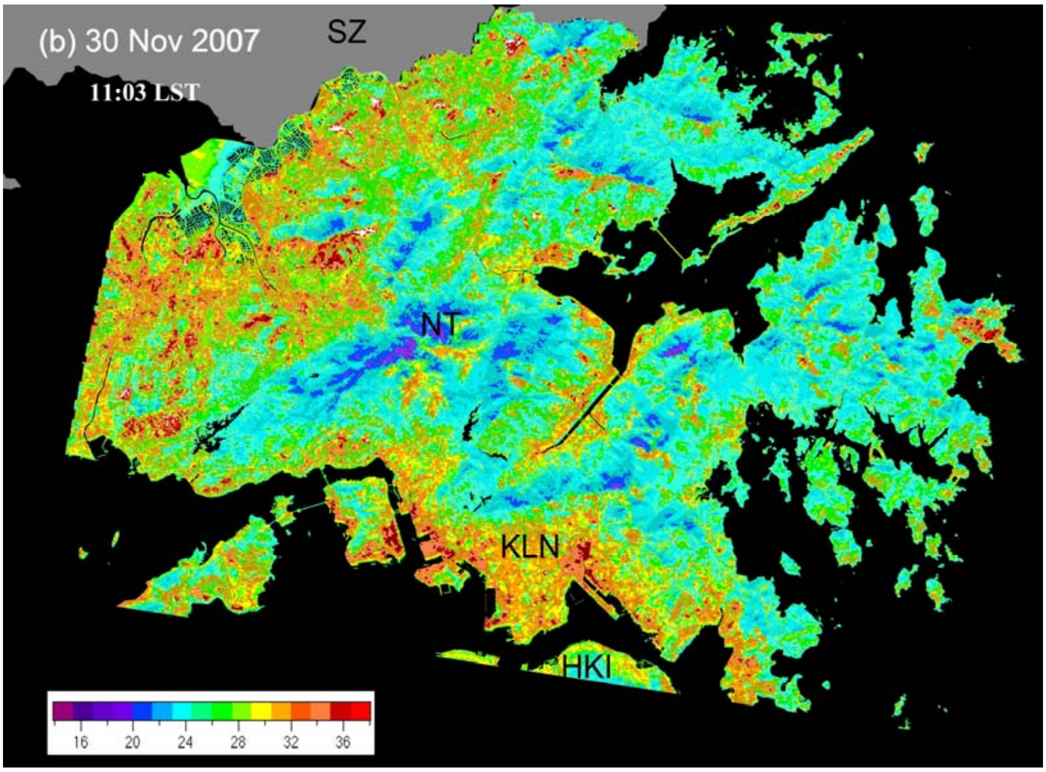
(b) 30 Nov 2007
11:03 LST
SZ
NT
KLN
HKI
16 20 24 28 32 36

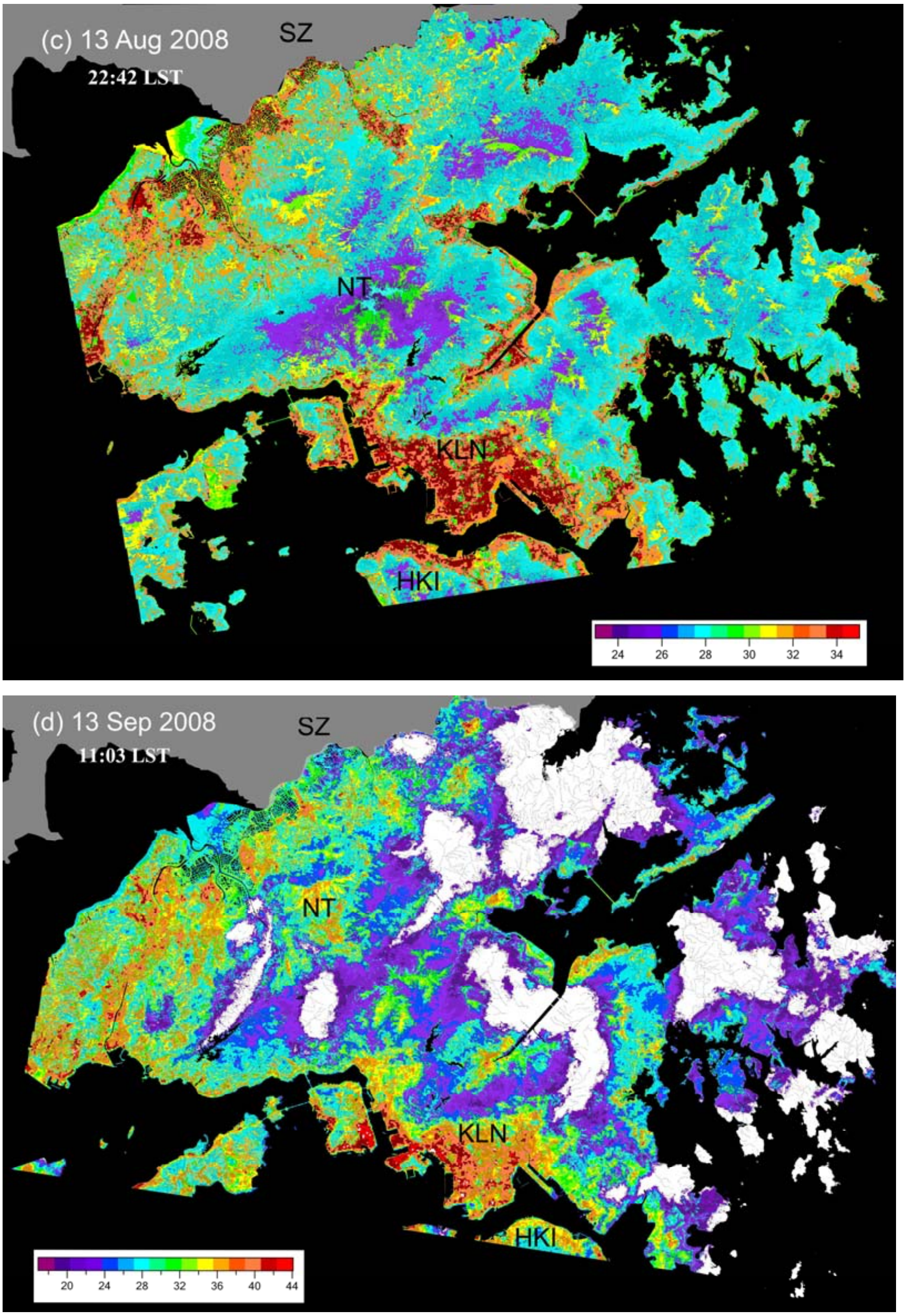

Figure 4.2 Satellite-derived surface temperature (a) at 22:42 local time on 31 January 2007; (b) at 11:03 local time on 30 November 2007; (c) at 22::42 local time on 13 August 2008 and (d) at 11:03 local time on 13 September 2008. Black / Grey color – No data. White color – Cloud effect. (SZ – Shenzhen; NT – New Territories; KLN – Kowloon; HKI – Hong Kong Island; *MK* – Mong Kok; *CWB* – Causeway Bay; *TKL* – Ta Kwu Ling)

Surface Heat Island study

The maximum nocturnal surface heat island intensities were 14.4^{o}C on 31 January 2007 and 8.8^{o}C on 13 August 2008. These maximum intensities were obtained in Kowloon Peninsula and were apparently different between winter and summer. In addition, maximum daytime surface heat island intensities were 14.2^{o}C on 30 November 2007 and 18.4^{o}C on 13 September 2008. Compared with the nocturnal results, these results are in agreement with many other surface heat island studies, which reported that the surface heat island intensity at daytime was larger no matter in winter and summer (Roth et al. 1989).

Different materials have different properties including the emissivity value and moisture content. This emissivity value will affect significantly the derivation of the surface temperature from satellite images, especially daytime images. Referring to the daytime image on 30 November 2007, the maximum surface temperature of 37.8^{o}C occurred in landfill site. Owing to the geometry of landfill, heat absorbed in different facades varied. The surface faced to the sun could absorb and emit much more the solar energy compared to other surfaces. In this study, only one emissivity value of 0.97 was used for all surfaces in such landfill. However, the emissivity value of 0.97 on identical landuse surfaces is assumed to be the same but the derived surface temperatures from these two facades could be different in a satellite image. For those surfaces not faced the sun, black body temperatures were lower than that of the surfaces faced to the sun. By applying Equation (3.5), there is a significance change of $T_{sat,suf}$ (around 2.3) if T_b changed from 10.88 to 10.52. It is likely that the satellite-derived surface temperatures have a discrepancy, especially on daytime images.

One short coming of this method is that it provides little information on seasonal variation. Clear sky image is rare particularly in spring in a subtropical city. Cloudy and humid weather condition block the view of the satellite sensors. Only two to three good images are available each year. These four episodes incidentally happened under a clear sky weather condition which probably recorded the extreme cases of heat island effect. It is difficult to conclude the seasonal change of surface heat island in Hong Kong using this approach.

Generally, the significance of using remote sensing technique in this study is to explore the coverage and the areal pattern of the heat island.

Urban heat island effect certainly exists in Hong Kong with solid evidences from both atmospheric and surface heat island field measurements, indicating higher intensity was generally recorded at night.

4.2 District UHII distribution

According to the mobile transverse measurement, two planned transverse routes covered seven districts out of 18. According to the geographical location from west to east, there are Sham Shui Po, Yau Tsim Mong, Kowloon Bay and Kwun Tong in Kowloon Peninsula; and Central and Western, Wan Chai and Eastern on Hong Kong Island. The mean of UHII among these districts are shown in Figure 4.3. Green boundary bars in Figure 4.3 represent UHII in Kowloon Peninsula while red boundary bars represent those on Hong Kong Island. From the statistical point of view, in the evening period, an overall UHII in Kowloon Peninsula was significantly higher than those on Hong Kong Island. In other periods, the differences in UHII were not statistically significant. This conclusion suggests that in the evening heat dispersion rate in Kowloon Peninsula may be slower than that on Hong Kong Island. This heat dispersion rate refers to a heat loss from urban surfaces to the atmosphere mainly by radiation, convection and conduction. From the topographic point of view, the buildings on Hong Kong Island are along Victoria Harbor while those in the western part of Kowloon Peninsula are perpendicular to the Harbor. The prevailing wind measured in Star Ferry station / King's Park is easterly due to the geometry of the harbor. As such, the wind was comparatively hard to puff away the heat generated in Kowloon Peninsula. Memon et al. (2010) also highlighted that importance of building aspect ratio and wind speed on urban heating.

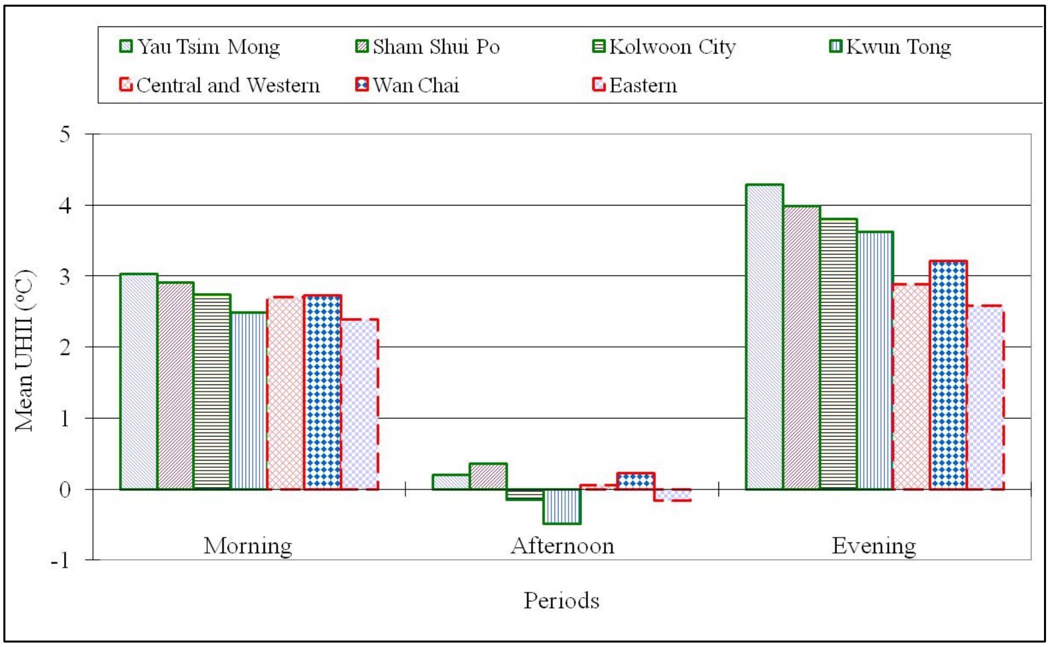

Figure 4.3 Mean values of UHII in different districts (each column represents one district UHII value)

Table 4.2 Maximum UHII and Population density in different districts (HK – districts on Hong Kong Island; Kln – districts in Kowloon)

Districts	Population	Density (population per km^2)	Max UHII (°C)	Ascending order of UHII
Wan Chai (HK)	155 196	15 489	3.2	3
Central & Western (HK)	250 064	19 973	2.9	2
Yau Tsim Mong (Kln)	280 548	40 956	4.4	7
Kowloon City (Kln)	362 501	36 359	3.9	5
Sham Shui Po (Kln)	365 540	38 559	4.0	6
Kwun Tong (Kln)	587 423	53 160	3.7	4
Eastern (HK)	587 690	31 243	2.6	1

Oke (1973) suggested that UHII increases with city population. As shown in Table 4.2, the most densely-populated district in Hong Kong is Eastern, but the UHII value was the smallest there. The highest UHII was recorded in Yau Tsim

Mong, and was followed by Sham Shui Po and Kowloon City. The population in these districts was around 300 thousand. Even though the population in these districts was not large, the heat island intensity was significant. This result implies that the maximum UHII is not highly correlated to the population in Hong Kong, but it seems to link with population density (Population per square kilometer) in each district. These densities are shown in the third column of Table 4.2. The results indicated that higher UHII (>3.3^{o}C) were recorded with an approximately population density of 35,000 or more. In general, the population density in Kowloon Peninsula was statistically greater than that on Hong Kong Island with p-value of 0.01. In addition, there was a significant evidence to support that the maximum UHII on Hong Kong Island was higher than those in Kowloon Peninsula. The p-value for a t-test was 0.005. For those districts in Kowloon Peninsula, buildings were tall and the building density was also high. One probable explanation for high intensity reading in high population density district may be that the capability of heat storage during daytime and energy emission at night is higher in high dense district. In short, this preliminary study proposes that UHII is likely correlated to the population density. Other possible parameters related the district UHII are energy consumption, heat release from cars, restaurants and industries, but those detail district data sets are not available. To further conduct a quantitative analysis, a comprehensive data survey and/or a data collection system should be conducted.

4.3 Integration of satellite thermal image with ground measurement

As mentioned in section 4.1.2, surface temperatures over Hong Kong were captured by the space satellite on four days. When the satellite passed over Hong Kong, a mobile transverse measurement was employed to measure ambient air temperatures, which were compared with the satellite-derived surface temperatures. Figure 4.4 illustrates mobile air temperature readings along two routes associated with the four satellite images. These readings are summarized in Table 4.3. Comparing two night episodes in winter and summer (Figure 4.4 (a) and (c)), the temperature ranged from 10.4^{o}C to 19.8^{o}C on 31 January 2007 and from 27.9°C to 32.3°C on 13 August 2008. The maximum temperature was measured in Kowloon Peninsula. The maximum temperature difference between the most urbanized area (Mong Kok, MK) and the less urbanization areas (Yuen Long YL and Sha Tin ST) was 9.4°C in winter and was about 4.4°C in summer. On the other hand, comparing two daytime episodes (Figure 4.4 (b) and (d)), the temperature ranged from 18.0°C to 24.1°C on 30 November 2007 and from 31.4°C to 39.2°C on 13 September 2008. Along the mobile route, the maximum temperature difference between the most urbanized area and the less urbanization areas was 6.1°C in winter and 7.8°C in summer. These data appear to support the interpretation that the microclimate does exist because a large temperature variation was observed in such a small land – Hong Kong.

(a) 31 January 2007 (Winter night)

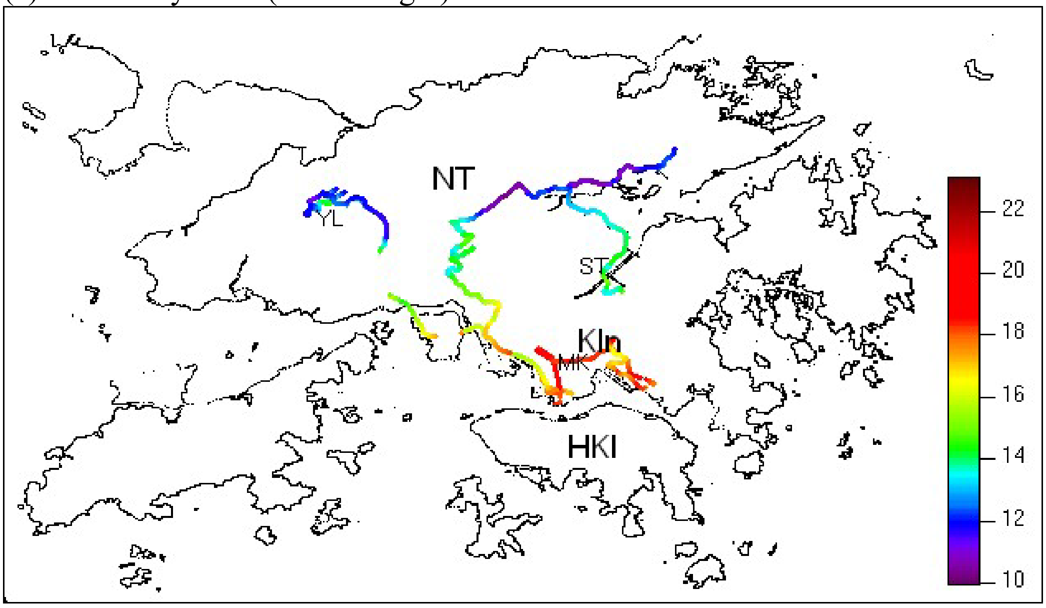

(b) 30 November 2007 (Winter Day)

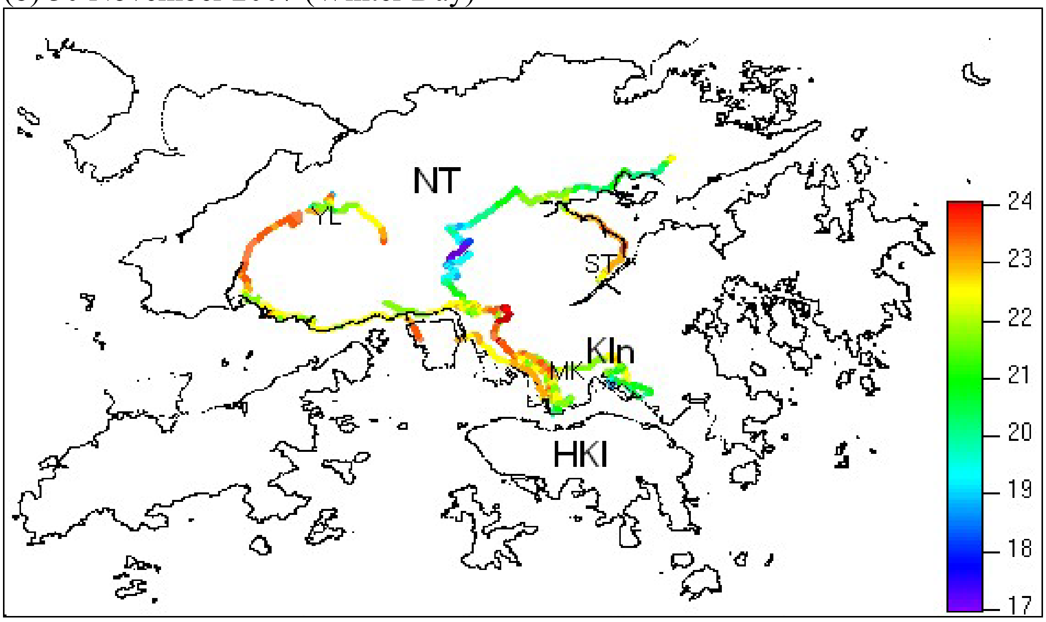

(c) 13 August 2008 (Summer Night)

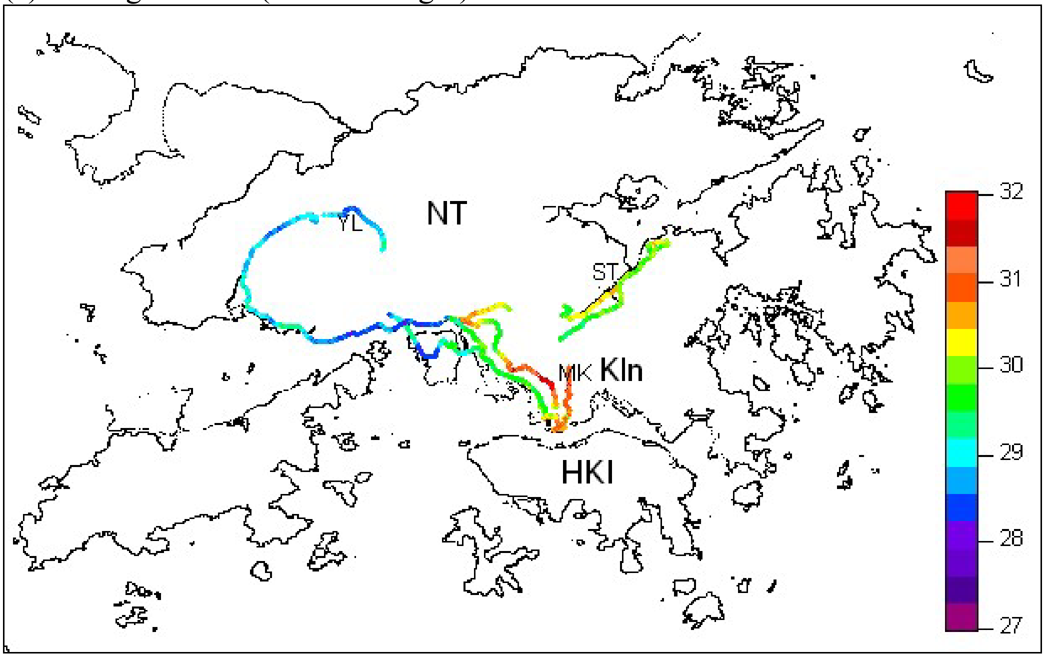

(d) 13 September 2008 (Summer Day)

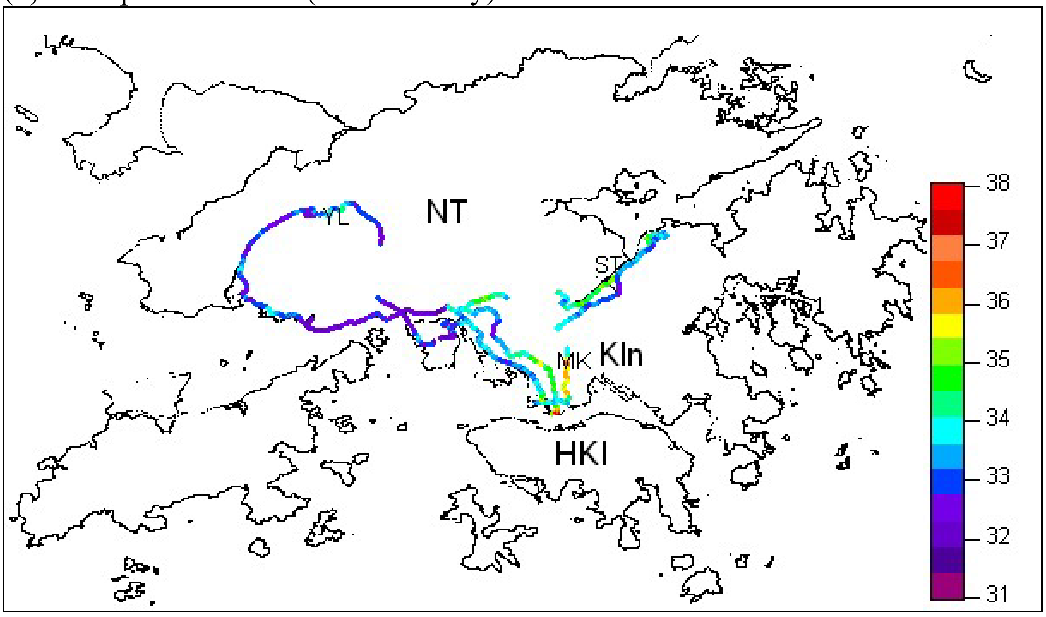

Figure 4.4 Overview of normalized mobile air temperature readings along two mobile routes at four episodes (a) at 22:42 local time on 31 January 2007; (b) at 11:03 local time on 30 November 2007; (c) at 22::42 local time on 13 August 2008 and (d) at 11:03 local time on 13 September 2008 (NT – New Territories; Kln – Kowloon; HKI – Hong Kong Island)

Table 4.3 Summary of mobile air temperature and satellite-derived surface temperature along the two routes at four episodes

Date and Time	Mobile air temperature			Satellite-derived surface temperature		
Overall	**Max.**	**Min.**	**Avg.**	**Max.**	**Min.**	**Avg.**
31 January 2007, 22:42 LT	19.8	10.4	15.1	21.2	10.8	16.7
30 November 2007, 11:03 LT	24.1	18.0	21.2	37.5	16.9	27.8
13 August 2008, 22:42 LT	32.3	27.9	29.9	34.9	26.2	32.7
13 September 2008, 11:03 LT	39.2	31.4	33.6	41.6	25.6	35.0
Urban						
31 January 2007, 22:42 LT	19.8	17.1	18.4	21.2	15.4	19.3
30 November 2007, 11:03 LT	23.4	18.0	21.0	35.6	16.9	27.2
13 August 2008, 22:42 LT	32.3	29.1	30.5	34.9	26.2	32.8
13 September 2008, 11:03 LT	39.2	31.8	34.3	40.9	25.8	34.8
Suburban						
31 January 2007, 22:42 LT	17.5	10.4	13.5	19.8	10.8	15.6
30 November 2007, 11:03 LT	24.1	19.7	21.6	37.5	20.2	28.8
13 August 2008, 22:42 LT	31.1	27.9	29.1	34.8	27.8	32.5
13 September 2008, 11:03 LT	35.7	31.4	33.0	41.6	25.6	35.1

Figure 4.5 plots both mobile air and satellite-derived surface temperatures along the two routes. Red lines represent mobile air temperatures while dot grey lines represent satellite-derived surface temperatures. A summary of mobile air temperatures and satellite-derived surface temperatures is listed in Table 4.3. In general, the satellite-derived surface temperatures were slightly higher than the mobile air temperatures in urban areas. This difference was larger in suburban area. The average temperature difference between the mobile air temperature and the satellite-derived surface temperature was 2.5^{o}C in urban area and 3.7^{o}C in suburban area respectively. These data appear to support a correlation between mobile air temperatures and satellite-derived surface temperature and this correlation varies in different land covers. There are at least two classes of land

covers – urban and suburban areas. The ambient temperature could be then derived from the satellite-derived surface temperature.

(a) 31 January 2007, at 22:42 LST

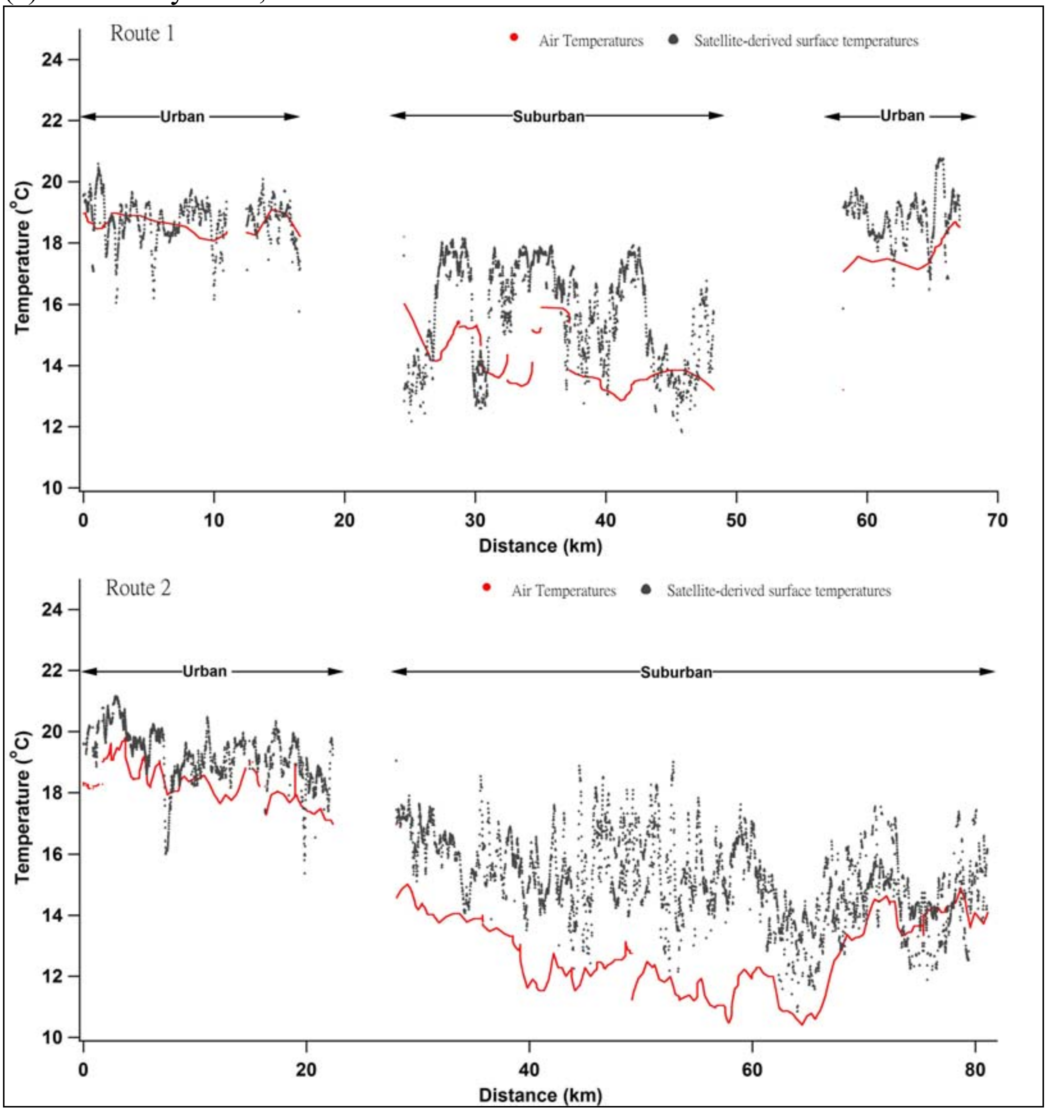

(b) 30 November 2007, at 11:03 LST

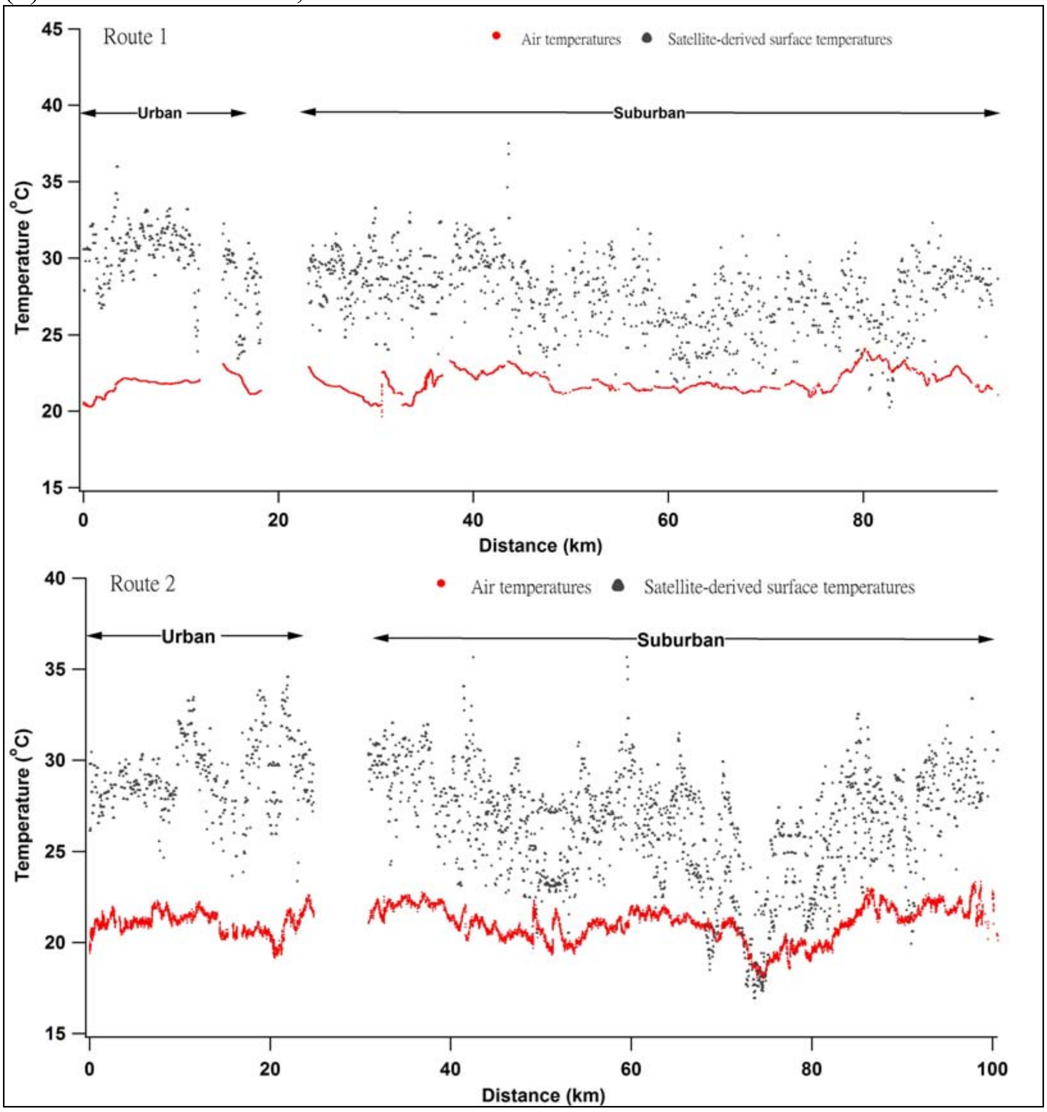

(c) 13 August 2008, at 22:42 LST

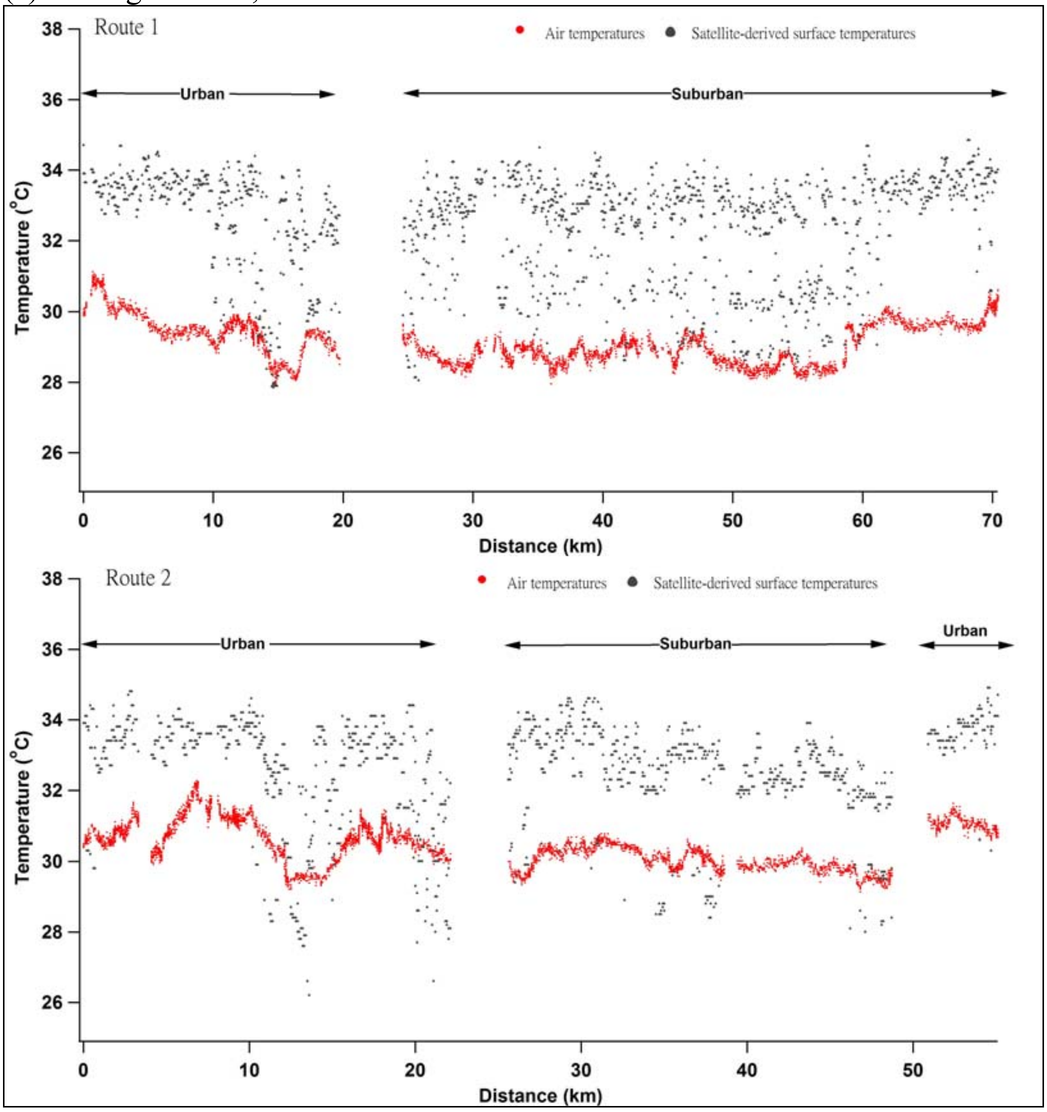

(d) 13 September 2008, at 11:03 LST

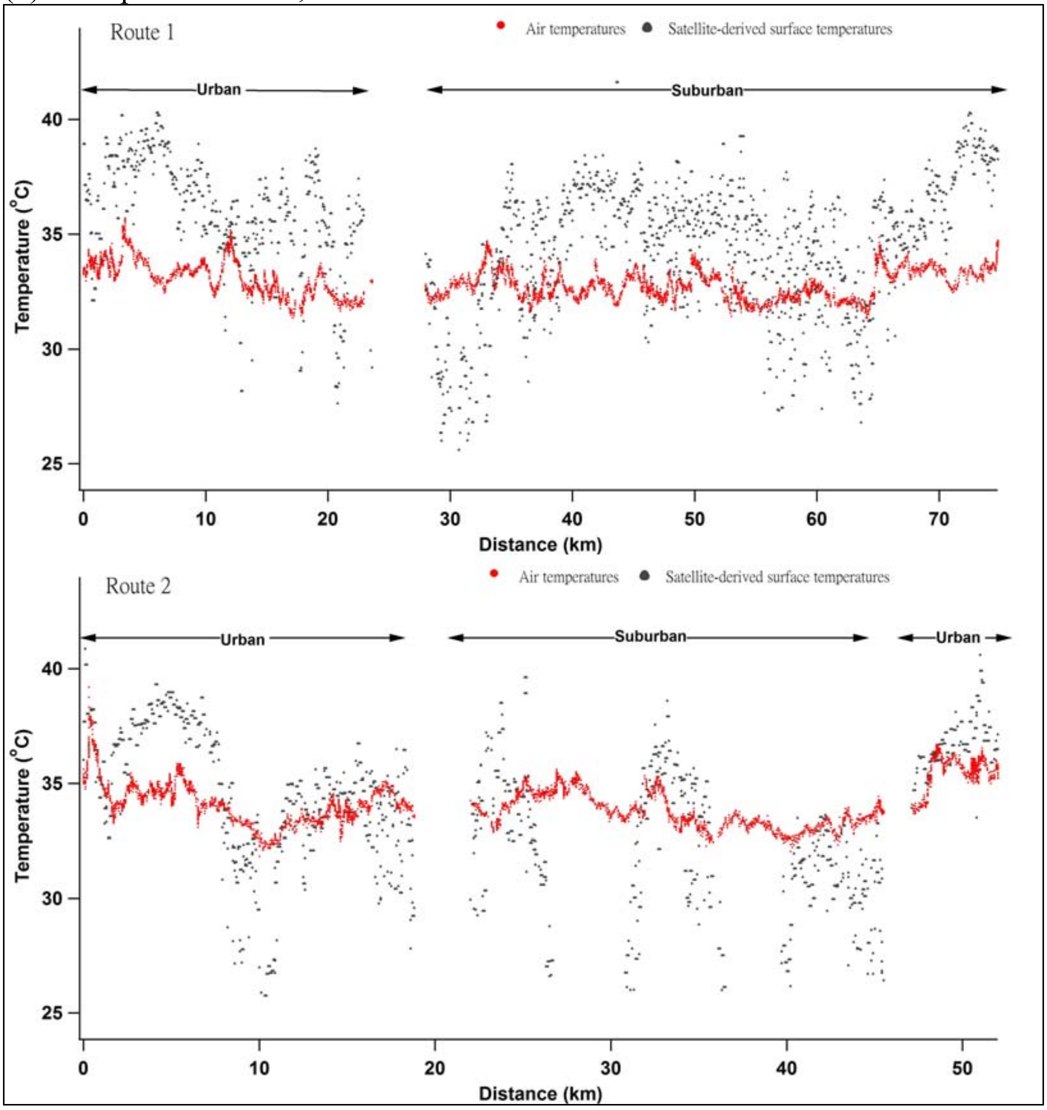

Figure 4.5 Comparison of measured mobile air temperatures from mobile traverse across urban and rural areas, with satellite-derived surface temperatures (a) at 22:42 local time on 31 January 2007; (b) at 11:03 local time on 30 Nov 2007; (c) at 22:42 local time on 13 Aug 2008 and (d) at 11:03 local time on 13 Sep 2008, according to distance recording. Breaks in the data represent driving through tunnels

4.4 Chapter summary

The results of this chapter confirm the existence of urban heat island in Hong Kong using a series of mobile transverse measurement and four remote sensing images. Both atmospheric and surface heat island studies were conducted in Hong Kong. According to 20 mobile transverse measurements, the maximum heat island occurred in the evening. The atmospheric heat island results in the evening were consistent with those of the surface heat island study. In addition, different heat island intensities recorded among seven urban districts suggest that population density can be one of the factors causing higher temperature readings in Kowloon Peninsula.

An important suggestion in this chapter is a need for deriving ambient temperatures from surface temperatures. According to the four episodes experiments (mobile transverse measurement synchronized with satellite images), a correlation relationship between ambient and surface was identified at two classes of land covers – urban and suburban areas. A detailed derivation of the ambient temperature from satellite images is discussed in section 5.3.

Chapter 5 : Correlation between surface temperature and near surface air temperature

5.0 Outline

In this chapter, the accuracy of the satellite-derived surface temperatures are discussed in section 5.1. Section 5.2 outlines the correlation between surface temperatures and air temperatures. Section 5.3 demonstrates one nighttime satellite-derived air temperatures image. Section 5.4 lists linear empirical equations for converting surface temperatures to ambient air temperatures under different weather conditions. Section 5.5 lists linear empirical equations for converting hourly surface temperatures to ambient air temperatures over grass and concrete surfaces. The summary of this chapter are given in section 5.6.

5.1 "Accuracy" of satellite-derived surface temperatures

The integration of in-situ ground measurements together with satellite overpass provides a unique opportunity to validate the satellite thermal image and to find out the correlation between ambient and surface temperatures. During the field measurements, ground surface temperatures were recorded at different locations within 1-2 hour while the satellite passed over. There were a total of 103 pairs of satellite-derived surface temperatures, and in-situ surface temperatures recorded in 41 sites on the four episode days. A scattered diagram of these two temperatures is shown in Figure 5.1. Linear regression showed that the coefficient of determination (R^2) was 0.80; the standard error (ε) was 4.2 and the corresponding p value was 0.000 at 5% significance level. The correlation between the two temperatures was good. An individual R^2 and ε were different among four selected days. On 31 January 2007, the R^2 and ε were 0.73 and 1.4 respectively. On 30 November 2007, the R^2 and ε were 0.03 and 4.4 respectively. On 13 August 2008, the R^2 and ε were 0.17 and 1.6 respectively. On 13 September 2008, the R^2 and ε were 0.24 and 3.7 respectively. In general, there was a good correlation found on 31 January 2007, not on other days. On 31 January 2007, the ground surface temperature was slightly overestimated by the satellite image. The results can also indicate an expected good correlation between satellite-derived surface temperatures and in-situ surface temperatures.

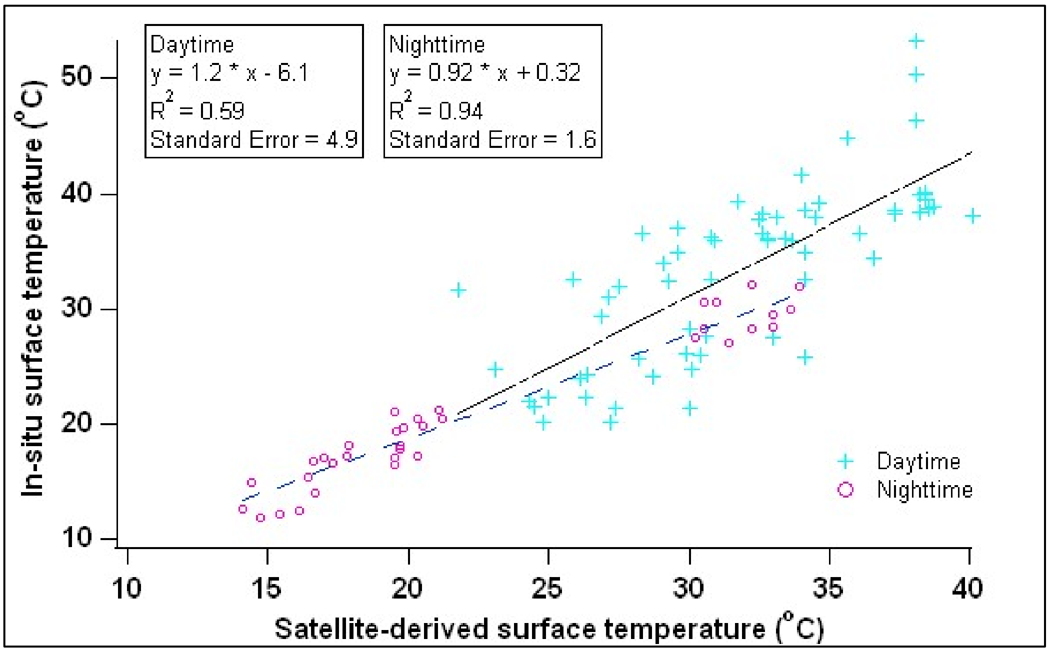

Figure 5.1 Correlation between in-situ surface temperature and satellite-derived surface temperature on four selected days

A crude estimate of the accuracy and precision of the satellite-derived surface temperature can be obtained. If we define 'd' as the difference between the satellite-derived temperature and the in-situ temperature, the root mean square of 'd' was about 1.6°C for night images and about 4.9°C for daytime images. If two standard deviations of 'd' is taken as the precision, these are 3.2°C for night images and 9.8°C for daytime images respectively. The R^2 was 0.94 at two nighttime images and it was 0.59 at two daytime images. This finding appears conceivable that the discrepancy of nighttime satellite-derived surface temperatures was less. One likely explanation is that a thermal conduction principle of land surfaces is relatively simple at night. The influence of solar radiation existed during daytime is minimized after the sunset and long-wave radiation emission dominates the heat loss at night.

5.2 Temperature correlation

5.2.1 Correlation between in-situ air and in-situ surface temperatures

From the ground field measurements, 103 pairs of in-situ air and surface temperatures were also recorded. Figure 5.2 shows a scattered plot diagram of the in-situ air temperatures against the in-situ surface temperatures on the four episode days. Linear regression showed that the coefficient of determination (R^2) was 0.84 and the p value was 0.000. The correlation between the two temperatures was strong. Individual R^2 values were 0.77 on 31 January 2007, 0.15 on 30 November 2007, 0.11 on 13 August 2008 and 0.27 on 13 September 2008 accordingly. In addition, the overall R^2 was 0.74 in daytime and was 0.95 in nighttime. These data further support the interpretation in section 4.3 that the correlation between ambient and surface temperatures exists over different types of land covers.

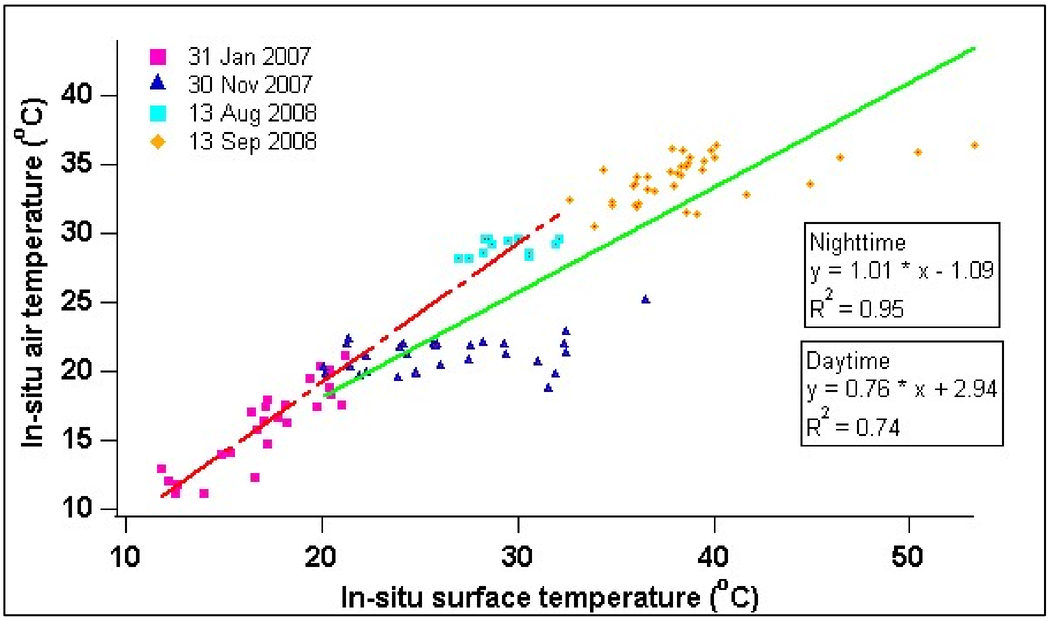

Figure 5.2 Correlation between in-situ air temperature and in-situ surface temperature on four episode days

5.2.2 Correlation between mobile air and satellite-derived surface temperatures

Figure 5.3 shows a scattered plot diagram of the air temperature acquired by mobile vehicle against the satellite-derived surface temperature on the four episode days. This individual plot can demonstrate a comparison of satellite-derived surface temperatures with a large sample size. Linear regression showed that the coefficients of determination R^2 were 0.70 on 31 January 2007, 0.14 on 30 November 2007, 0.15 on 13 August 2008 and 0.11 on 13 September 2008. The sample sizes on these four days were 14815, 12799, 8964 and 8848 accordingly. It appears that there is barely a correlation between satellite-derived surface temperature and mobile air temperatures due to too many data. Nevertheless a simple linear regression could still be performed.

(a) 31 January 2007

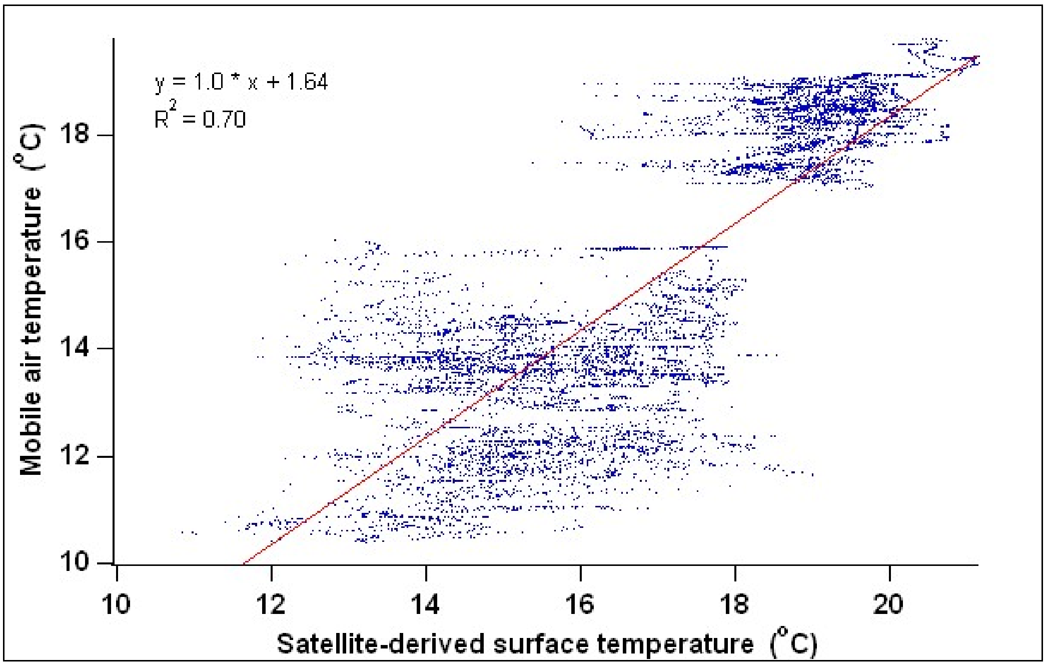

(b) 30 November 2007

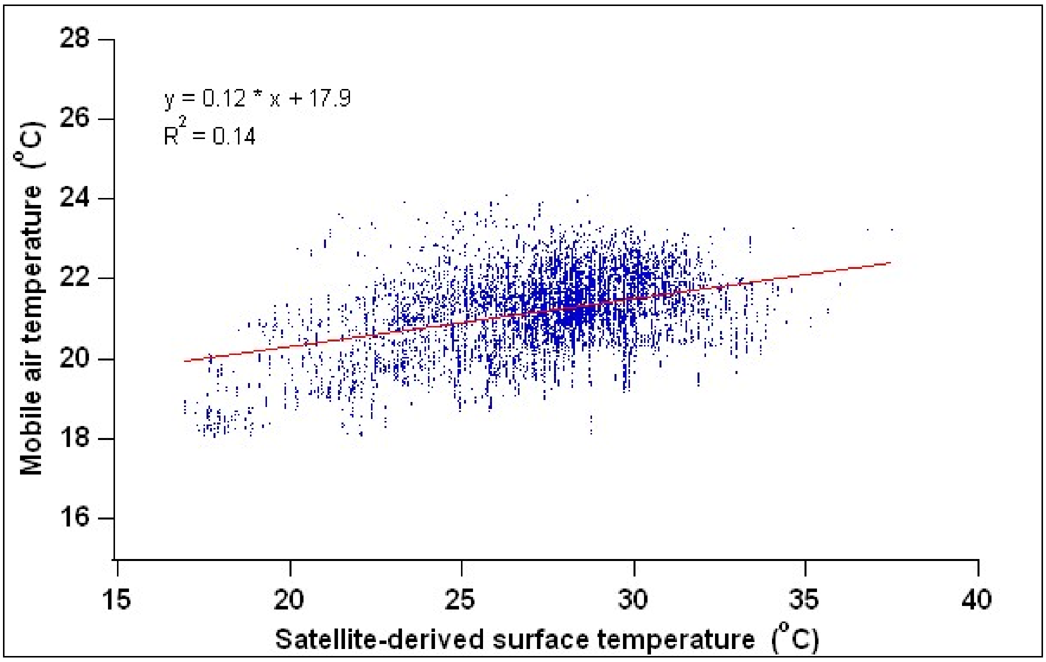

(c) 13 August 2008

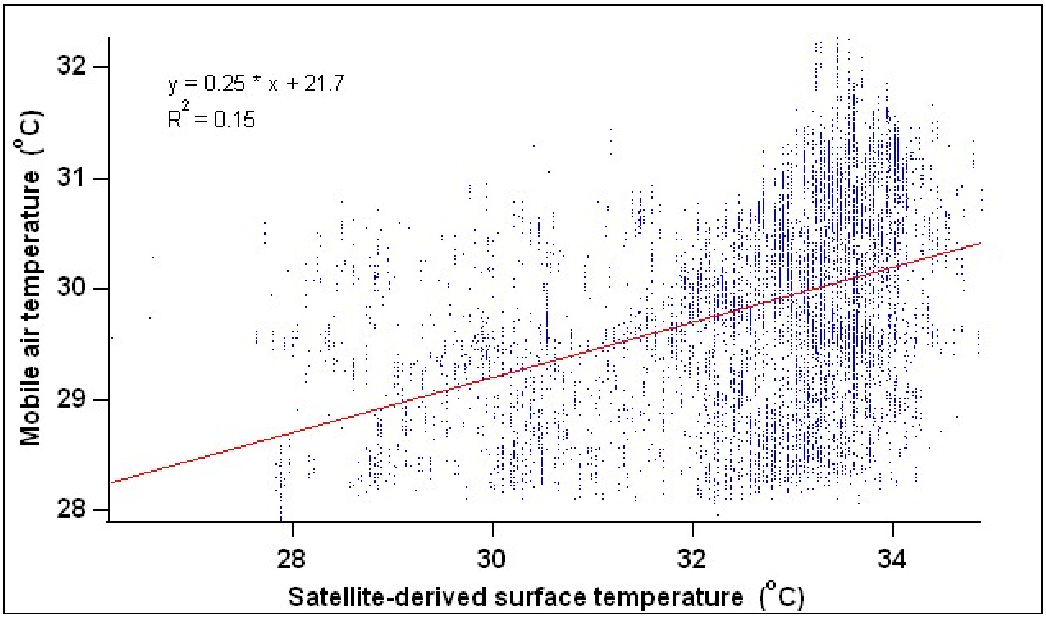

(d) 13 September 2008

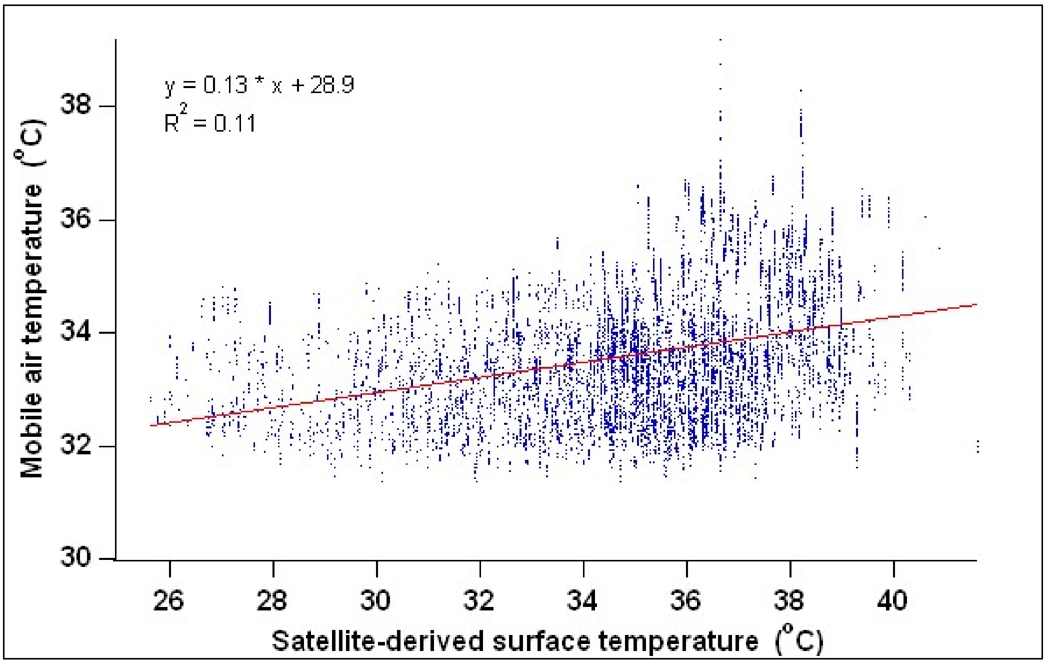

Figure 5.3 Correlation between satellite-derived surface temperatures and mobile air temperatures (a) on 31 January 2007; (b) on 30 November 2007; (c) on 13 August 2008 and (d) on 13 September 2008

5.2.3 Correlation over concrete and grass surfaces

To further explore the correlations among urban and suburban areas, in-situ temperature acquired during the four episodes are extracted and grouped according to the two land covers, which are concrete surface and grass surfaces. Sample size was 49 and 27 over these two land covers respectively. Figure 5.4 shows the scattered diagram of in-situ air temperature against in-situ surface temperature over two surfaces of concrete and grass. The overall R^2 were 0.83 over grass surface and 0.79 over concrete surface respectively. This infers that the temperature correlation exists over grass and concrete surfaces and the change of land covers certainly affects the thermodynamics above the surfaces.

(a) Grass surface

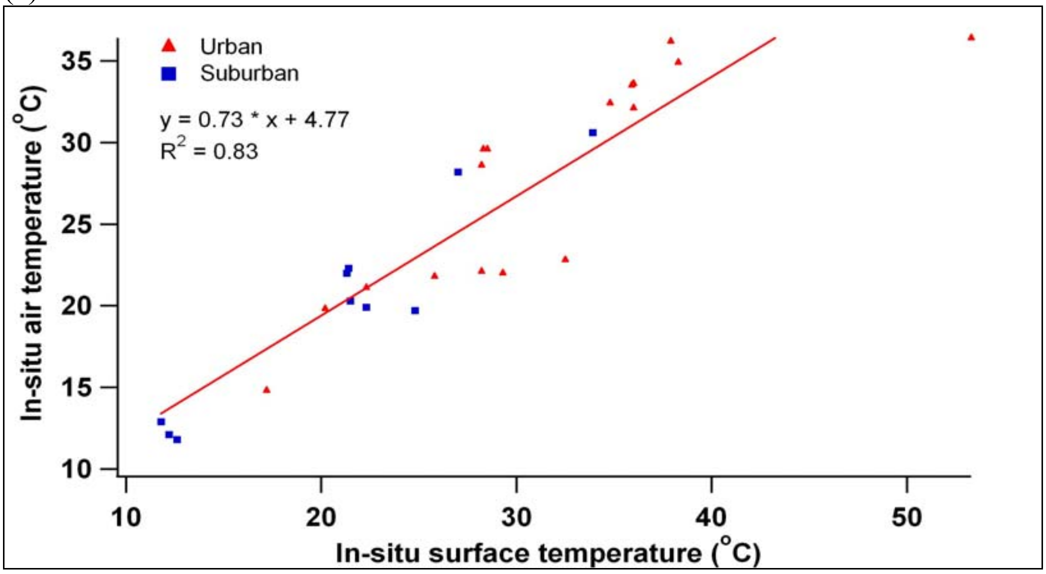

(b) Concrete surface

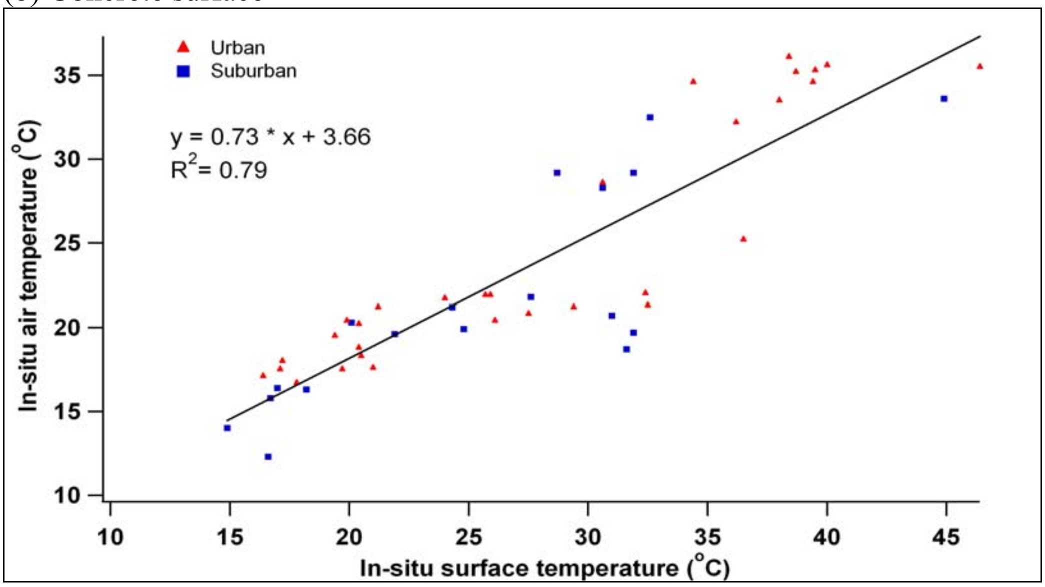

Figure 5.4 Correlation between in-situ air temperature and in-situ surface temperature over (a) grass surface and (b) concrete surface

5.3 Satellite-derived air temperatures

5.3.1 Conversion of satellite-derived surface temperature into satellite-derived air temperatures

An attempt to obtain the satellite-derived air temperature was carried out using the satellite image on 31 January 2007 (see Figure 4.2 (a)). The satellite-derived surface temperature, except water surface, was first converted to an in-situ surface temperature using the linear correlation regression described in section 5.1. The regression equation was $T_{insitu,suf} = T_{sat,suf} * 1.16 - 3.95$ (Figure 5.5). This was then converted to a satellite-derived air temperature using the linear correlation regression reported in section 5.2.1 and the corresponding extracted scattered diagram is shown in Figure 5.6. The overall regression equation was $T_{sat,air} = T_{insitu,suf} * 0.93 + 0.13$. The combined empirical equations for the conversion of satellite temperatures are:

For all data (n = 25):

$T_{sat,air} = 1.07 * T_{sat,suf} - 3.5$ (5.1)

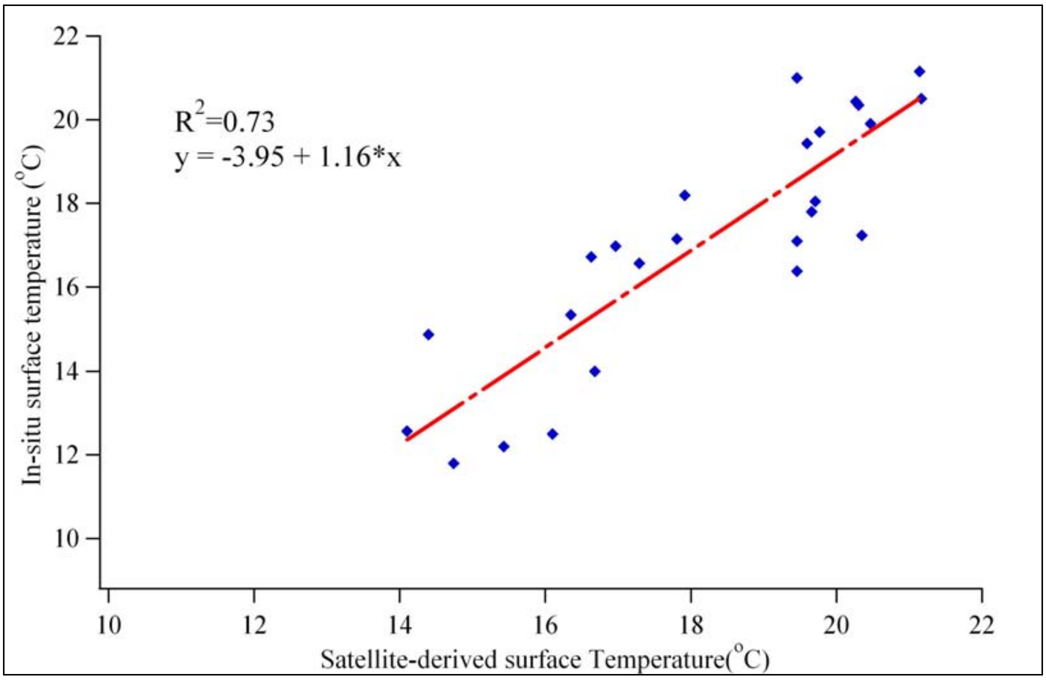

Figure 5.5 Correlation between in-situ surface temperature $T_{insitu,\,suf}$ and satellite-derived surface temperature $T_{sat,suf}$ on 31 January 2007

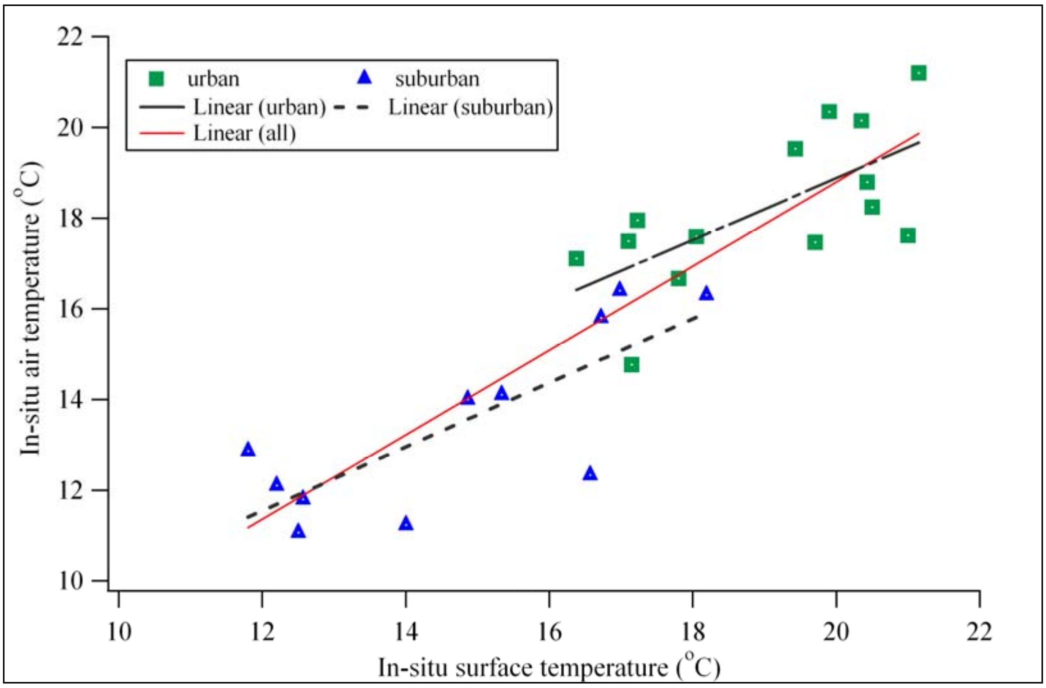

Figure 5.6 Correlation between in-situ air temperature $T_{insitu,air}$ and in-situ surface temperature $T_{insitu,suf}$

The above conversion was then repeated by splitting the territory into urban and suburban using both Equations (5.2) and (5.3). The second conversion used Equation (5.2) on urban pixels and Equation (5.3) on non-urban pixels.

For urban locations (n = 14):

$$T_{sat,air} = 0.79 * T_{sat,suf} + 2.6 \qquad (5.2)$$

For suburban locations (n = 11):

$$T_{sat,air} = 0.82 * T_{sat,suf} + 0.3 \qquad (5.3)$$

where $T_{sat,air}$ is the satellite-derived air temperature

$T_{sat,suf}$ is the satellite-derived surface temperature

The above equations should be used with caution as the number of sampling is not large, and they represent results from only one winter night. More data from future work in the same season will improve our understanding of this correlation.

The validity of the three empirical equations can be studied by comparing the satellite-derived air temperatures with the reasonable size of the air temperature data acquired by mobile vehicles (also called as mobile air temperature). The temperature records measured from mobile observation is summarized in Table 4.3. When Equation (5.1) was used, the overall average satellite-derived air temperature was about 0.5^{o}C lower than the mobile air temperature. A more detailed examination shows that Equation (5.1) performed better in suburban areas. The discrepancy mainly occurred in the urban areas where the difference amounted to 1.2^{o}C. When the conversion treated urban and suburban areas separately using Equations 5.2 and 5.3, the difference between the satellite-derived air temperature and the mobile air temperature was reduced slightly to 0.2^{o}C. On average, the temperature difference was about 0.7^{o}C in the urban areas and 0.0^{o}C in the suburban areas. In addition to the above findings, the overall R^2 between the satellite-derived air temperature and mobile air temperature improved from 0.63 (Equation (5.1)) to 0.70 (Equations (5.2) and (5.3)) at the 5% significance level. Therefore, there is a benefit in treating urban and suburban areas separately in the analysis. The image of the satellite-derived air temperature is shown in Figure 5.7.

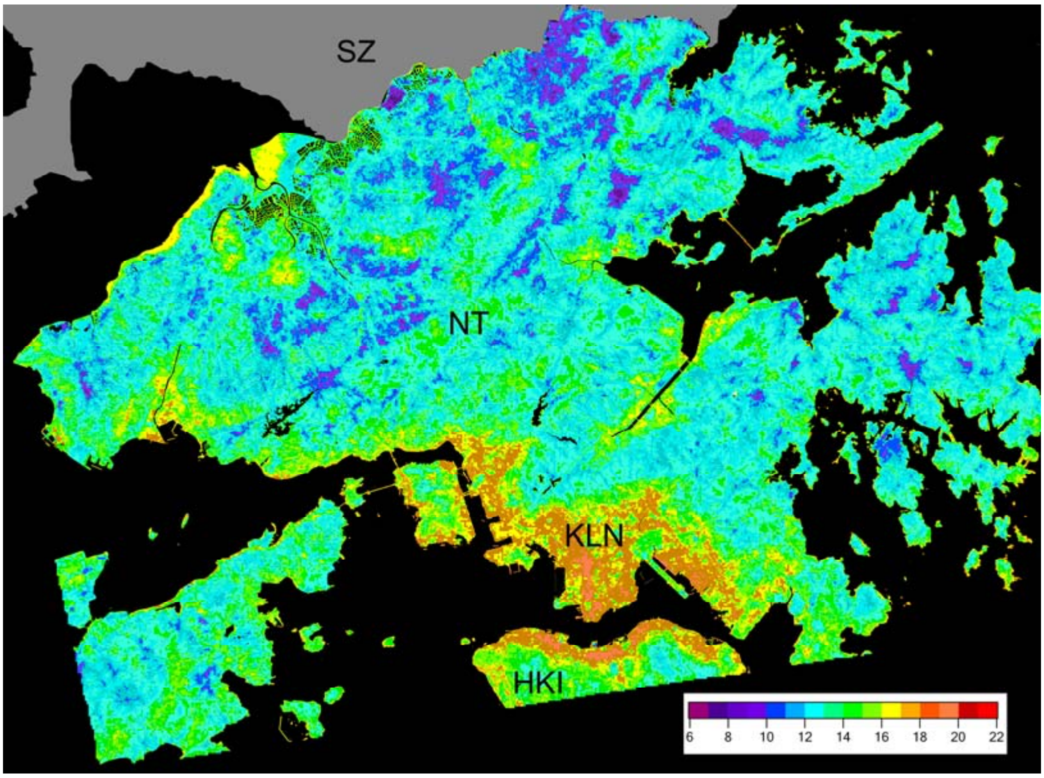

Figure 5.7 Satellite-derived air temperature at 22:42 local time on 31 January 2007. Black / Grey color – No data. (SZ – Shenzhen; NT – New Territories; KLN – Kowloon; HKI – Hong Kong Island)

As shown in Figure 5.7, the range of the satellite-derived air temperature was between 7.3^{o}C and 19.4^{o}C. In the urban areas, the satellite-derived air temperature ranged from 14.7^{o}C to 19.4^{o}C. In the suburban areas, it ranged from 7.3^{o}C to 17.9^{o}C. The lowest satellite-derived air temperature (7.3^{o}C) was located in the vicinity of the reference point (TKL). Thus, the maximum UHII of 12.1^{o}C was observed on the night of 31 January 2007.

5.3.2 A comparison of satellite-derived air temperature against fixed station observations

Meteorological station data (hereinafter called HKO air temperature) was used to further test the satellite-derived air temperature. 12 HKO station observed air temperatures were available for comparison. The HKO air temperatures were observed on the same night, and at approximately same time during the satellite overpass. Figure 5.8 shows the scattered diagram between HKO air temperature and satellite-derived air temperature. The correlation is good, with an overall coefficient of determination of 0.66. The standard error of this correlation was 1.4. This good correlation indicates that this temperature conversion method is applicable on a winter night.

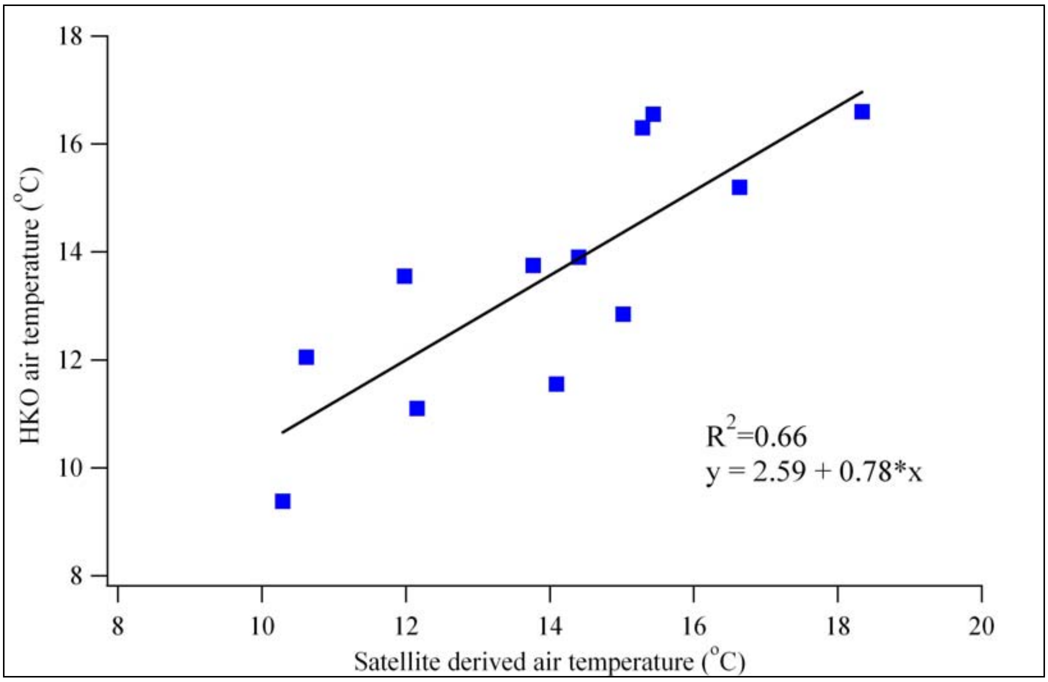

Figure 5.8 Correlation between HKO air temperature and satellite-derived air temperature

5.4 Empirical equations between ambient air temperatures and surface temperatures under different weather conditions

It is not clear from the previous sections that a correction between ambient temperature and surface temperatures does exist. A 2-year intensive study was conducted to examine 1) any existence of correlation between surface temperature and air temperature and 2) search for meteorological factors affecting the relationship between surface temperatures and ambient temperatures. A long-term measurement of surface temperatures and surface air temperatures at two fixed stations confirms that there is a good correlation between the two temperatures over a fix point. The empirical equations for their correlation were then found under different weather conditions, especially in low wind days.

<u>Existence of surface and air temperature correlation over a fix ground surface</u>

In this study, hourly ambient temperatures at two stations were recorded for 2 years (2006 -2007). One urban station was located at Mong Kok (MK) and one suburban station was located at Hok Tsui (HT). The grounds at two stations were both concrete paved. At each station, three temperature readings were measured, one at ground level, the second at 0.05 m above the ground and the third at 1.5m above the ground. In this study, the temperature at ground surface is called as surface temperature, the 0.05 m above ground is called surface air temperature and the 1.5 m above ground is called ambient air temperature.

The correlation between surface air and surface temperatures at two stations was then examined. Figure 5.9 depicts the scattered diagram of the surface air temperatures against the surface temperatures over the concrete surfaces at two stations. Red squares give the correlation between two temperatures in summer and green triangles represent its correlation in winter. An excellent correlation was found in both stations. The R^2 at the MK station was almost 1.0 at 5% significance level. The R^2 at the HT station was 0.96.

(a) Mong Kok, MK

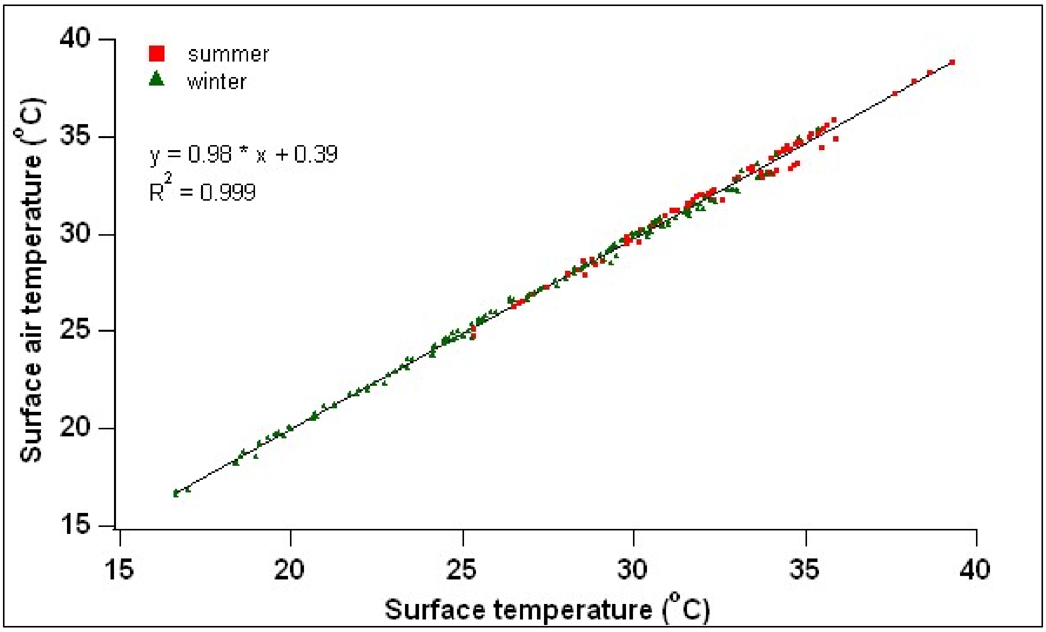

(b) Hok Tsui, HT

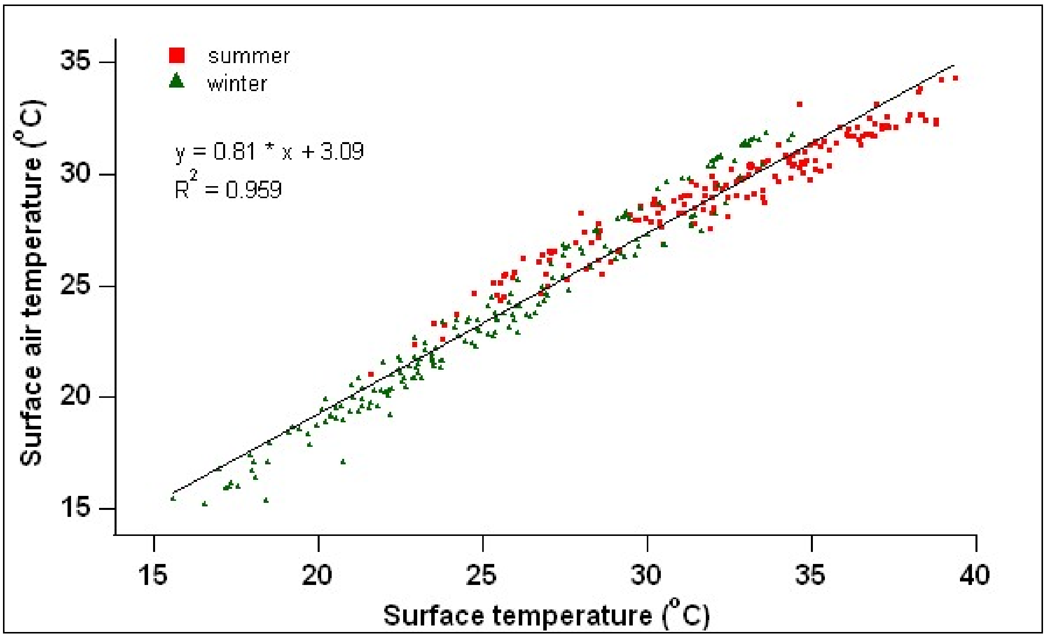

Figure 5.9 Scattered diagram of surface air temperatures against surface temperatures over concrete surfaces at (a) Mong Kok MK urban station; (b) Hok Tsui HT suburban station

Linear regression was continued to explore the correlation between surface temperatures and ambient air temperatures. Figure 5.10 shows the scattered diagram of daily ambient air temperature against surface temperature over concrete surfaces at two stations. The determination of correlation (R^2) at urban station (MK) was 0.88 and its value at the suburban station (HT) was 0.92. Compared to the correlation between surface and surface air temperatures, the linear correlation was weaker due to the turbulent flow above the ground, but the correlation is still good. To explain the weaker correlation, effect of wind speed was further studied.

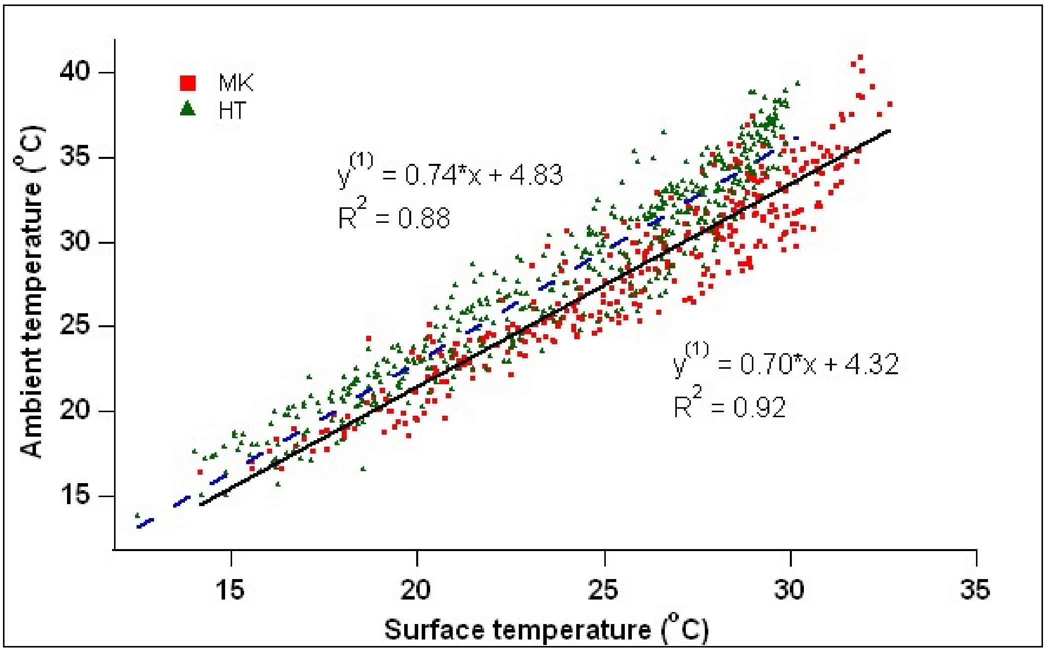

Figure 5.10 Scattered diagram of ambient air temperatures against surface temperatures over concrete surfaces at two stations (MK – Mong Kok urban station; HT – Hok Tsui suburban station) [$^{(1)}$ means the trend satisfied 5% significance level]

<u>Low wind days</u>

Past studies report the existence of correlation between ambient air and surface temperatures in calm days. At the MK urban station, the average daily wind speed was below 2.0 ms^{-1}. This temperature correlation could be discussed under two wind speed classes. The first class was the temperature data under less than 1.0 ms^{-1} wind speed; the second class was the data with wind speed between 1-2 ms^{-1}. As shown in Figure 5.11, the temperature correlation between ambient air and surface temperature is displayed for these two classes. Table 5.1 lists their empirical equations for the two classes and for the whole data set. In general, R^2 of the regression decreased with wind speed. The finding implies that the temperature correlation is better when average wind speed is below 1.0 ms^{-1}. It should be noted that empirical equations can be applied over concrete surfaces in urban areas, where the wind speed is low. In the case of heat island intensity, the wind speed is usually below 3 ms^{-1}. The empirical equations introduced in this section can help to derive ambient air temperatures from surface temperatures in urban areas in calm days.

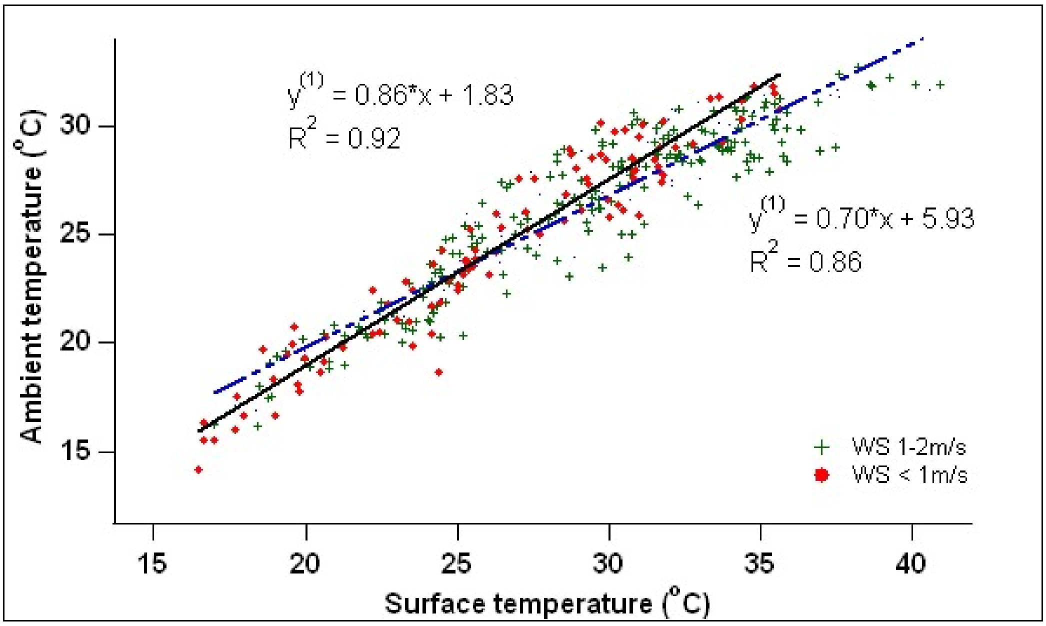

Figure 5.11 Scattered diagram of daily ambient temperature against surface temperature in the MK urban station [$^{(1)}$ means the trend satisfied 5% significance level]

Table 5.1 Summary of empirical equations between ambient and surface temperatures in different wind speed conditions

		$T_{air} = A*T_{suf} + B$	
	R^2	A	B
Data set with			
- WS < 2m/s	0.883	0.739	4.83
- WS 1-2 m/s	0.863	0.696	5.93
- WS < 1m/s	0.924	0.858	1.83

5.5 Empirical equations between ambient air temperatures and underground temperatures over different surfaces

A 1-year intensive temperature measurement was conducted from March 2007 to February 2008 in Ta Kwu Ling (TKL). This measurement including four underground temperatures and two ambient temperatures was set up over grass surfaces and the set-up was moved over the concrete surface in August 2007. Hourly underground soil temperatures were measured in the depth of 0.05 m, 0.2 m, 0.5 m and 1.25 m (abbreviated in T_{-5}, T_{-20}, T_{-50}, T_{-125} respectively). Daily temperatures were computed by 24 hour average. Two ambient temperatures were also recorded 1.8 m and 0.2 m above the ground. A correlation between the underground temperature 0.05 m below the ground temperature (T_{-5}) and other three temperatures ($T_{180,}$ $T_{20,}$ T_{-15}/ T_{-20}) was analyzed.

5.5.1 Grass surfaces

The scattered diagram of daily mean ambient temperatures against the reference surface temperature T_{-5} over the grass surface is shown in Figure 5.12. A considerable good correlation ($R^2 > 0.95$) was found during the cold season over grass surface in TKL. During the hot season, the correlation was reduced to 0.75. One of the possible explanations is that vertical heat convection above the surface is stronger during the hot season. A turbulent flow can diminish a heat transmission from the ground surface to the upper level. The above empirical equations are based on daily mean. A derivation of hourly empirical equations is required.

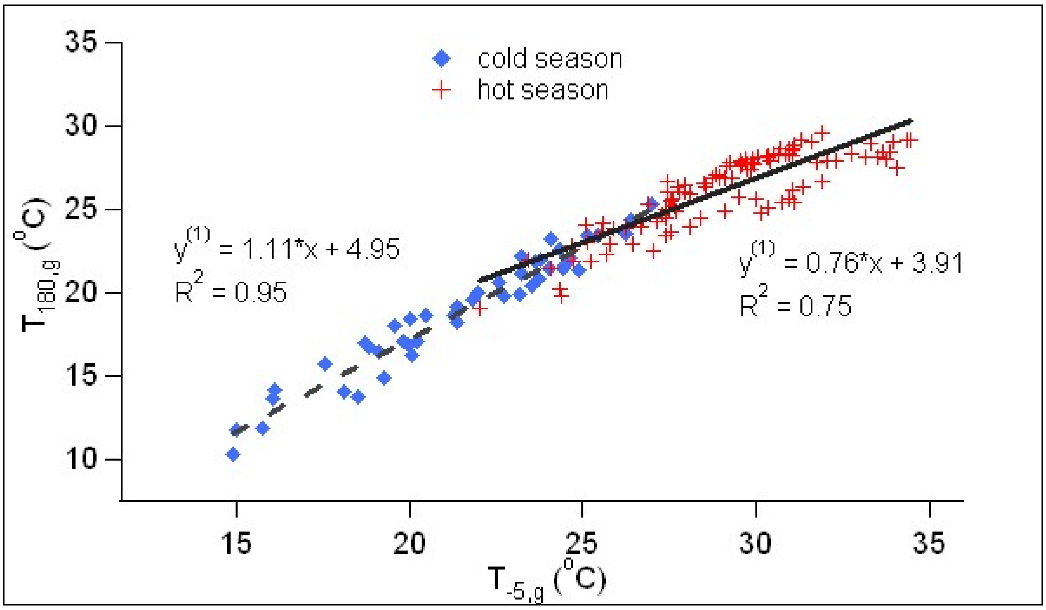

Figure 5.12 Scattered diagram of daily mean ambient temperatures ($T_{180,g}$) against surface temperatures ($T_{-5,g}$) over the grass surface during both hot and cold seasons [[1] means the trend satisfied 5% significance level]

Next, the hourly mean empirical regression equations between three temperatures ($T_{180,g}$, $T_{20,g}$, $T_{-20,g}$) and the reference surface temperature ($T_{-5,g}$) over grass surface during both hot and cold seasons are summarized in Table 5.2. Due to a lack of the ambient temperatures above 0.2 m ($T_{20,g}$) in the first two months of the measurement, this empirical equation was not available. The findings show that a correlation is generally higher during the cold season and all equations were statistically significant.

Table 5.2 Statistical summary of empirical equations of hourly temperatures against a underground temperature 0.05 m below grass surfaces at TKL station during both hot and cold seasons

	$y^{(a)} = T_{-5,g}*A + B$							
	Hot season				Cold season			
	A	B	R^2	p-value	A	B	R^2	p-value
$T_{180,g}$	0.781	3.46	0.65	0.00	0.952	-1.56	0.82	0.00
$T_{20,g}$	0.895	0.602	0.62	0.00				
$T_{-20,g}$	0.572	12.4	0.61	0.00	0.552	9.86	0.72	0.00

(a) y *can represent* $T_{180,g}$, $T_{20,g}$ *and* $T_{-20,g}$

5.5.2 Concrete surfaces

Over concrete surfaces, there was no measurement of T_{-5}. The scattered diagram of mean daily ambient temperatures against the surface temperatures $T_{0,c}$ over the concrete surface is shown in Figure 5.13. A considerable good correlation (R^2 > 0.95) was found during the cold season. During the hot season, the correlation was relatively weak (0.49). It appears conceivable that empirical equations derived in this study are useful for the estimation of ambient temperatures from surface temperatures.

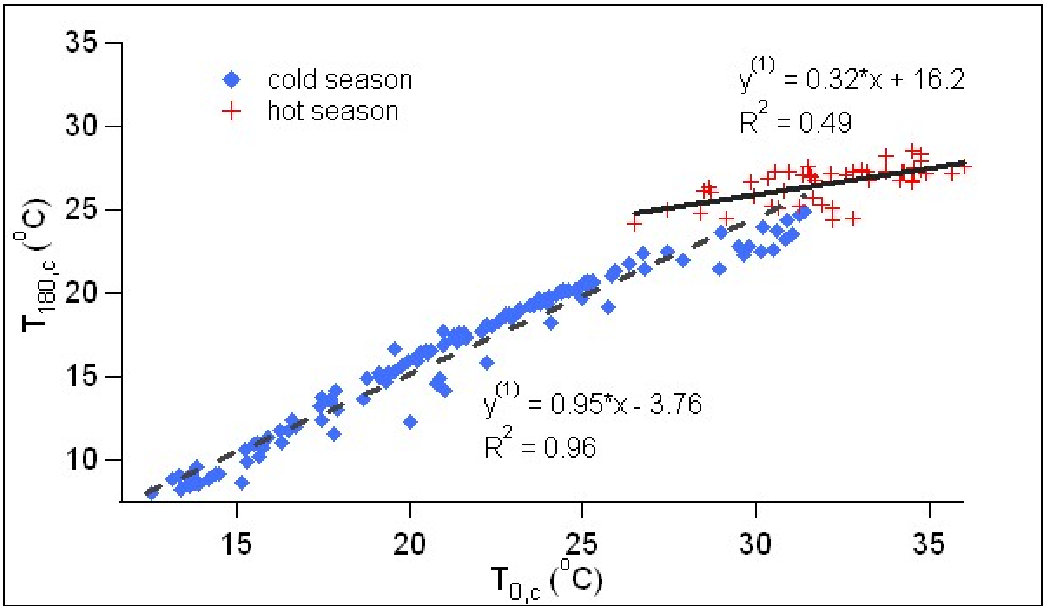

Figure 5.13 Scattered diagram of mean daily ambient temperatures ($T_{180,c}$) against surface temperatures ($T_{0,c}$) over the concrete surface during both hot and cold seasons [[1] means the trend satisfied 5% significance level]

Regarding hourly empirical equations over concrete surfaces, a summary of these equations between three temperatures ($T_{180,c}$, $T_{20,c}$, $T_{-15,c}$) and a reference soil surface temperature ($T_{0,c}$) over concrete surfaces during both hot and cold seasons is listed in Table 5.3. It was found that the correlations between the ambient temperatures ($T_{180,c}$ and $T_{20,c}$) and the reference surface temperature ($T_{0,c}$) was considered as good over the two seasons and these correlations were better during the cold season. However, the correlation between $T_{-15,c}$ and $T_{0,c}$ was significantly low. A weak statistical significant correlation could be found with soil temperatures below 0.2 m the surfaces. One of the possible explanations is that the heat capacity of soil is large and the rate of heat conduction in soil is much lower than that in air. Therefore, a good correlation between hourly soil temperatures could not be found.

Table 5.3 Statistical summary of empirical equations of hourly temperatures against a surface temperature $T_{-10,c}$ concrete surfaces at TKL station during both hot and cold seasons

	$y^{(a)} = T_{0,c} * A + B$							
	Hot season				Cold season			
	A	B	R^2	p-value	A	B	R^2	p-value
$T_{180,c}$	0.453	11.9	0.79	0.00	0.873	-2.21	0.93	0.00
$T_{20,c}$	0.458	12.5	0.82	0.00	0.845	-0.381	0.94	0.00
$T_{-15,c}$	0.301	22.7	0.36	0.00	0.618	8.78	0.61	0.00

[(a)] y *can represent* $T_{180,c}$, $T_{20,c}$ *and* $T_{-15,c}$

The contribution of this section is the production of empirical equations relating ambient air temperatures / underground temperatures and surface temperatures over grass and concrete surfaces. These equations should be useful to the interpretation of the surface heat island and 1-D heat budget model.

5.6 Chapter summary

This chapter firstly discussed the "accuracy" of the satellite-derived surface temperatures by comparing with the results of the field measurement and the remote sensing images. Higher "accuracy" of data (about 3°C) was found in nighttime images. Secondly, the correlation between surface temperatures and ambient air temperatures was examined. Finally, more than 16 linear empirical equations for estimating ambient air temperatures from surface and underground temperatures were produced.

Chapter 6 : Time series analysis of heat island in Hong Kong

6.0 Outline

This chapter covers the heat island results from a long-term time series analysis and its interpretation. In section 6.1, a representative urban station and a representative suburban station were selected based on the preliminarily temperature analysis and the environment of six HKO stations. Section 6.2 outlines the properties and characteristics of heat island intensities obtained from the two representative stations. The diurnal and seasonal variations of this intensity were explored using 19-year temperature data (1989 – 2007). Section 6.3 describes the long term trends of heat island intensity. Section 6.4 discusses the influence of relative humidity and population growth on the properties of heat island intensity and its trends. The correlation between the trend of heat island and the temperature trend due to urbanization is discussed in section 6.5. The key findings of this chapter are summarized in section 6.6.

6.1 Selection of stations

This section presents the criteria of selecting one representative urban station and reference station among six HKO stations by considering the temperature properties in these stations. Two of six HKO stations are located in the center of Hong Kong and other four stations are located at coastal areas away from the city center. Two selected urban stations are HKO Headquarters (HKOH) station and King's Park (KP), three suburban stations are Ta Kwu Ling (TKL) station, Lau Fu Shan (LFS) station, Cheung Chau (CCH) station and one rural station is Waglan Island (WGL) station. Section 6.1.1 describes the selection of a representative urban station from two HKO stations in detail, which are located in the Kowloon Peninsula. Section 6.1.2 outlines the results of the heat island intensities between the representative urban station and four suburban stations from the period of 1994 – 2004. A reference station was selected among them based on these results.

6.1.1 Urban station

A 11-year temperature profile at six HKO stations were analyzed and the temperature trends of monthly means are depicted in Figure 6.1 for 11 years (1994 – 2004). The red line in Figure 6.1 is the temperature observed at HKOH station and the blue line is KP station's. The hollow blue circles, the hollow green squares, the solid red circles and the solid purple squares represent the TKL, LFS, CCH and WGL suburban stations respectively. In general, the monthly air temperature at HKOH was the highest throughout the year among all HKO stations.

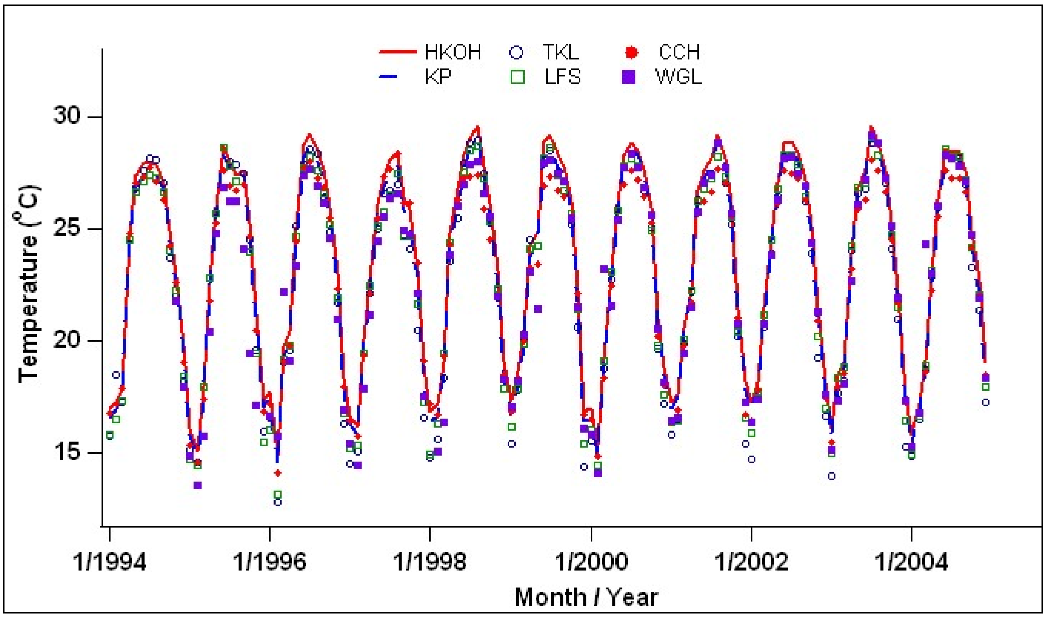

Figure 6.1 Monthly mean temperature observed in six HKO stations (1994 – 2004)

Regarding the two HKO urban stations, both stations (HKOH and KP) are located in the center of Kowloon Peninsula and they are 1.1 km apart. A summary of the average temperature at the two urban stations is listed in Table 6.1. The monthly average temperature at the HKOH was slightly higher than that at the KP. However, the ranges of monthly average, minimum and maximum temperatures at the KP were larger. From the statistical point of view, there was no significant evidence to support any difference in their monthly average, minimum and maximum temperatures between two urban stations.

Therefore, the meteorological data at these two stations can be assumed to be similar and the temperature readings can represent the urban temperatures with similar microclimate characteristics.

Table 6.1 Summary of monthly temperatures at two urban HKO stations (1994 – 2004)

	HKOH			*KP*		
	Mean	Min.	Max.	Mean	Min.	Max.
Monthly average temperature	23.4	14.6	29.6	23.1	14.4	29.2
Monthly minimum temperature	21.7	12.7	27.8	21.1	11.9	27.2
Monthly maximum temperature	25.6	16.9	32.5	25.8	16.9	32.1

Based on the temperature readings at two stations, the urban characteristics of two stations are similar. The surrounding views of two stations are shown in Figure 6.2. HKOH headquarters station is surrounded by many high-rise buildings while the KP station is located on the top of a small hill and has a much wider sky view. The temperatures measured at the HKO headquarters station are likely affected by surrounding high-rise buildings much more than those of KP station and HKOH is typical of urban environment. As a result, the HKOH station was selected as a representative urban station in this study for the following time series analysis in sections 6.2 to 6.5.

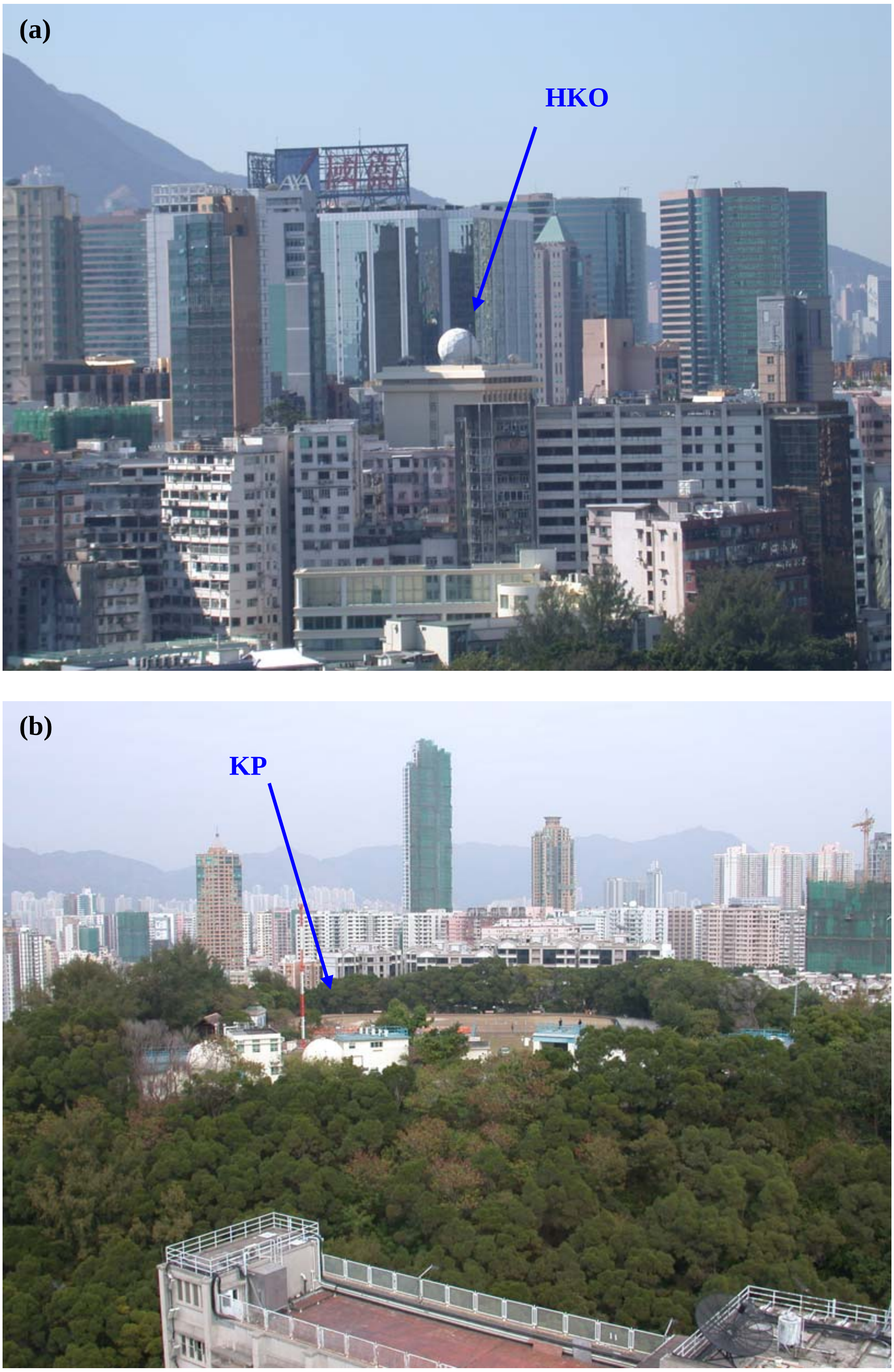

Figure 6.2 Surroundings of two HKO stations (a) HKO headquarters station and (b) King Park's station

6.1.2 Selection of reference station

Four HKO stations were shortlisted out of 27 meteorological stations for selecting a reference station. They were Cheung Chau (CCH), Waglan Island (WGL), Lau Fau Shan (LFS) and Ta Kwu Ling (TKL). CCH and WGL are classified as coastal suburban areas; and LFS and TKL are classified as inland suburban areas. The microclimates of these four stations are slightly different. A study was carried out to examine which station is most representative of rural environment among these four stations. The difference between the temperature measured at HKOH and the temperature measured at a suburban station was studied. There are four possible combinations, namely HKOH-CCH, HKOH-WGL, HKOH-LFS and HKOH-TKL. The term "HKOH-TKL" represents a temperature difference between the HKOH urban station and the Ta Kwu Ling suburban station. Annual and monthly heat island intensities were computed by averaging daily value, which was the maximum of hourly temperature difference between two stations.

<u>Trend Analysis among four station pairs</u>

Figure 6.3 shows annual heat island intensities between the urban station (HKOH) and the four HKO stations (CCH, LFS, TKL and WGL). HKO-CCH and HKO-TKL had an increasing trend at 5% significance level in the past 11 years. HKO-WGL had slightly decreased in the past 9 years at 5% significance level and HKO-LFS had a weak decreasing trend. No consistent observation can be drawn from the annual trend analysis. Therefore, the seasonal analysis was conducted to explore a UHII trend.

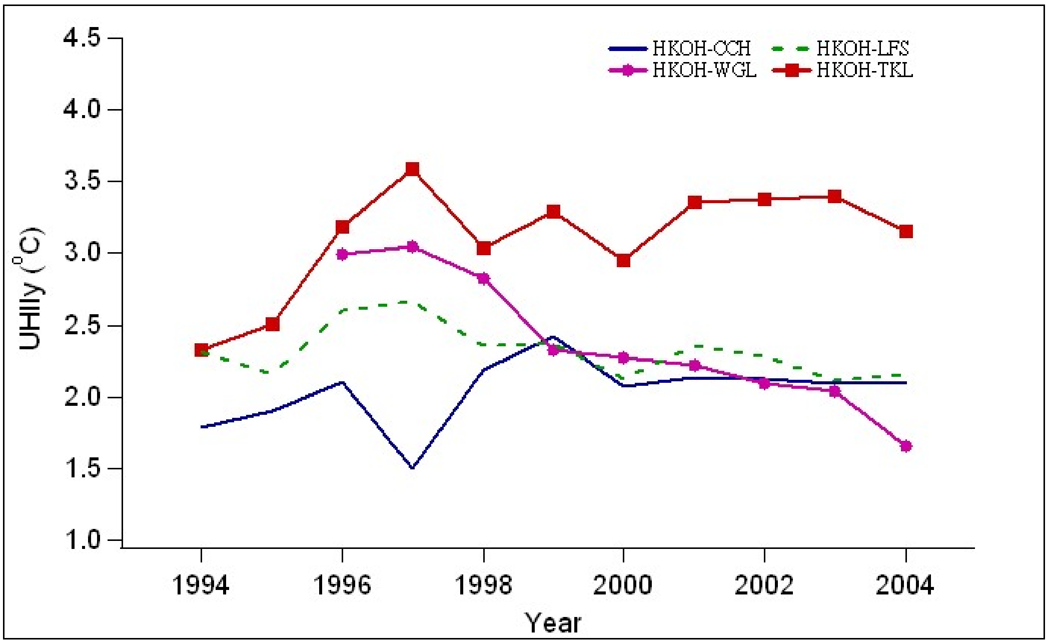

Figure 6.3 Annual trends of daily maximum UHII (UHIIy) between HKOH station and four suburban stations

The long-term trend was further study by looking at individual season. In the Northern Hemisphere, the spring season starts from March to May; summer between June and August; autumn between September and November; and winter between December and February. Seasonal heat island intensities were computed by averaging the daily maximum UHII in the specific three months. The results are similar to those shown in Figure 6.3. The findings show that an increasing trend between CCH / TKL stations and the urban station was found in each season while a decreasing trend between WGL station and the urban station was obtained in four seasons. The seasonal trends between LFS station and the urban station were not clear in spring and summer but there were a decreasing trends in fall and winter. Based on the results of annual and seasonal trend analysis, local microclimates certainly affect the temperature readings at the local areas and this causes different UHII results between the urban station and the suburban stations.

Diurnal variation study

To select the extreme case of heat island intensity in Hong Kong, a diurnal variation of these intensities among the four stations pairs was investigated to select the most representative suburban station. The mean of hourly UHII ($UHII_h$) was calculated by averaging hourly temperature difference between urban and suburban stations for 11 years. As shown in Figure 6.4, an upside down bell shape of heat island intensities were depicted for all four station pairs but the magnitudes of the intensities varied for different station pairs. In general, the maximum heat island intensity usually occurs at night and the minimum UHII usually occurs during the daytime. Due to the marine effect on coastal suburban station, the peak intensities have been shifted to occur after the sunset but before mid-night. The diurnal variations of heat island intensity were 2.0^{o}C, 2.3^{o}C, 1.8^{o}C and 3.4^{o}C for HKOH-CCH, HKOH-WGL, HKOH-LFS and HKOH-TKL accordingly. The highest intensity and largest diurnal variation were measured between the TKL station and the urban HKOH station.

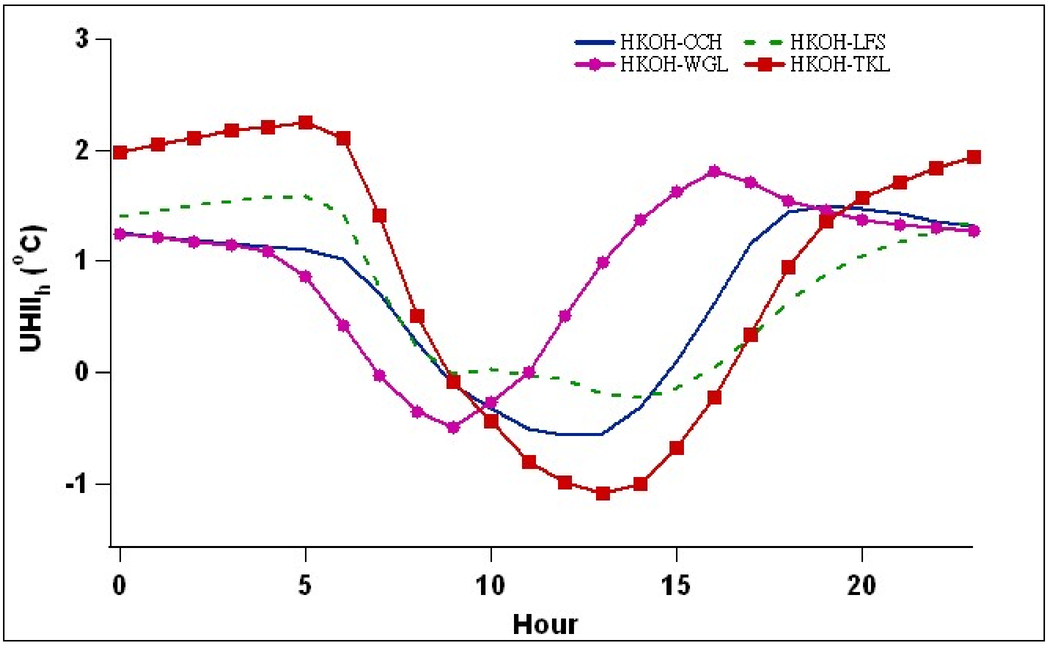

Figure 6.4 Mean of hourly UHII ($UHII_h$) between HKOH headquarters station and four suburban stations

In short, the diurnal profiles of the four stations pairs are similar but there are subtle differences in different station pairs. The findings of the trend analysis and the diurnal variation study may indicate that selecting a reference station is extremely important to interpret heat island intensity. In this study, Ta Kwu Ling (TKL) station was selected as a reference station with reasons. First, the result of the diurnal heat island intensity study reported that the highest intensity was found between TKL station and the urban station. It is worth investigating the highest heat island intensity and its impact in Hong Kong. Second, the marine effect at TKL area is minimized by the surrounding high hills. Third, nearly 95% of land cover is grass at the TKL area with low population. Human heat impact can be effectively reduced. Although WGL station is classified as rural based on the criteria list in Table 3.5, this station was not selected as the reference station due to a large marine effect on diurnal temperature variation.

6.2 General features of heat island intensity

Based on the results in section 6.1, HKOH station was selected as the urban reference station and TKL station was selected as the reference station respectively for further time series analysis. The properties and characteristics of the heat island intensity in Hong Kong in a period of 1989 – 2007 were analyzed. This section reports the heat island intensity measured from two stations and describes the results of diurnal and seasonal heat island intensity.

6.2.1 Summary of heat island intensity

The frequency distribution of the daily maximum heat island intensity ($UHII_{max}$) in four seasons is shown in Figure 6.5. There were a total of 6879 samples for 19 years. The average of $UHII_{max}$ was 2.7^{o}C and the range was between -1.9^{o}C and 11.5^{o}C in this subtropical city. The maximum of $UHII_{max}$ of 11.5^{o}C occurred in winter. In addition, the $UHII_{max}$ distribution in each season was different. The mean of the $UHII_{max}$ was about 2.2^{o}C ± 2.6^{o}C in spring, was 2.6^{o}C ± 2.1^{o}C in summer, was 3.4^{o}C ± 3.6^{o}C in fall and was 3.9^{o}C ± 4.6^{o}C in winter respectively. For the groups above 5.0^{o}C, over 45% of the $UHII_{max}$ were recorded in winter. These mean values of $UHII_{max}$ were statistically different among four seasons. The results supported that the properties of the heat island intensity possibly vary seasonally, which are discussed in section 6.2.3. This result was also consistent with other studies' that the maximum UHII occurs in the cold seasons (Hinkel et al. 2003; Hawkins et al. 2004).

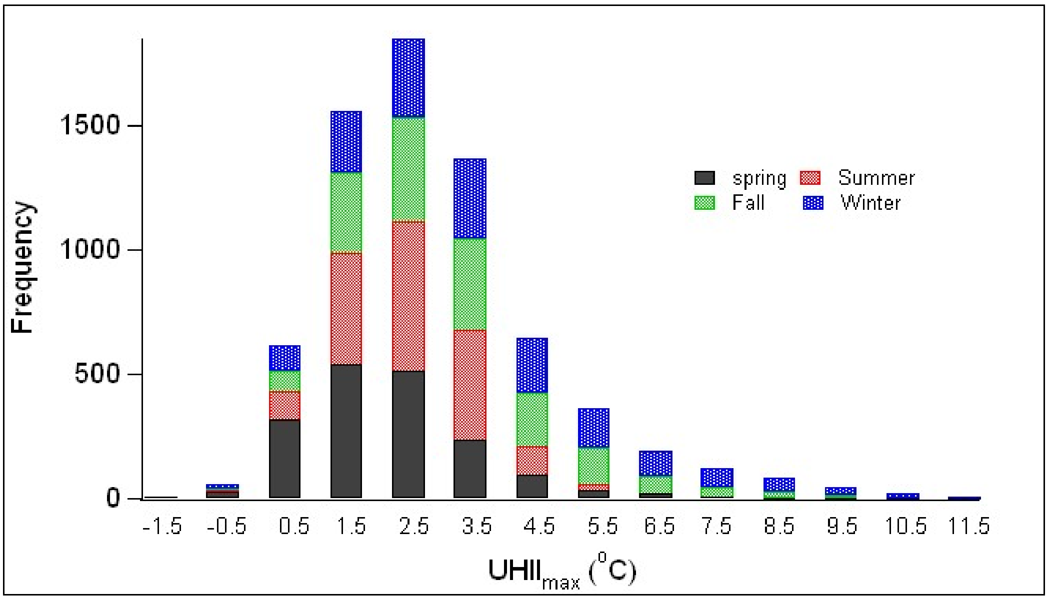

Figure 6.5 Frequency distribution of daily maximum heat island intensity $UHII_{max}$ between the urban and suburban stations for 19 years (Class range example: Class 1 ranged from 1.5 to 2.4)

6.2.2 Diurnal variation

Figure 6.6 shows the average hourly heat island intensity (UHII) between the urban station (HKOH) and the suburban station (TKL) on both diurnal and monthly basis based on 19 years data. On a diurnal basis, the maximum (positive) UHII often happened before the sunrise (4:00–6:00) while the minimum (negative) UHII happened during the daytime (13:00–15:00). In other words, this effect occurred 7-9 hours after the sunset. Typically, heat island effects occur 3-4 hours after the sunset (Oke 1989). It could be due to city geometry that can affect the occurrence time of maximum heat island intensity on one day. On the other hand, there exists a negative heat island intensity which frequently occurs during the daytime. Such negative differences indicate that the temperatures at the suburban stations are higher than that in the urban station during the daytime (22:00 – 5:00). This phenomenon of this negative heat island intensity is called "Cool Island Effect", which is mentioned in section 2.1. In Hong Kong a recent study also reported that the cool island effect occurs during the daytime in clear sky days using different temperature pairs (Memon et al. 2009). However, limited research has discussed the cool island effect because the negative impact of cool island effect may not be as severe as heat island effect. Therefore, the conclusion is that both heat and cool island effects exist between HKOH–TKL station pair. As higher temperature will cause health problem, affect our air quality and consume much more electricity energy (Fung et al. 2006; Parry et al. 2007), only the maximum UHII at dawn is discussed in the following sections.

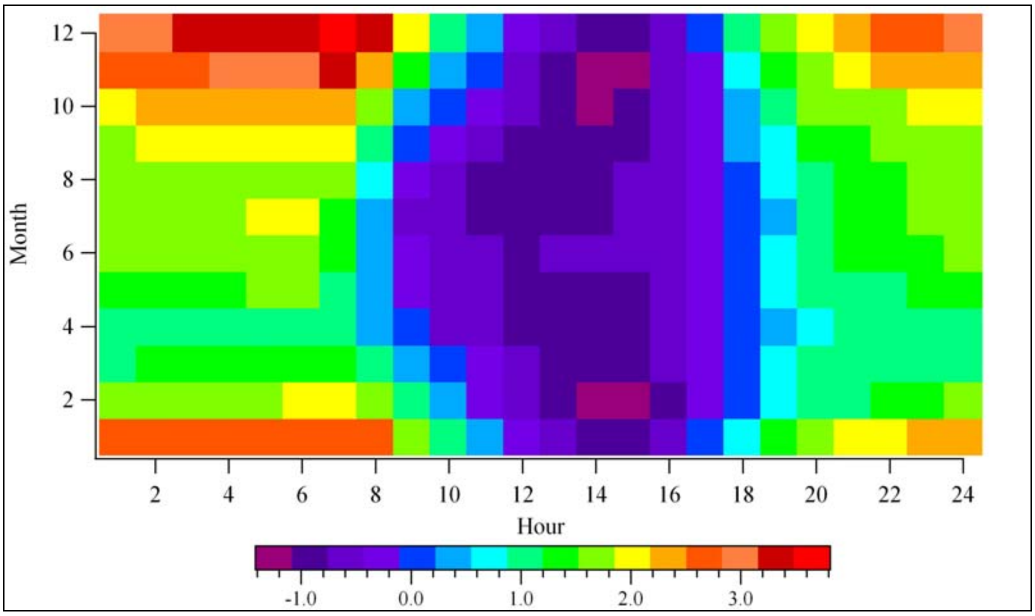

Figure 6.6 Temporal distribution of UHII between the urban and suburban stations for 19 years

6.2.3 Seasonal variation

As shown in Figure 6.6, the maximum monthly means of the heat island intensity were always observed during the cold seasons and the mean of these values could reach 3.8^{o}C. The maximum values of UHII were relatively low during spring and they generally increased every month and reached the highest value in December. However, most studies focus on the impact of heat island effect in summer (hot season) in the north the Northern Hemisphere, but not the highest value of heat island intensity (Rosenzweig et al. 2005). One of the possible reasons is that the temperature impact on humans during the hot season is much more significant than that during the cold season.

Cloud amount is one of the possible factors that could reduce the average heat island intensity. Figure 6.7 shows the monthly variation of $UHII_m$ between the HKOH station and TKL station with two standard derivations (±2σ interval) and the corresponding average monthly cloud amount at King's Park KP station. The ±2σ interval of the monthly data was marked with upper and lower caps by taking two standard derivations of the data set. In Hong Kong, monthly cloud amount in winter was about 62%, which was much less than the amount of 78% in spring. It appears that the monthly mean of $UHII_m$ was inversely correlated to the monthly cloud amount. Heat island intensity decreases with cloud amount. On cloudy days, solar radiation is blocked by clouds during daytime and the natural heat source is more or less the same in both urban and suburban areas. Anthropogenic heat in urban area dominates the heat source but the impact of such heat was not so significant. Therefore, the heat island effect between two stations is not obvious in cloudy days. Furthermore, the variation of UHII in winter was possibly larger than that in spring in Hong Kong. Two standard derivation of the $UHII_m$ in winter was 1.8°C, which was 1.5 times of that in spring (1.2°C). This may also be attributed to the cloud amount. One likely explanation is that overcast days can maintain a uniform weather condition over a large areas and heat balance among these areas is likely similar. As such, both the variation and magnitude of the UHII between two stations were reduced in cloudy seasons.

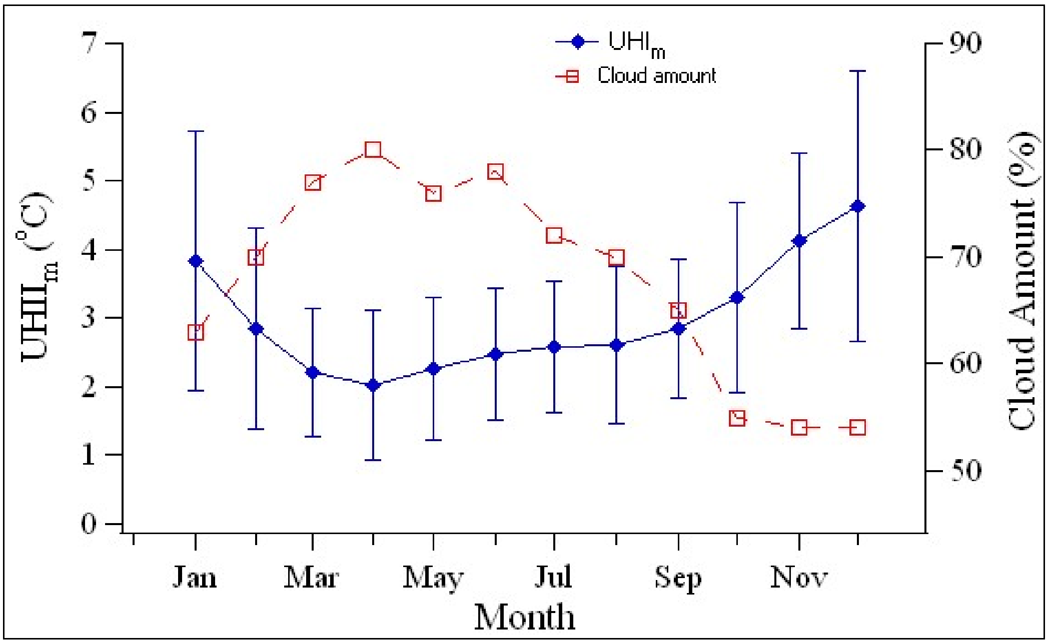

Figure 6.7 Monthly mean of the daily maximum heat island intensity (UHII$_m$) between HKOH station and TKL station, and monthly cloud amount at KP station for 1989-2007 [Vertical bars represent 2 standard deviations of the UHII$_m$]

6.3 Trend analysis

6.3.1 Seasonal trend

The graphical results of seasonal trends are shown in Figure 6.8 and the statistic results are tabulated in Table 6.2 accordingly. The same patterns of an increasing trend in four seasons were found but the magnitudes of the trends were different. The UHII$_m$ increased 0.47°C per decade in spring, 0.24°C in summer, 0.09°C per decade in fall and 0.38°C per decade in winter.

The seasonal trend of UHII$_m$ was then studied against the cloud amount. As shown in Table 6.2, increasing trends of seasonal heat island intensity in spring, summer and winter were found. At the same time, a decreasing trend of cloud amount was observed in the corresponding seasons. These results allow us to generalize that an overcast weather can weaken the formation of large temperature difference between urban and suburban areas, and a decreasing trend of cloud amount is likely associated with an increasing trend of seasonal UHII.

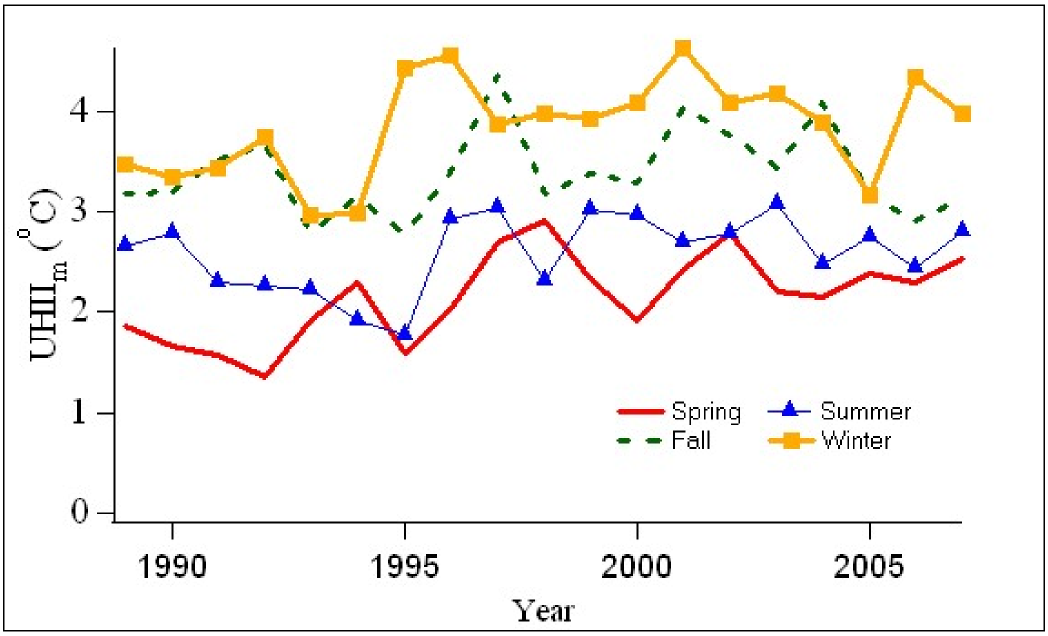

Figure 6.8 Seasonal trends of the monthly heat island intensity $UHII_m$ from 1989 to 2007

Table 6.2 Seasonal trends of monthly UHII and monthly cloud amount from 1989 to 2007

	Spring	Summer	Fall	Winter
$UHII_m$ (^oC/decade)	0.47	0.24	0.09	0.38
R^2	0.38	0.13	0.02	0.18
p value	0.01	0.14	0.63	0.07
Cloud amount (%/decade)	-0.79	-0.33	4.24	-1.47

6.3.2 Annual trend

Annual UHII intensities were calculated by averaging daily maximum intensity between two stations (HKOH and TKL) for each year. Figure 6.9 shows the annual intensity ($UHII_y$) along a time series (1989 – 2007) and the annual trend was computed linear regression. The $UHII_y$ trend from this 19-year observation was 0.29^oC/decade. The slope was statistically significant. The increasing $UHII_y$ trend could be due to urbanization and/or climate change.

Kalnay and Cai (2003) have introduced a "observation minus reanalysis" (OMR) difference method to estimate the impact of land-use/urbanization changes on temperature trend. In this study, the mean temperature trend at the urban (HKOH) station was found to be 0.30^oC/decade for 19 years (1989-2007) and the mean temperature trend of the NCEP/NCAR (NNR) reanalysis in the grid containing Hong Kong is -0.03^oC/decade for the same period (http://dss.ucar.edu/datasets/). By applying the OMR method, the annual mean temperature trend due to urbanization was estimated to be 0.33^oC/decade, which is slightly higher than the annual UHII trend result of this study (0.29^oC/decade). One possible reason may be that the population in the neighborhood of HKOH has been growing significantly since 1989. More and more residents have migrated to urban areas. An increase in energy demand and heat emission in urban areas may cause higher temperature readings in the urbanized areas. The temperature trend in urban areas has been increasing significantly while the temperature trend in less developed areas (suburban / rural areas) has been changing slowly. A subtle increase in annual temperature in the reference TKL station was then obtained. Thus, the magnitude of UHII trend is relatively smaller.

In addition, Lim et al. (2005) applied the OMR method to different land uses and they reported that an average temperature trend of 0.20^oC/decade was recorded in urban areas. By applying this OMR analysis method to the other Asian cities (Shanghai, Beijing, Singapore and Tokyo), a similar result was obtained. The urbanization trends in these cities ranged 0.27-0.53^oC/decade. The trend in Singapore of 0.27^oC/decade was closer to that in Hong Kong as similar high population density development policy in these two cities. The result of the estimated temperature trend of 0.27^oC/decade was similar to the result of this study (0.29^oC/decade).

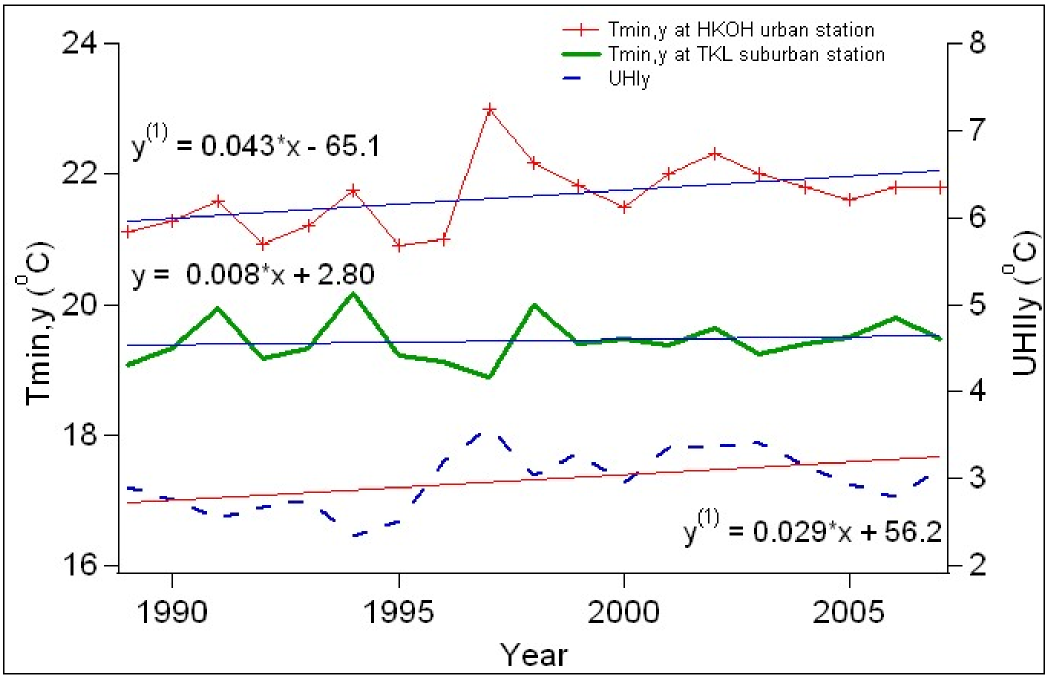

Figure 6.9 Annual trends of mean minimum daily temperatures at both urban and suburban stations $T_{min,y}$ (right axis), and annual mean of UHII between two stations UHIIy (left axis) for a period of 1989 – 2007 [(1) means the trend satisfied 5% significance level]

6.4 Factors affecting heat island intensities

It is interesting to investigate which meteorological and / or non-meteorological variables have correlation with the annual UHII. Ten meteorological variables and two non-meteorological variables were used to examine whether they are related to heat island intensity. The ten meteorological variables were the mean of daily maximum temperature, the mean of daily mean temperature and minimum temperature and relative humidity at the HKOH station, the mean of daily minimum temperature, relative humidity and wind speed at the TKL station, wind speed, cloud amount and daily global radiation at the KP station. Two other non-meteorological variables were population and energy consumption. Normalization of each variable was performed and Table 6.3 summarizes the correlations of the annual heat island intensity against 12 variables. It was found that most variables were positively correlated to the annual UHII, except relative humidity reading at the HKOH station and, cloud amount and wind speed at the KP station and wind speed at the TKL station. The highest correlation coefficient (r) was 0.74 and the corresponding variable was the mean of daily minimum temperature at the HKOH station. The highest negative correlation coefficient was associated with annual mean value of wind speed at the urban station and the r was -0.46. The second highest negative correlated variable was the wind speed at the suburban station with r of -0.29, which was less than that of the highest correlated variable. There is an observation that both wind speeds measured at urban and suburban stations are negatively correlated to heat island intensity, but such correlation was higher at urban station.

Table 6.3 Correlation coefficients among annual means of UHII, 10 meteorological variables and 2 non-meteorological variables [HKOH represents the meteorological data measured at HKOH station; TKL represents the meteorological data measured at TKL station; KP represents the meteorological data measured at KP station]

		Meteorological variables										*Non-meteorological variables*	
		HKOH				*TKL*			*KP*				
	$UHII_y$	$T_{max,y}$	$T_{mean,y}$	$T_{min,y}$	*RH*	T_{min}	*RH*	*WS*	WS	*Cloud*	*global radiation*	*Population ('000)*	*Energy*
$UHII_y$	1.00												
$T_{max,y,HKOH}$	0.35	1.00											
$T_{mean,y,HKOH}$	0.52	0.60	1.00										
$T_{min,y,HKOH}$	0.74	0.55	0.77	1.00									
RH_{HKOH}	-0.16	0.10	-0.09	0.08	1.00								
$T_{min,y,TKL}$	0.17	-0.14	-0.12	0.08	-0.29	1.00							
RH_{TKL}	0.20	0.07	0.25	0.45	0.60	-0.28	1.00						
WS_{TKL}	-0.29	-0.28	0.30	-0.33	-0.02	-0.12	-0.12	1.00					
WS_{KP}	-0.46	-0.66	-0.18	-0.71	-0.30	-0.30	-0.18	0.82	1.00				
$Cloud_{KP}$	-0.04	0.11	0.20	0.18	0.51	-0.30	0.61	0.36	0.19	1.00			
Global radiation, $_{KP}$	0.11	0.15	0.16	0.21	-0.46	0.21	-0.34	-0.45	-0.25	-0.56	1.00		
Population ('000)	0.59	0.24	0.56	0.68	-0.06	0.12	0.42	-0.49	-0.78	0.19	0.23	1.00	
Energy (TJ)	0.42	0.25	0.42	0.58	0.06	0.19	0.36	-0.53	-0.77	0.09	0.28	0.93	1.00

$UHII_y$ – annual mean of daily maximum UHII; $T_{max,y,HKOH}$ – Annual mean of daily maximum temperature measured at HKOH, $T_{mean,y,HKOH}$ - Annual mean of daily mean temperature measured at HKOH; $T_{min,y,HKOH}$ - Annual mean of daily minimum temperature measured at HKOH; $RH,_{HKOH}$ – Annual mean of daily mean relative humidity measured at HKOH; $T_{min,y,TKL}$ - Annual mean of daily minimum temperature measured at TKL; $RH,_{TKL}$ - Annual mean of daily mean relative humidity measured at TKL; $WS,_{TKL}$ - Annual mean of hourly wind speed measured at HKOH; $WS,_{KP}$ - Annual mean of hourly wind speed measured at KP; $Cloud,_{KP}$ – Annual mean of cloud amount measured at KP; Global radiation,$_{KP}$ – Annual mean of daily global radiation measured at KP

In addition, a multiple regression analysis was preformed with five variables with relatively high correlations obtained in Table 6.3. They were the daily mean and minimum temperatures measured at the HKOH station, wind speed measured at the KP station, population and energy consumption. The multiple regression equation is shown in Equation (6.1) and the statistical results of this equation are shown in Table 6.4. The overall p-value of the equation was 0.13 and the R^2 is relatively high of 0.69. For individual variables, the p-value of both wind speed and energy consumption were statistically significant but other variables were not. Even the p-value of energy consumption variable was less than 0.1, the coefficient value of energy consumption variables was considerably zero. This finding implies that the effect of energy consumption variable on the annual heat island intensity could be neglected. In addition, the coefficient value of population variable is also small. From the statistical point of view, the correlation between annual UHII and non-meteorological variables is weak and annual UHII is likely correlated to meteorological factors only, especially wind speed and the minimum temperature at urban station. These two variables are commonly used to simulate the heat island intensities in many cities. The wind speed at urban station may be the key variables, which is negatively correlated to heat island intensities. This result supports the findings from other studies that higher heat island intensity was usually obtained in a weather with low wind speed (Oke 1981).

$$UHII_y = 1.09 + 0.50*T_{mean,y,HKOH} - 0.68*T_{min,y,HKOH} - 1.45*WS_{,KP} + 0.002*Pop - 0.00004*E \quad (6.1)$$

where UHIIy is an annual mean of UHII in ^oC

$T_{mean,y,HKOH}$ is the mean of daily mean temperature at HKOH in ^oC

$T_{min,y,HKO}$ is the annual mean of daily minimum temperature at HKOH in ^oC

WS_{KP} is an average wind speed at KP in ms^{-1}

Pop is an annual population in thousand persons

E is an annual electricity consumption in TJ

Table 6.4 Statistical output of the multiple regression equation for annual UHII against 3 meteorological variables and 2 non-meteorological variables

Regression Statistics	
Correlation, r	0.83
Coefficient of determination, R^2	0.69
Standard Error, ε	0.17
Overall Significance, P -value	0.13

	Coefficients	*Standard Error*	*t Stat*	*P-value*
Intercept	1.09	9.49	0.12	0.91
$T_{mean,y,HKOH}$	0.50	0.37	1.38	0.22
$T_{min,y,HKOH}$	-0.68	0.46	-1.46	0.19
$WS_{,KP}$	-1.45	0.57	-2.55	0.04
Pop	0.00216	0.00	1.21	0.27
E	-0.00004	0.00	-2.17	0.07

6.5 Chapter summary

This chapter focuses on the analysis of heat island intensity using fixed station's data record. The work firstly search among six HKO meteorological stations for the most representative urban and suburban site using long-term time series analysis. Based on temperature records and landscape, the Hong Kong Observatory Headquarters at Tsim Sha Tsui was selected as a urban reference station and Ta Kwu Ling station was selected as a reference station.

Secondly, spatial variations of heat island intensity were analyzed in a period of 1989 – 2007. The fixed station data analysis yielded a heat island intensity of around 2.7^{o}C with a range from -1.9^{o}C to 11.5^{o}C. Maximum hourly heat island intensities often happen before the sunrise (4:00 – 6:00) while minimum (negative) intensities happen during the daytime (13:00 – 15:00). Regarding a trend analysis, there had been an increasing trend of 0.29^{o}C/decade in the annual heat island intensity and the seasonal trend was 0.47^{o}C/decade in spring and was 0.09^{o}C/decade in fall. This result was consistent with a number of studies in the literature.

Lastly, the relationship between meteorological and non-meteorological parameters and annual UHII was discussed. Five selected variables were used to corroborate the UHII. The findings supported that wind speed at urban station contributes to the formation of heat island.

Chapter 7 : Surface heat budget analysis

7.0 Outline

This chapter describes a 1-year field experiment of surface heat budget carried out at Ta Kwu Ling site. In order to understand the formation of maximum urban heat island intensity, four energy components including sensible heat, latent heat, solar radiation and soil heat were measured. Seasonal and diurnal analyses of four energy components are outlined in section 7.1. The impacts of the land surface changing from grass surface to concrete surface are outlined in section 7.2. The impact parameters include heat budget terms and two physical parameters (albedo and emissivity). A critical discussion in the use of the measured albdeo and emissivity in modelling is also discussed. The key findings of heat budget measurement are concluded in section 7.3.

7.1 Heat budget measurement

<u>Measurement description</u>

A 1-year intensive heat budget measurement was conducted at Ta Kwu Ling from 2 March 2007 to 28 February 2008. The measurement was first set up over grass surface and later moved to a concrete surface since 17 August 2007. The heat flux measurement over each surface covers both summer and winter. The measured heat flux densities include solar radiation, subsurface soil heat, sensible heat and latent heat. Diurnal and seasonal variations of heat fluxes are analyzed.

7.1.1 Solar radiation

Net radiation was measured at Ta Kwu Ling. Specifications of the net radiometer has been given in chapter 3. This section outlines both seasonal and diurnal patterns of the four radiation components, viz Qs,sky, QL,sky, Qs,gd and QL,gd and net radiation Q*.

<u>A comparison of monthly global solar radiation at King's Park and Ta Kwu Ling</u>

In this study, the monthly mean of daily global solar radiation measured at Ta Kwu Ling was compared to that measured at King's Park in order to assess the quality of the Ta Kwu Ling data. The Hong Kong Observatory started monitoring daily global solar radiation in Hong Kong in 1958 (Sham 1964). At present, global solar radiation are measured at King's Park by a thermoelectric pyranometer together with an integrating counter. Figure 7.1 shows the monthly mean of daily global solar radiation at King's Park ($Q_{S,KP}$) against that at Ta Kwu Ling ($Q_{S,TKL}$) from March 2007 to February 2008. The correlation between the two observations was very high (R^2 = 0.94) and the p-value of this regression was less than 1.5E-0.7. Linear regression equation indicates that the value at King's Park was slightly higher but the difference in daily global solar radiation was not statistically significant. The quality of the daily global solar radiation readings taken at Ta Kwu Ling are consider satisfactory.

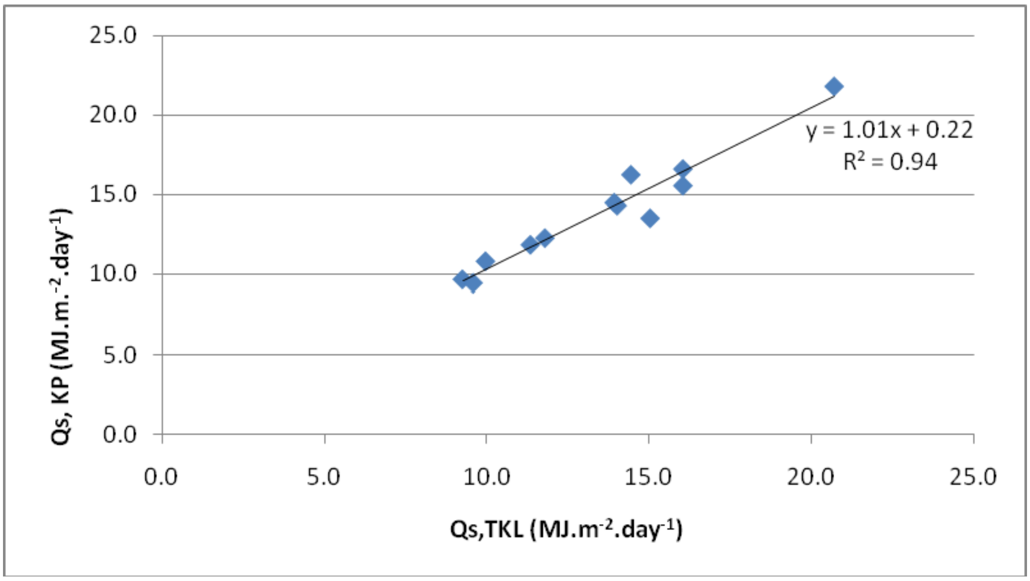

Figure 7.1 Scattered diagram of monthly mean of daily global solar radiation at King's Park ($Q_{S,KP}$) against that at Ta Kwu Ling ($Q_{S,TKL}$) (March 2007 to February 2008*). The linear regression line is overlaid

**Only 19 daily global solar radiation data at Ta Kwu Ling was available in August 2007 as measurement was discontinued in 6-16 August 2007 due to relocation of the instruments from grass surface to concrete surface; over 80% data available in other months.*

<u>Seasonal variations of global solar radiation from the sky (Qs, sky)</u>

As shown in Figure 7.2, the monthly mean of daily global solar radiation (mean of 24 hours average) from the sky (dotted line) varies from 9.26 $MJm^{-2}day^{-1}$ (107 Wm^{-2}) in March 2007 to 20.71 $MJm^{-2}day^{-1}$ (40 Wm^{-2}) in July 2007 were recorded. It should be noted that the hourly global solar radiation becomes zero from 20:00 to 5:00 in the following day. In general, global solar radiation was higher in summer and lower in winter. The result was generally consistent with Lam and Li (1996), which reported that the monthly mean daily global solar radiation varying from 8.50 $MJm^{-2}day^{-1}$ (98 Wm^{-2}) in March to 18.40 $MJm^{-2}day^{-1}$ (213 Wm^{-2}) in July in urban area of Hong Kong between 1991 and 1993.

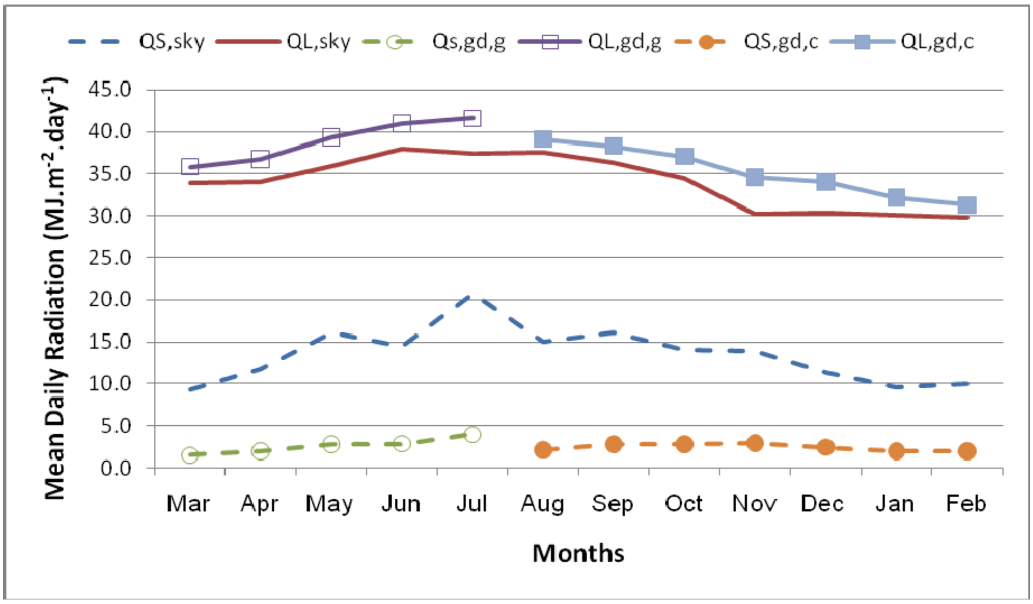

Figure 7.2 Monthly mean of daily global solar radiation from the sky (Qs,sky), global solar radiation reflected from the grass surface (Qs,gd,g), the concrete surface (Qs,gd,c), infrared radiation from the sky (Q_L,sky), infrared radiation reflected from the grass surface (Q_L,gd,g) and the concrete surface (Q_L,gd,c) at Ta Kwu Ling (Grass surface: March – July 2007; Concrete surface: August 2007 – February 2008)

A seasonal variation of global solar radiation reflected from the ground (Qs,gd) was then examined. The monthly mean of daily global solar radiation (Qs,gd) reflected from the ground surface is also shown in Figure 7.2. The curve of Qs,gd is separated into two parts due to a change of measurement location and land surface in August 2007. The first part from March to July 2007 represents the radiation characteristic over the grass surface. The second part from August 2007 to February 2008 showed the radiation variation over the concrete surface. The findings show that the monthly mean of daily global solar radiation reflected from the grass surface (green dotted line with hollow circle marks) ranged from

1.52 $MJm^{-2}day^{-1}$ (18 Wm^{-2}) in March to 3.97 $MJm^{-2}day^{-1}$ (46 Wm^{-2}) in July and the associated range over the concrete surface (orange dotted line with solid circle marks) was between 1.98 $MJm^{-2}day^{-1}$ (23 Wm^{-2}) in February 2008 and 2.92 $MJm^{-2}day^{-1}$ (34 Wm^{-2}) in November 2007. A seasonal difference in global solar radiation reflectance over the two different surfaces was not significant as the figures are small in comparison to the infrared radiation.

Seasonal variations of infrared radiation (Q_L,sky, Q_L,gd)

The seasonal variations of monthly mean infrared radiation from the sky and infrared radiation emitted by the ground surface are shown in Figure 7.2. The sky infrared radiation (red solid line) was between 29.89 $MJm^{-2}day^{-1}$ (346 Wm^{-2}) (in February 2008) and 37.95 $MJm^{-2}day^{-1}$ (439 Wm^{-2}) (in June 2007). The infrared radiation emitted from the grass surface Q_L,gd,g (purple solid line with hollow square marks) increased from 35.86 $MJm^{-2}day^{-1}$ (415 Wm^{-2}) (in March 2007) to 41.60 $MJm^{-2}day^{-1}$ (481 Wm^{-2}) (in July 2007). The corresponding radiation over the concrete surface Q_L,gd,c (blue solid line with solid square marks) also increased from 31.28 $MJm^{-2}day^{-1}$ (362 Wm^{-2}) (in February 2008) to 39.29 $MJm^{-2}day^{-1}$ (455 Wm^{-2}) (in August 2007). There was a distinct seasonal variation pattern of infrared radiation. Both the sky infrared radiation and ground emitted infrared radiation are higher in summer and lower in winter. In addition, the infrared radiation emitted from the concrete surface was generally lower than that from the grass surface. This indicates that land surface change does affect the emission of infrared radiation. Since the amount of emitted infrared radiation is related to the emissivity value of surfaces, the emissivity of concrete surface is usually lower than that of grass surface throughout a year. Thus, the emitted infrared radiation from concrete surface is expected to be less.

Diurnal Variations of four radiation components

A diurnal variation of four radiation components namely, Qs,sky (which equals to $Q_{S,TKL}$), Qs,gd Q_L,sky and Q_L,gd are shown in Figures 7.3 (a) to (d) respectively. Four selected months (January, March, July and October) were displayed. The data of March and July 2007 were based on the grass surface (lines without square markers) while the data of October 2007 and January 2008 were based on the concrete surface (lines with square markers).

The diurnal variation of the global solar radiation from the sky Qs,sky showed rather smooth bell-shape curves (see Figure 7.3 (a)). In general, Qs,sky is directly related to the solar zenith angle. In Hong Kong, solar zenith angle reaches zero degree (overhead sun) at solar noon in June and increases to 45 degree at solar noon in December. Figure 7.3 (a) demonstrates that in July 2007 the peak value of average Qs,sky was 2.78 $MJm^{-2}hr^{-1}$ (772 Wm^{-2}) and in March 2007 the peak value of Qs,sky was 1.50 $MJm^{-2}hr^{-1}$ (417 Wm^{-2}).

The diurnal variation of Qs,gd is very similar to Qs,sky (see Figure 7.3 (b)) since the sky radiation is the key source for ground reflection. However, the magnitude of Qs,gd is much smaller than Qs,sky due to a substantial amount of solar heat absorbed by the ground.

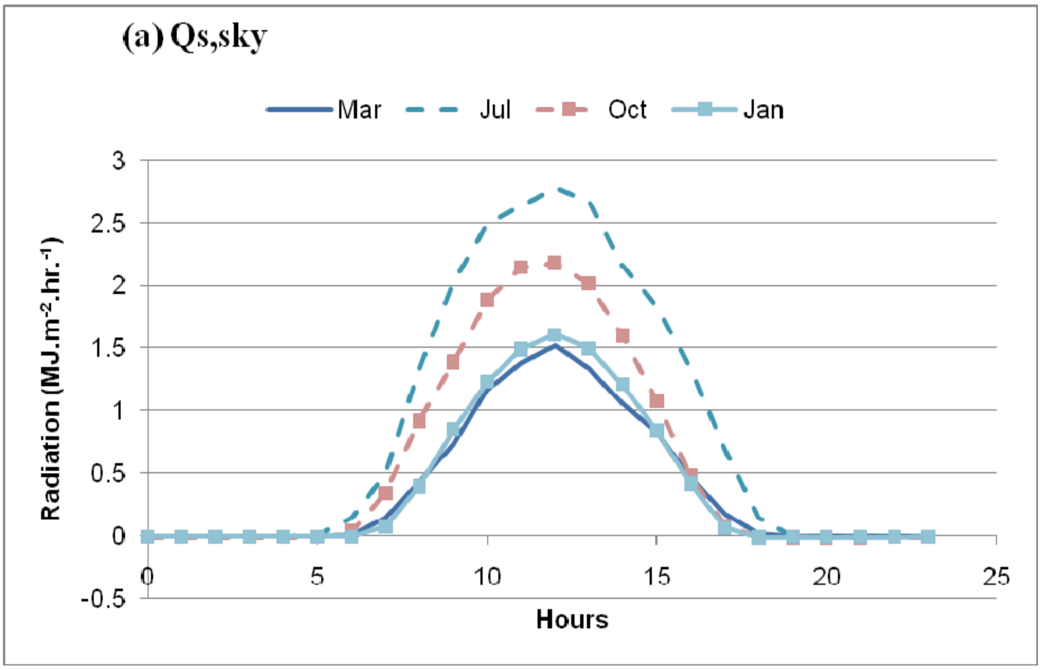

(a) Qs,sky
Mar
Jul
Oct
Jan
Radiation (MJ.m-2.hr.-1)
Hours
3
2.5
2
1.5
1
0.5
0
-0.5
0
5
10
15
20
25

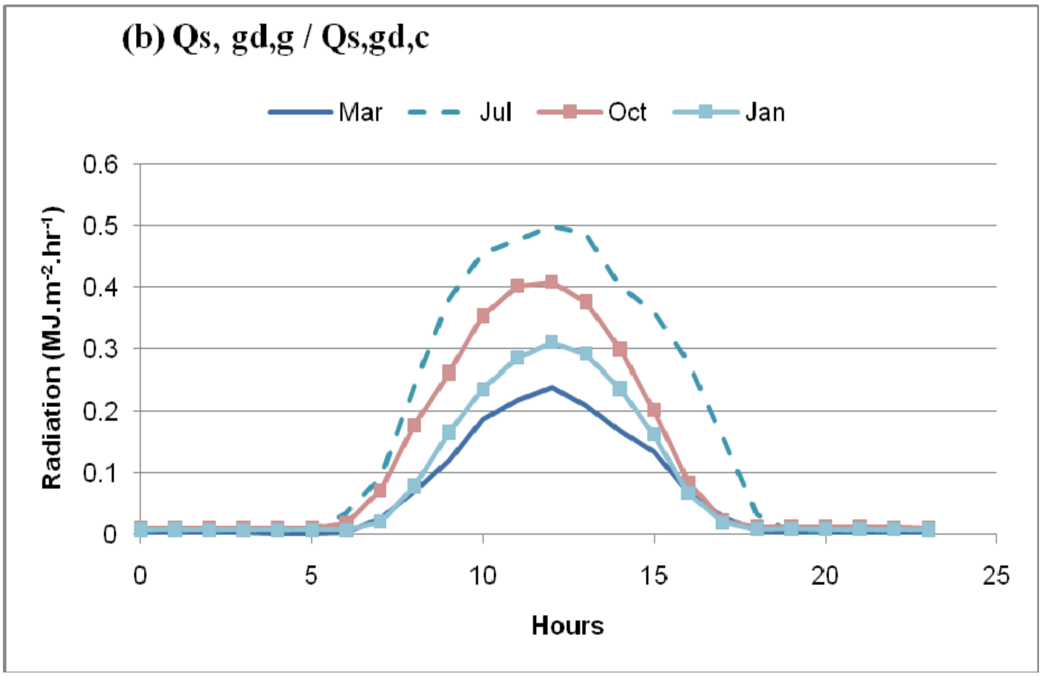

(b) Qs, gd,g / Qs,gd,c
Mar
Jul
Oct
Jan
Radiation (MJ.m-2.hr-1)
Hours
0.6
0.5
0.4
0.3
0.2
0.1
0
0
5
10
15
20
25

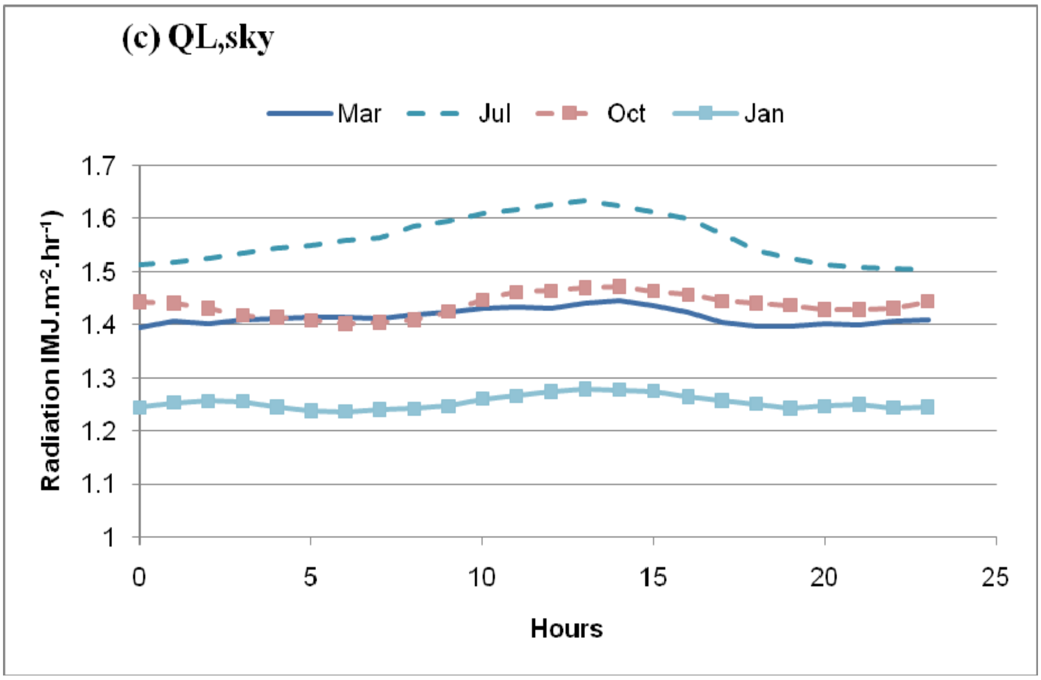

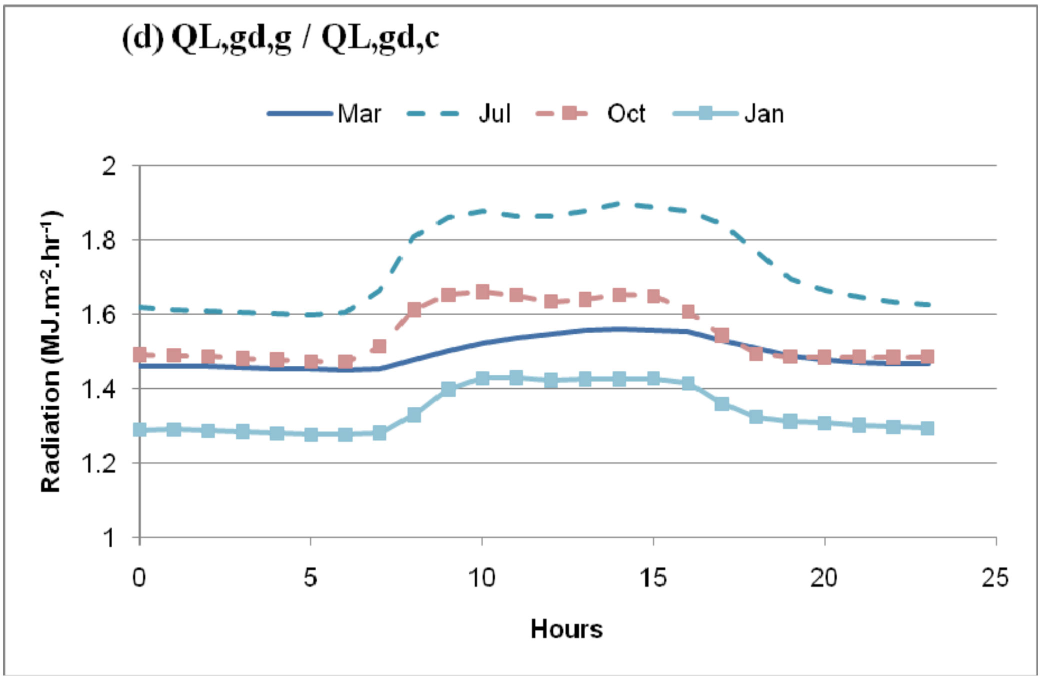

Figure 7.3 Diurnal variations of (a) solar radiation from the sky, Qs,sky, (b) solar radiation emitted from the ground surface, Qs,gd,g / Qs,gd,c, (c) infrared radiation from the sky, Q_L,sky, (d) infrared radiation emitted from the ground surface, Q_L,gd,g / Q_L,gd,c in four selected months (March and July – grass surface ; October and January – concrete surface)

The diurnal variations of the infrared radiation (Q_L,sky and Q_L,gd) were quite different from the solar radiation. Q_L,sky and Q_L,gd are theoretically related to the temperatures of the atmosphere and the ground surface respectively according to the Stefan–Boltzmann law. Therefore, both Q_L,sky and Q_L,gd exhibited a diurnal change that resembled a change in air temperatures and ground surface temperatures respectively. As Q_L,sky depends on the infrared radiation emission from all layers of air above it, the diurnal change of Q_L,sky (Figure 7.3 (c)) was much less pronounced than that of Q_L,gd (Figure 7.3 (d)). Furthermore, the peak hour of Q_L,gd was generally 1 hour later than that of Qs,sky, due to the heat transfer delay. The average of Q_L,sky at 13:00 in July 2007 reached 1.63 $MJm^{-2}hr^{-1}$ (453 Wm^{-2}) and it dropped to 1.28 $MJm^{-2}hr^{-1}$ (356 Wm^{-2}) at 13:00 in January 2008. The infrared radiation emitted from the ground Q_L,gd was generally higher than the incoming infrared radiation from the sky, Q_L,sky. Q_L,gd in the afternoon at 14:00 reached 1.90 $MJm^{-2}hr^{-1}$ (528 Wm^{-2}) in July 2007 (grass surface) and it dropped to 1.42 $MJm^{-2}hr^{-1}$ (394 Wm^{-2}) at 14:00 in January 2008 (concrete surface).

<u>Net radiation</u>

Net radiation heat gain Q^* in $MJm^{-2}hr^{-1}$ is defined as Qs,sky + Q_L,sky – Qs,gd – Q_L,gd. Table 7.1 exhibits that daytime monthly mean Q^* (sum of hourly Q^* from 5:00 to 19:00) dominates the surface energy budget. Over the grass surface, Q^* increased from 0.43 $MJm^{-2}hr^{-1}$ (119 Wm^{-2}) in March 2007 to 1.05 $MJm^{-1}hr^{-1}$ (292 Wm^{-2}) in August 2007. Over the concrete surface, Q^* decreased from 0.79 $MJm^{-2}hr^{-1}$ (219 Wm^{-2}) in September 2007 to 0.40 $MJm^{-2}hr^{-1}$ (111 Wm^{-2}) in January 2008. In general, daytime Q^* was higher during hot seasons and lower during cold seasons. There is some indication that during daytime Q^* over the grass surface is slightly larger than Q^* over the concrete surface but the difference in Q* between two surfaces is not apparent. During nighttime, in the absence of solar radiation, Q^* is dominated by outgoing infrared radiation and no obvious seasonal variation pattern is observed. Over the grass surface, nighttime Q^* ranged between -0.06 $MJm^{-2}hr^{-1}$ (-16 Wm^{-2}) and -0.13 $MJm^{-2}hr^{-1}$ (-36 Wm^{-2}). Over the concrete surface, nighttime Q^* ranged between -0.03 $MJm^{-2}hr^{-1}$ (-8 Wm^{-2}) and -0.14 $MJm^{-2}hr^{-1}$ (-39 Wm^{-2}). On average, the grass surface was gaining 9.66 $MJm^{-2}day^{-1}$ (112 Wm^{-2}) during daytime due to solar radiation, it was losing 0.80 $MJm^{-2}day^{-1}$ (-9 Wm^{-2}) during nighttime due to outgoing infrared radiation (not shown in Figure 7.3). For the concrete surface, it was gaining 7.84 $MJm^{-2}day^{-1}$ (91 Wm^{-2}) during daytime and losing 0.67 $MJm^{-2}day^{-1}$ (-8 Wm^{-2}) during nighttime. Nighttime Q^* is nearly one order of magnitude smaller than daytime Q^*. Overall speaking, daytime heating has a stronger effect than nighttime cooling. Therefore, there is a net heat gain on the ground surface. The greenhouse effect is also observed from the magnitude of Q_L,sky. It can be seen in Table 7.1 that Q_L,sky is of about the same magnitude as Q_L,gd but always smaller. So in terms of infrared radiation, heat is always radiated out to Space round-the-clock no matter during daytime or nighttime. If the atmosphere is taken away, Q^* would be very different. First, Q_L,sky would be mostly eliminated leaving only the solar emitted infrared radiation. This will result in a drop of surface temperature. Q_L,gd will decrease and at the same time, Qs, sky will increase due to the absence of cloud and gas absorption. Without the atmosphere, using Stephan Boltzmann law, let the absorbed sunlight be 240 Wm^{-2}, the earth's average surface temperature would be -18.0°C.

Table 7.1 Monthly mean of hourly net radiation in $MJm^{-2}hr^{-1}$ observed at Ta Kwu Ling between March 2007 and February 2008

		Daytime 5:00 to 19:00					Nighttime 20:00 to 4:00				
		$Q_{s,sky}$	$Q_{s,gd}$	$Q_{L,sky}$	$Q_{L,gd}$	Q*	$Q_{s,sky}$[1]	$Q_{s,gd}$	$Q_{L,sky}$	$Q_{L,gd}$	Q*
Grass	Mar	0.62	0.10	1.42	1.51	0.43	0.00	0.00	1.40	1.46	-0.06
	Apr	0.79	0.13	1.43	1.57	0.52	0.00	0.01	1.40	1.48	-0.09
	May	1.07	0.18	1.52	1.68	0.73	0.00	0.01	1.47	1.57	-0.11
	June	0.96	0.19	1.60	1.77	0.60	0.00	0.01	1.55	1.61	-0.07
	July	1.38	0.26	1.59	1.80	0.91	0.00	0.01	1.52	1.62	-0.11
	Aug	1.39	0.22	1.57	1.69	1.05	0.00	0.01	1.49	1.61	-0.13
Concrete	Aug	0.89	0.13	1.59	1.67	0.68	-0.01	0.01	1.54	1.56	-0.03
	Sep	1.08	0.18	1.53	1.64	0.79	-0.01	0.01	1.49	1.53	-0.06
	Oct	0.94	0.18	1.44	1.58	0.62	-0.01	0.01	1.43	1.49	-0.08
	Nov	0.94	0.19	1.26	1.48	0.53	-0.01	0.01	1.26	1.38	-0.14
	Dec	0.76	0.16	1.27	1.46	0.41	-0.01	0.01	1.26	1.35	-0.11
	Jan	0.64	0.13	1.26	1.37	0.40	-0.01	0.01	1.25	1.29	-0.06
	Feb	0.66	0.13	1.24	1.32	0.46	-0.01	0.01	1.25	1.27	-0.03

[1] *Negative value may be measured during the nighttime due to an instrument discrepancy. The accuracy of measured value is about 10% of daily totals.*

7.1.2 Underground soil temperatures

<u>Seasonal variation</u>

The profiles of monthly mean soil temperatures are shown in Figure 7.4. In general, a seasonal variation of the soil temperatures was observed. The soil temperatures were higher in summer, which is related to strength of absorbed solar radiation. In August 2007, over the grass surface, the highest soil temperature of 33.1°C was observed in 0.05 m just below the grass surface ($T_{-5,g}$) while the soil temperature in 1.25 m below the grass surface ($T_{-125,g}$) was only 29.7°C, which was about 3.4°C less than the surface. Even there was a significant difference between the monthly mean soil temperatures in surface soil layer and deeper layer, seasonal variations for all layers over grass surface were clearly observed. Since 17 August 2007, the soil temperature measurement was moved over the concrete surfaces. As shown in Figure 7.4, both ambient temperatures ($T_{180,c}$, $T_{20,c}$) above the concrete surface are notably lower than the temperatures measured at the surface. During the measurement, the soil under concrete is much hotter than above ground surface. There is a fundamental difference in soil temperature variation underneath grass and concrete surface. The soil temperature beneath grass first began to increase when the depth increase. The soil temperature reaches a maximum at about 0.2 m. On further descend, the soil temperature starts to cool. When it reached a depth of 1.25 m, the soil temperature was similar to the ambient temperature. Under the concrete surface, the soil was hot. The soil temperature continues to increase with depth. When it reached a depth of 1.4 m, the temperature was still higher than all soil layer aloft.

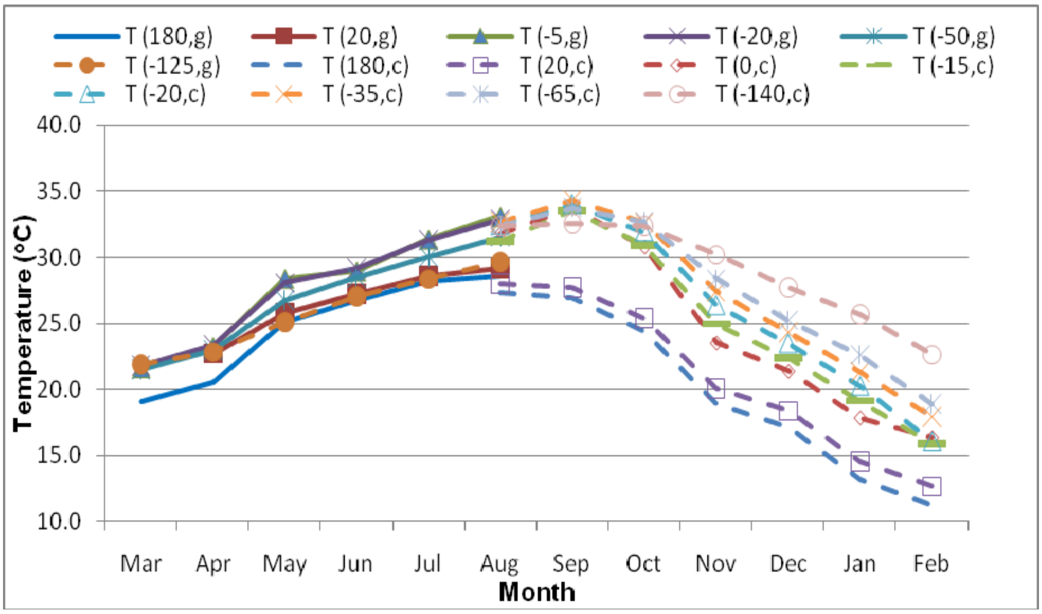

Figure 7.4 Monthly mean temperatures over the grass layer (May to August) and over the concrete layer (August to February)

Based on the observation in the first two months after sensor installation (March and April for the grass surface; August and September for the concrete surface), the readings of all soil temperatures with the depth greater than 0.5 m were similar. However, since the third month of the samplings, the readings in all depths were able to be distinguished clearly and could represent the temperatures in such depths. It took about 2 months' time for the soil temperature to reach equilibrium after the sensors burial. This finding suggested that at least two months quarantine is needed for the soil temperature measurement and the length of quarantine time is related to the depth of soil sensors. It is noted that this quarantine time did not affect the heat flux measurement because a clear diurnal variation of soil temperatures in surface layers was used to calculate soil heat flux.

A seasonal analysis for daily mean soil temperatures is then analyzed to explore the properties of four vertical underground temperatures. As shown in Figure 7.5, quasi-periodical waves were observed in T_{-5} and T_{-20} but only one concave curve was observed in T_{-125}. These findings support that the soil temperature in shallow soil with depth less than 0.5 m (T_{-5}) are more sensitive to heat and cold waves due to weather change in the atmosphere but the soil temperature in 1.25 m depth (T_{-125}) is almost immune to those changes. Take T_{-5} as an example. The duration of heat waves ranged from 8 to 20 days on average while the duration of cold waves ranged from 10 to 35 days. The cold drainages from the mainland China was much stronger than the warm drainages from South China Sea in 2007/2008. However, there was no clear impact of hot and cold waves on T_{-125}. These findings show that the measured temperature in the depth of 1.25 m is adequate to represent underground temperature where the impact of the daily solar radiation on ground temperatures is considered as negligible. This implies that the temperature stability in soil increases with the depth. This stable and cold environment in a deep layer may be a useful for cooling system during hot season. This innovative cooling / warming system may be developed to abate the heat emitted due to urbanization. On contrary, the underground warm environment during cold season is also useful in warming system, especially in high-latitude cities.

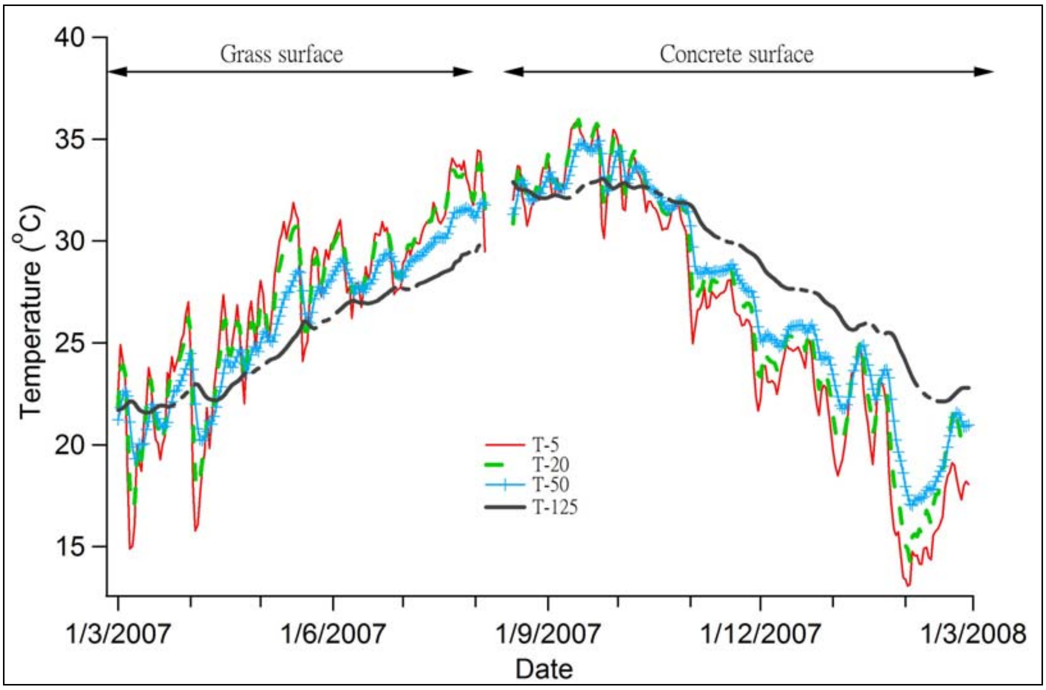

Figure 7.5 Daily average of underground soil temperatures throughout the year (March 2007 to February 2008) [Grass surface – 2 March 2007 to 6 August 2007; Concrete surface – 17 August 2007 to 28 February 2008]

Diurnal variation

Figure 7.6 shows the monthly mean of hourly temperature profiles over grass and concrete surfaces at four specific times (0:00, 6:00, 12:00 and 18:00) in March, July, September and February. A diurnal variation at the top surface layer (less than 0.2 m) was clearly observed over both grass and concrete surfaces but there was no significant diurnal temperature change with a depth of 0.2 m or deeper over two surfaces. Over grass surface, T_{-5} ranged from 19.6^{o}C at 6:00 in March to 37.2^{o}C at 18:00 in August; T_{-20} ranged from 20.9^{o}C at 12:00 to 34.2^{o}C at 18:00; T_{-50} ranged from 21.4^{o}C at 18:00 to 31.6^{o}C at 6:00 and T_{-125} also ranged from 21.9^{o}C at 6:00 to 28.9^{o}C at 0:00. Over concrete surface, T_0 ranged from 13.3^{o}C at 6:00 in February 2008 to 40.1^{o}C at 12:00 in September 2007; T_{-15} ranged from 11.8^{o}C at 0:00 to 36.2^{o}C at 18:00; T_{-20} ranged from 15.0^{o}C at 12:00 to 35.0^{o}C at 18:00; T_{-35} ranged from 17.7^{o}C at 12:00 to 34.7^{o}C at 0:00; T_{-65} ranged from 18.9^{o}C at 18:00 to 33.8^{o}C at 6:00 and T_{-140} also ranged from 22.6^{o}C at 0:00 to 32.5^{o}C at 0:00. These findings show that the relatively high temperatures measured at the top surface were usually recorded before the sunset (18:00) over both surfaces while the associated values in deeper level was measured at dawn. This implies that the soil temperatures at the top surface is likely correlated to the solar radiation

As shown in Figure 7.6, the vertical patterns of soil temperatures at specific time were almost the same over both grass and concrete surfaces. Over grass surface, heat energy was transmitted from the surface layer to the ground during daytime and vice versa at night. Over concrete surface, soil temperatures generally increased with the depth during cold season and decreased during hot season. The soil temperature gradient was much stable over concrete surface. This profile is still unclear. This result suggests that a continuous hourly soil temperature monitoring can help to understand the underground temperature gradient and soil heat flux. Hong Kong Observatory is currently measuring soil temperatures over grass surface with different depths at 7:00 and 19:00. This result is able to provide a preliminary soil measurement result over concrete surface in Hong Kong.

(a) Grass surface

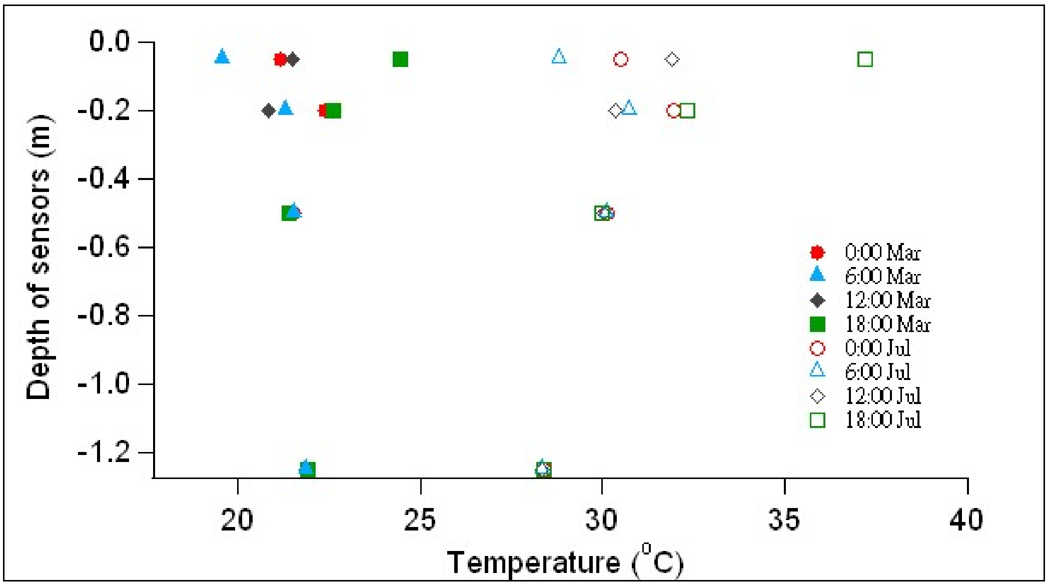

(b) Concrete surface

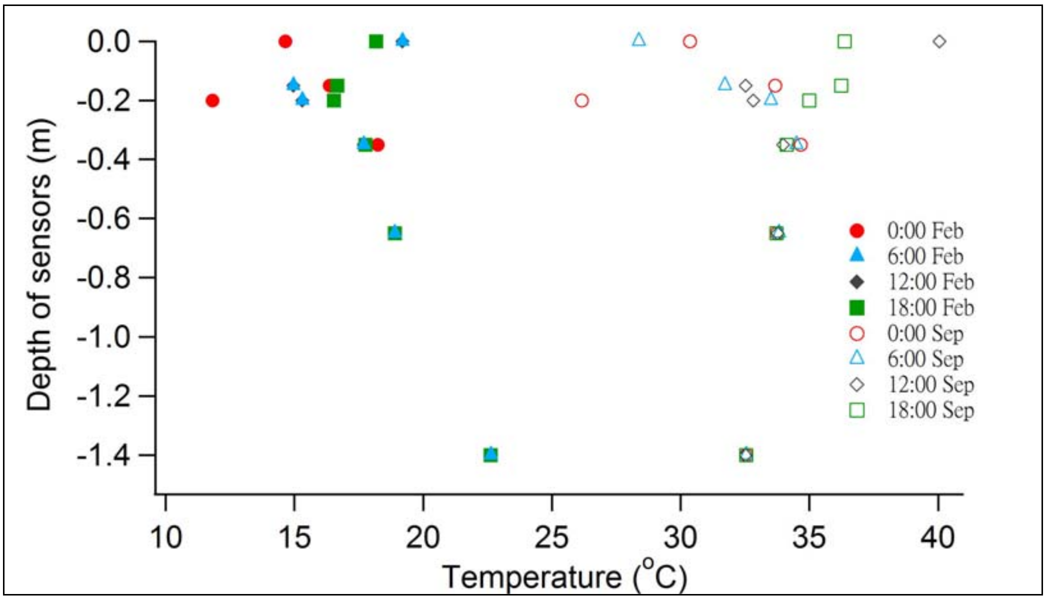

Figure 7.6 Mean hourly temperatures in different soil depths at specific time (0:00, 6:00, 12:00, 18:00) (a) over the grass surface in March and July; (b) over the concrete surface in September and February

7.1.3 Heat fluxes

<u>Seasonal variation</u>

As shown in Figure 7.7, the monthly mean of daily net radiation Q* (orange line without any marks) varies from 5.32 $MJm^{-2}day^{-1}$ (62 Wm^{-2}) in December 2007 to 12.65 $MJm^{-2}day^{-1}$ (146 Wm^{-2}) in July 2007 were recorded. As expected, the net radiation is lower in winter (December) and higher in summer (July). Net radiation is absorbed from the ground surface and was converted to other forms of energy. In this study, three converted heat fluxes were measured and they were soil heat, sensible heat and latent heat. The findings show that the monthly mean of daily soil heat flux stored over grass surface Q_G,g (blue solid line with diamond marks) ranged from -1.69 $MJm^{-2}day^{-1}$ (-20 Wm^{-2}) in May to 2.88 $MJm^{-2}day^{-1}$ (33 Wm^{-2}) in July and the associated range over the concrete surface Q_G,c (blue dotted line with diamond marks) was between -1.61 $MJm^{-2}day^{-1}$ (-19 Wm^{-2}) in November and 0.05 $MJm^{-2}day^{-1}$ (0.6 Wm^{-2}) in September. Negative values mean the overall daily soil heat is losing from the ground, especially during cold seasons. This phenomenon can be observed in diurnal variation of soil heat flux, which is going to be discussed in the following section. For sensible heat flux Q_H, the monthly mean value over the grass surface (red solid line with triangle marks) increased from 1.35 $MJm^{-2}day^{-1}$ (16 Wm^{-2}) in June and 2.98 $MJm^{-2}day^{-1}$ (34 Wm^{-2}) in July and the associated range over the concrete surface (red dotted line with triangle marks) ranged from 2.41 $MJm^{-2}day^{-1}$ (28 Wm^{-2}) in December and 4.25 $MJm^{-2}day^{-1}$ (49 Wm^{-2}) in September. It seems that the overall monthly sensible heat flux over concrete surface was slightly higher than these over grass surface and there were no seasonal variations. For latent heat flux Q_E, the monthly mean value over the grass surface (green solid line with square marks) increased from 3.04 $MJm^{-2}day^{-1}$ (35 Wm^{-2}) in March to 9.19 $MJm^{-2}day^{-1}$ (106 Wm^{-2}) in May while the associated range over the concrete surface (green dotted line with square marks) decreased from 7.62 $MJm^{-2}day^{-1}$ (88 Wm^{-2}) in August 2007 to 3.84 $MJm^{-2}day^{-1}$ (44 Wm^{-2}) in December. It was found that a seasonal variation of daily latent heat flux existed. This variation may not be related to the land surfaces because the heat flux measurement at Ta Kwu Ling over both surfaces was dominated by the same microclimate. It should be noted that the number of successful measurement of sensible and latent heat fluxes was different among 12 months due to the site relocation in August and bad weather conditions.

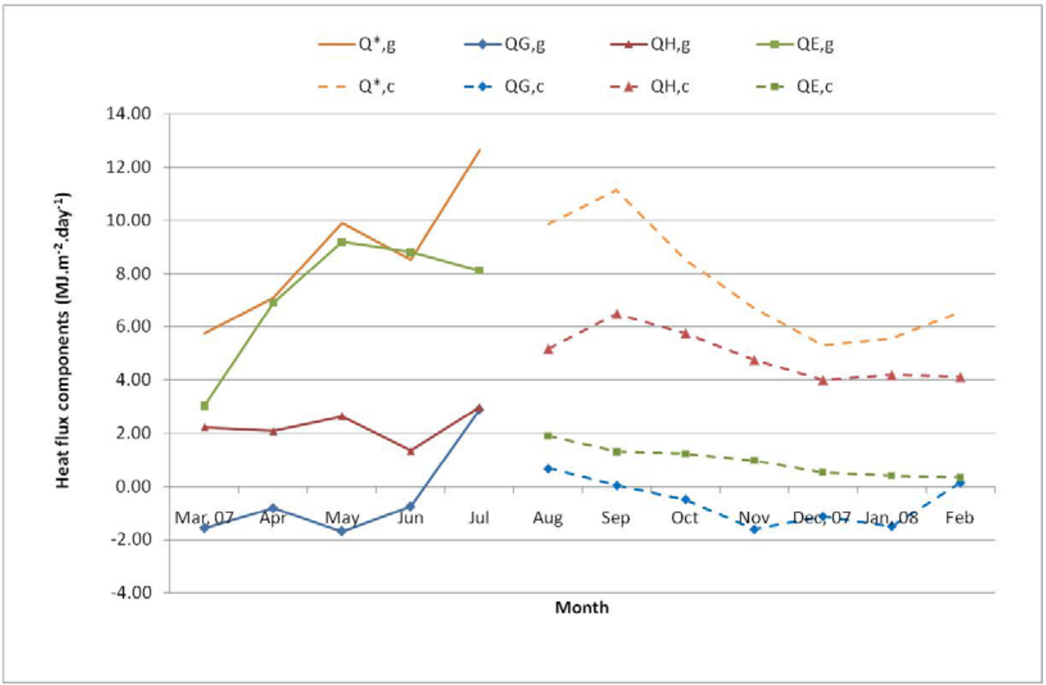

Figure 7.7 Monthly mean of daily net radiation (Q*,g; Q*,c), soil heat flux (Q_G,g; Q_G,c), sensible heat flux (Q_H,g; Q_H,c) and latent heat flux (Q_E,g; Q_E,c) at Ta Kwu Ling on selected days of each month (Grass surface: March – July 2007; Concrete surface: August 2007 – February 2008)

<u>Diurnal variation of Soil heat flux</u>

Figure 7.8 demonstrates the monthly mean of hourly Q_G over grass and concrete surfaces. In general, the shape of soil heat flux over grass surface is bell sharp and directly related to net radiation. The positive sign of the bell shape means heat gaining by soil during the daytime and the negative sign heat losing at night. This heat gain was from the solar radiation during the daytime and such loss was resulted from the infrared radiation emission at night. Over grass surface, the monthly mean of hourly Q_G reached the peak of 75 Wm^{-2} (0.27 $MJm^{-2}hr^{-1}$) at 14:00 in summer and 58 Wm^{-2} (0.21 $MJm^{-2}hr^{-1}$) in winter. Over the concrete surface, maximum value of hourly Q_G in summer was approximately 92 Wm^{-2} (0.33 $MJm^{-2}hr^{-1}$) at 14:00, which was about 39 Wm^{-2} (0.14 $MJm^{-2}hr^{-1}$) higher than that at 15:00 in winter. As mentioned in section 7.1.3, the daily soil heat flux was higher in summer over grass surface. The finding of this section shows that the nighttime soil heat fluxes over grass surface were the highest no matter the change of season and land cover. One possible reason is that the soil

moisture content is usually high in raining seasons and the soil heat capacity is high too. As such, the capacity of soil heat flux storage is generally higher in summer and the nighttime energy emitted from the ground is much more than these in other seasons. This infers that soil heat flux is relatively the main heat source at night as the key main source of net radiation is gone after the sunset. During nighttime, such soil heat flux as a heat source is subsequently converted to sensible and latent heats.

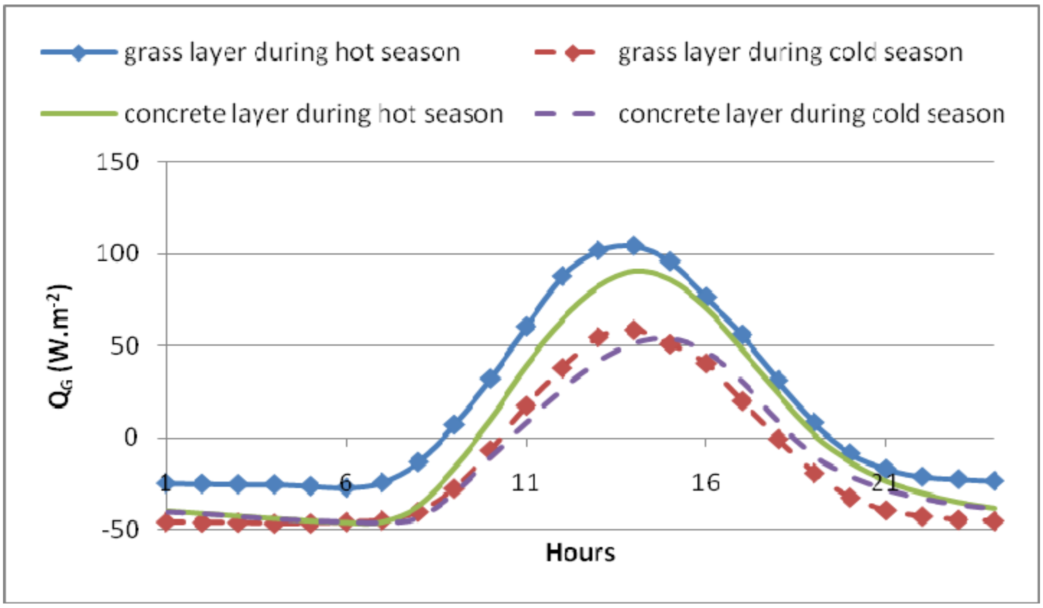

Figure 7.8 Mean of hourly soil heat flux over grass and concrete surfaces on selected days during hot and cold seasons

Diurnal variation of sensible heat

As shown in Figure 7.9, the shape of monthly mean of hourly sensible heat fluxes Q_H over grass surface were almost the same during both hot and cold seasons (blue and red lines with diamond marks). The nighttime hourly values were slightly negative but were more or less zero. The maximum of this Q_H was about 103 Wm^{-2} (0.37 $MJm^{-2}hr^{-1}$) at 13:00 and the magnitudes of diurnal variation were almost the same. This infers that the average sensible heat flux over grass surface does not change much throughout a year. Over the concrete surface, there is a difference in daytime hourly Q_H between hot and cold seasons, especially after noon. The measured hourly Q_H during hot season (green solid line) was slightly 12 Wm^{-2} (0.04 MJm^{-2}hr^{-1}) on average higher than that during cold season (purple dotted line). Compared the Q_H data after the sunset, the values over the concrete surface were significantly higher than these over the grass surface. One of the possible explanations is that a certain amount of heat stored in concrete surfaces keeps the heat emission after the sunset until the sunrise and then the duration of heat lose lasts longer over concrete surfaces. The air over concrete surface keeps warmer at night. This is also a contribution of heat island effect happened in urban areas.

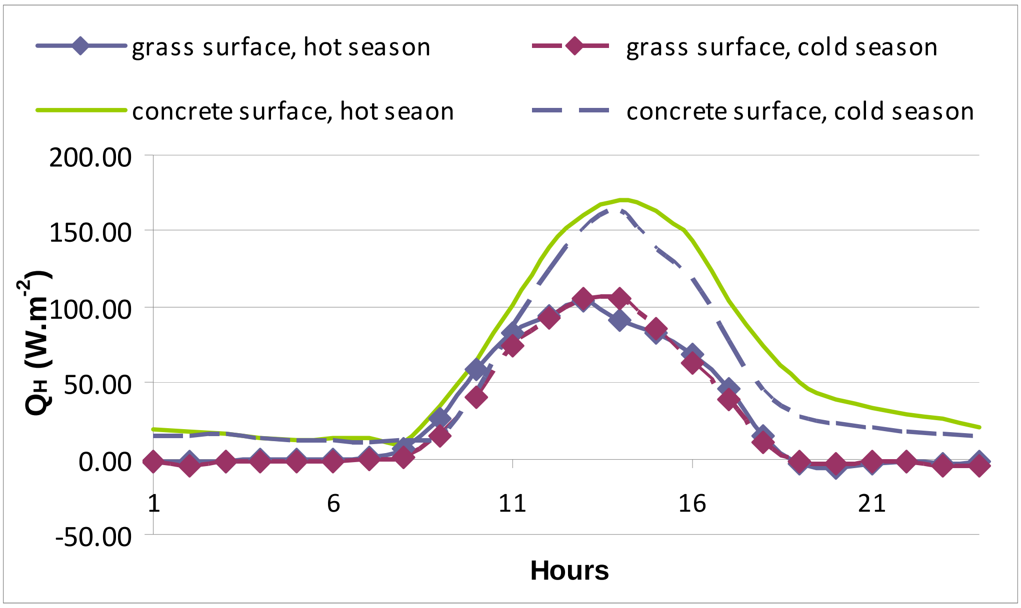

Figure 7.9 Mean of hourly sensible heat flux over grass and concrete surfaces on selected days during hot and cold seasons

Diurnal variation of latent heat flux

Figure 7.10 depicts the mean of hourly latent heat flux Q_E over grass and concrete surfaces during both hot and cold seasons. Over grass surface, hourly Q_E during cold season (blue line with diamond marks) ranged from 3.5 Wm^{-2} (0.01 MJm^{-2}hr^{-1}) at 21:00 to 209.1 Wm^{-2} (0.75 MJm^{-2}hr^{-1}) at 13:00 and the associated value during hot season (red dotted line with diamond marks) was between 2.6 Wm^{-2} (0.01 MJm^{-2}hr^{-1}) at 20:00 and 338.3 Wm^{-2} (1.22 MJm^{-2}hr^{-1}) at 13:00. The difference in the highest Q_E values between two seasons was around 164.2 Wm^{-2} (0.59 MJm^{-2}hr^{-1}) on average at 12:00. Over concrete surface, the minimum value of Q_E was observed at night and they were about 1.0 Wm^{-2}

(0.01 $MJm^{-2}hr^{-1}$) during the cold season (purple dotted line) and 2.4 Wm^{-2} (0.01 $MJm^{-2}hr^{-1}$) during the hot season (green solid line). The peak value of Q_E was 20.0 Wm^{-2} (0.07 $MJm^{-2}hr^{-1}$) at 14:00 during cold season and the corresponding value was 50.2 Wm^{-2} (0.18 $MJm^{-2}hr^{-1}$) at 14:00 during hot season. The difference in the highest Q_E values between two seasons was only 30.2 Wm^{-2} (0.11 $MJm^{-2}hr^{-1}$) on average at 14:00 over concrete surface, which was much less than those over grass surface of 164.2 Wm^{-2}. In addition, this finding showed that the seasonal variation of hourly Q_E is much obvious over grass surfaces because the soil moisture in grassland varies seasonally and the evaporation over the surfaces is always higher in rainy seasons (hot seasons in a subtropical city). On contrary, a good water runoff system over concrete surface avoids the water retarding on the floor and the water evaporation rates are similar throughout a year.

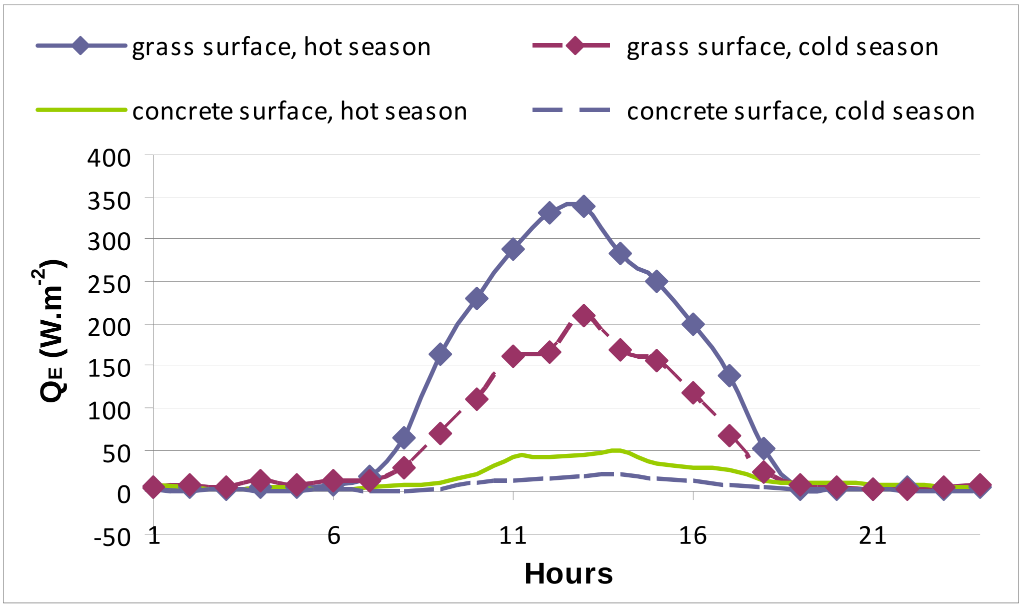

Figure 7.10 Monthly mean hourly latent heat fluxes over grass and concrete surfaces during hot and cold seasons

7.2 Impacts of a land surface change

7.2.1 Solar and infrared radiations

Average hourly solar and infrared radiations emitted from the ground over grass and concrete surfaces are shown in Figures 7.11 (a) and (b) respectively. The measured solar radiation at night is zero. The available radiation data over the grass and concrete surfaces is grouped into two periods: hot and cold seasons. Hot season is from 15 April to 14 October and cold season from 15 October to 14 April. For the grass surface, 5404 data was available in the hot season and 2112 data in the cold season. For the concrete surface, 2552 data and 6548 data are available in the hot and cold seasons respectively.

As shown in Figure 7.11 (a), the mean hourly Qs,gd decreased from 35.7 Wm^{-2} (0.13 $MJm^{-2}hr^{-1}$) (grass) to 29.3 Wm^{-2} (0.10 $MJm^{-2}hr^{-1}$) (concrete) during the hot season and the corresponding value increased from 17.6 Wm^{-2} (0.06 $MJm^{-2}hr^{-1}$) (grass) to 28.1 Wm^{-2} (0.10 $MJm^{-2}hr^{-1}$) (concrete) during the cold season. The percentages of change are around -18% and 60% respectively. The standard deviation of the mean hourly solar radiation over the concrete surface is about 42.7 Wm^{-2} (0.15 $MJm^{-2}hr^{-1}$) during the hot season and remains almost the same during the cold season. The standard deviation over the grass surface changed from 50.1 Wm^{-2} (0.18 $MJm^{-2}hr^{-1}$) during the hot season to 30.2 Wm^{-2} (0.11 $MJm^{-2}hr^{-1}$) during the cold season. The results suggest that grass is more shiny than concrete in the hot season and this shininess diminishes in the cold season. In addition, solar radiation reflected from the grass surface changes considerably from summer to winter while solar radiation reflected from the concrete surface remains rather constant.

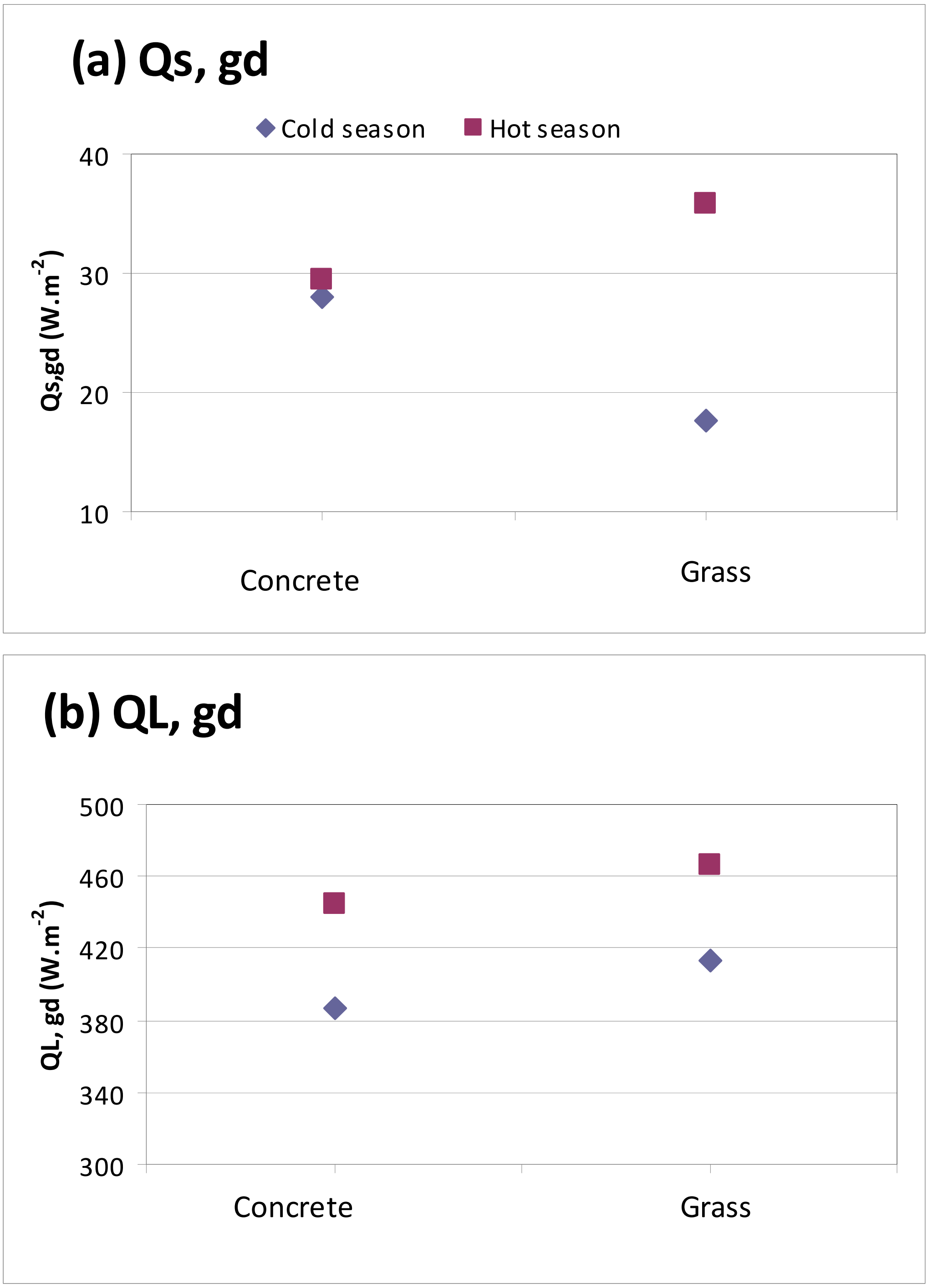

Figure 7.11 Average hourly of (a) solar radiation emitted and (b) infrared radiation emitted from the ground over concrete and grass surfaces

Regarding infrared radiation emitted from the ground (Q_L,gd), changing the surface from grass to concrete, the mean hourly Q_L,gd decreased slightly from 465.7 Wm^{-2} (1.68 $MJm^{-2}hr^{-1}$) (grass) to 444.9 Wm^{-2} (1.60 $MJm^{-2}hr^{-1}$) (concrete) during the hot season and decreased from 413.4 Wm^{-2} (1.49 $MJm^{-2}hr^{-1}$) (grass) to

387.3 Wm^{-2} (1.39 $MJm^{-2}hr^{-1}$) (concrete) during the cold season. The standard deviations over both grass and concrete surfaces were around 31 Wm^{-2} (0.11 $MJm^{-2}hr^{-1}$) throughout the year. This shows that the change of land cover will possibly cause an even change in Q_L,gd throughout the year. Overall, over the concrete surface, less heat loss associated with the out-going infrared radiation is compared with that over the grass surface. This is another factors contributing to heat island effect.

7.2.2 Heat fluxes on episode days

Based on results of heat island intensity in section 6.2, the maximum UHII in Hong Kong usually happens on a clear sky day. In this section, the energy balance over grass and concrete surfaces on clear sky days in both summer and winter are discussed in order to investigate the impact of land use change on three heat fluxes: soil heat, sensible heat and latent heat. Four selected days were 18 April 2007 (over grass surface in winter), 26 July 2007 (over grass surface in summer), 27 September 2007 (over concrete surface in summer) and 27 February 2008 (over concrete surface in winter).

The general properties of heat fluxes over two surfaces for a year were discussed in section 7.1.3. As such, individual heat flux profiles on four selected days are not shown. Figure 7.12 indicates the ratio of heat flux components to the total heat source on the four selected days. The heat flux components include soil heat Q_G, sensible heat Q_H, latent heat Q_E and others. The term "Others" means the remaining balance of the measured heat fluxes. Over the concrete surface, Q_G, Q_H and Q_E contributed around 13.7%, 68.7% and 6.3% to the heat source in the summer day; 9.6%, 55.8%, 10.5% in the winter day. Similar ratios for all these fluxes in clear sky days were found. This implies that heat fluxes are significantly dominated by concrete surfaces throughout a year. Over grass surface, Q_G decreased from 25.0% in the summer day to 1.0% in the winter day, Q_H slightly decreased from 28.9% to 21.0%; Q_E increased from 35.6% to 68.7%respectively. There was a significant reduction in Q_G and an increase in Q_E. Large soil moisture was measured in rainy seasons (summer). The larger the soil moisture, the larger is the soil heat capacity. Much more solar radiation in summer can be stored in the ground. Due to a reduction of water evaporation from hot season to cold season, the ratio of Q_E decreased accordingly. In addition, little change in Q_H was observed. It suggested that the vertical thermal change from grass surface to the air is less depended on seasonal weathers.

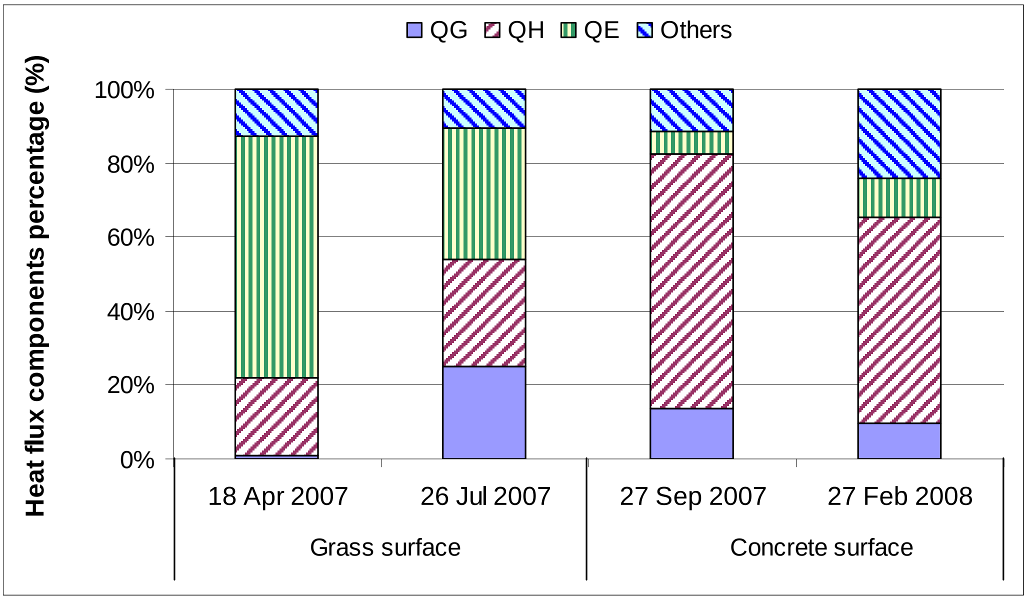

Figure 7.12 Ratio of daily heat flux components to total heat sources on four selected days, 18 April 2007 (over grass surface in winter), 26 July 2007 (over grass surface in summer), 27 September 2007 (over concrete surface in summer) and 27 February 2008 (over concrete surface in winter)

As expected, large amount of Q_H was found over concrete surfaces, which can explain the formation of heat island in terms of heat budget. Based on the results of Q_H ratio, there is a detectable impact on heat flux due to land cover change on a clear sky day. During the cold seasons, the ratio of Q_H to the heat source increased from around 21.0% over grass surface to 55.8% over concrete surface while this associated ratio during the hot season changed from 28.9% to 68.7%. The change of this ratio was about 166% during the cold season and was just 138% during the hot season. The impact of land surface change on sensible heat flux is significant in cold season. This implies that the UHII between rural/suburban (grass surface) and urban (concrete surface) could be larger in cold season. This finding supported the current observation in section 6.2 that the average UHII of 3.9^{o}C in winter was the highest for 19-year fixed station observation.

Another impact of a land surface change is related to Q_G. Since the concrete layer provides a good conductor and store a certain considerable amount of energy throughout a year, ratios of Q_G to the heat source are similar over the concrete surface. Over the grass surface, the amount of soil heat flux depends on the soil moisture. As such, there was no typical amount of Q_G stored in the soil layer. Therefore, it is hard to quantify the impact on Q_G when the land cover changed land from grass to concrete but there is a clear observation that Q_G over concrete surfaces remains almost constant throughout a year.

Further studies are needed to examine the certain unknown “Others” which are outstanding balance in this study. This energy may be resulted from anthropogenic heat generated nearby the site during the measurement. In addition, CO_2 flux may be another possible component even this flux value is considerably low when compared to other heat flux components. It should be noted that the results in this section were reported the heat flux measurement on clear sky days.

7.2.3 Albedo

Albedo is a ratio of the reflected radiation from a ground surface to the absorption of the incoming solar radiation on the ground surface. Albedo varies with the change of ground surface materials. In this study, the albedos over grass and concrete surfaces during the hot and cold seasons were determined. The results are shown in Figure 7.13.

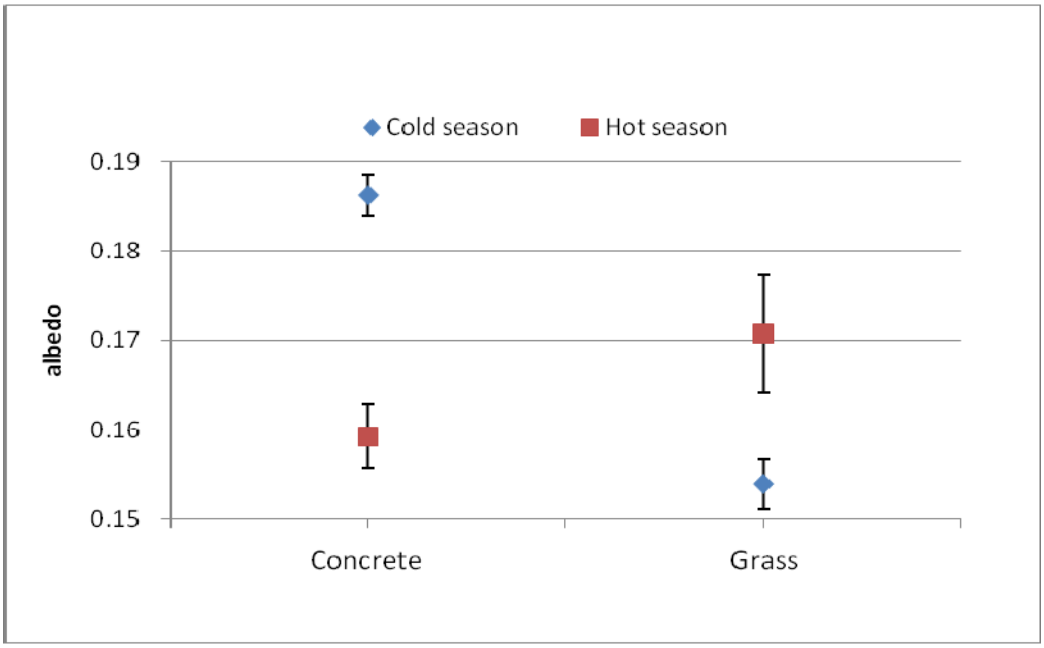

Figure 7.13 Mean of hourly albedos (from 9:00 to 16:00) over the concrete and grass surfaces during the hot and cold seasons (Cap of the bar – 95% upper and lower limits of the mean)

The albedos were calculated based on the daytime period from 9:00 to 16:00. The finding shows that during the hot seasons when the surface changed from grass to concrete, the average value of the mean hourly albedo decreased a little from 0.17 (grass) to 0.16 (concrete). Albedo decreased by about around 6%. During the cold seasons, the corresponding albedo value increased from 0.15 (grass) to 0.19 (concrete) (about 27% increase). The standard deviation of albedo over the concrete surface is similar in both hot and cold seasons while the corresponding standard deviation over the grass surface is larger in the hot seasons. Such change in albedo value could be explained by the water content in the grass surface. One possible reason may be that greenish grass reflects much more solar radiation during the hot seasons while withered grass does less during the cold seasons. Another possible explanation is that the water content itself on the ground surface could affect albedo. Nevertheless, the results show that both the seasonal change and the surface cover change from grass to concrete do not cause a large significant variation of albedo but there are subtle differences. This supports that albedo exhibits small seasonal change and less than 20% of solar radiation is generally reflected throughout the year no matter over grass and concrete surfaces. The albedos reported in this study could be useful in verifying the albedos used in numerical models.

Regarding the application of albedo value in numerical models, MM5 model was taken as a reference. In summer seasons, MM5 adopted albdeo value 0.19 over grass surface and 0.15 over concrete surface. In winter seasons, MM5 adopted albedo value 0.23 over grass surface and 0.15 over concrete surface (Dudhia et al. 2005). It is interesting to note that MM5 assumes a higher albedo in winter over grass surface, whereas the albedo over urban area does not change with season. However, this local measurement shows that the albedo over grass surface is higher in summer though the seasonal difference is not very large. Over the concrete surface, the local measurements results are quite similar to MM5 data base except that the local measurement results show a small seasonal change.

7.2.4 Emissivity

Emissivity of ground surface was also derived from the long-wave infrared radiation and the surface temperatures. According to the Stefan-Boltzmann law, the reflected energy is directly proportional to the fourth power of the thermodynamic temperature of the material. Hourly emissivity values were subsequently computed from 18:00 to 6:00. In this study, the emissivity over the two surfaces was calculated on clear sky days. Table 7.2 lists the emissivity over the grass and the concrete surfaces during winter and summer seasons. The results showed that the average emissivity values were 0.95 over the grass surface and 0.88 over the concrete surface respectively. The emissivity value over the concrete surface was considerably lower than that over the grass surface. These data imply that the change of land cover from grass to concrete can reduce the emissivity by 6.4% during winter season and by 8.4% during summer season.

Table 7.2 Emissivity measured in two surfaces of grassland and concrete and the albedo used in MM5 model [The value in the bracket is its standard deviation and its range]

Land surface	Winter season[1]		Summer season[2]	
	Our study (at 5-42 μm)	MM5 model (at 9 μm)	Our study (at 5-42 μm)	MM5 model (at 9 μm)
Grass	0.94 (0.027) [0.88-0.98]	0.92	0.95 (0.025) [0.87-1.00]	0.985
Concrete	0.88 (0.028) [0.80-0.96]	0.88	0.87 (0.034) [0.79-0.97]	0.88

(1) Winter season: 15 October – 14 April;

(2) Summer season: 15 April – 14 October

Sources: Dudhia et al. 2005

Compared to the emissivity value used in modelling, the experimental emissivity value over concrete surface was similar but this value over grass surface was different. The findings also reported that the emissivity value in modelling was lower than the measured data in this study during winter season and the corresponding data during summer season were relatively higher. However, the emissivity value in modelling falls within the range of experimental results. As the grid resolution in the MM5 model is 1 km or more, the emissivity value used in the MM5 model was estimated to represent the average value in a grid. Higher resolution of emissivity value for a microscale model might enhance model results.

7.3 Chapter summary

This chapter reported the heat flux results of net radiation, soil heat flux, sensible heat and latent heat of a 1-year intensive heat budget measurement at Ta Kwu Ling. Seasonal and diurnal variations of heat fluxes over grass and concrete surfaces were analyzed. Solar radiation from the sky is the primary source of heat gain and it was found that less than 20% of the incoming solar radiation is reflected by either grass or concrete surfaces. The ground loose heat through out-going infrared radiation but much of it was re-radiated back to the ground from the atmosphere through the Greenhouse effect. Regarding surface heat budget, the heat loss through infrared radiation during nighttime is roughly an order of magnitude smaller than the solar heat gain during daytime. On the whole, ground surface gains heat throughout the year.

The impacts of the land cover changing from grass surface to concrete surface on solar and infrared radiations, sensible heat flux, soil heat flux, albedo and emissivity were discussed. On a clear sky days, the change of the land cover from grass surfaces to concrete surfaces can increase the sensible heat flux in urban areas by around 165% in cold season and by almost 140% in hot season. Furthermore, the emissivity value can be reduced by at least 6.4% and the impact of land cover on albedo exhibits a small seasonal change. During hot seasons, albedo decreases by about around 6% from over grass surface to concrete surface. This value increases by about 27% during cold seasons. All these factors are likely contributing to the generation of urban heat island.

Chapter 8 : Conclusions

8.1 Summary of major scientific findings

Overall, the findings of this study were able to examine the characteristic of heat island intensity in Hong Kong and justify the impact of a land surface change on heat budget, albedo and emissivity. There are four specific points to be concluded as follows:

An existence of urban heat island in Hong Kong was confirmed and the average annual heat island intensity was about 2.7^{o}C. The urban heat island phenomenon often happens before the sunrise (4:00 - 6:00). As a matter of fact, sites within urban center could be cooler than the suburban area in the afternoon due to blockage of direct sun by tall buildings.

There is an increasing trend of heat island intensity during the past 2 decades. The annual UHII increased by 0.29^{o}C/decade. This trend could be due to urbanization.

Another key contribution is to compare the "accuracy" of satellite-derived surface temperatures with in-situ field measurement. Nighttime thermal image has a higher accuracy (about 3^{o}C) when compare with daytime images. In addition, an attempt was made to convert surface temperature acquired by satellite to air temperature. The conversion is satisfactory for winter nighttime images but not in summer daytime images. Further studies are required to test the applicability of such empirical equations in converting surface temperatures to ambient air temperatures.

An explorative heat budget measurement in the local climate was examined. Regarding the impact of heat island on heat budget, these results suggest that a change of land surface from grass to concrete can increase the storage of solar heat in concrete layers, increase in sensible heat, reduce emissivity values and affect albedo seasonally. Concrete also eliminate the latent heat component which could lead to an increase in sensible heat. Further heat budget research is needed to explore specifically in microclimate level.

8.2 Suggestions for future research

Based on the results and limitations of the current study, a few recommendations are suggested for future research as follows:

The current study showed a successful case of satellite-derived air temperature in a winter night. To improve the reliability of the derivation of satellite-derived air temperatures, a series of strategic measurements could be conducted to obtain a better understanding of temperature correlation and surface heat island studies.

The intensive underground temperature measurement at Ta Kwu Ling site was the first diurnal variation study. The results indicate the existence of underground cooling / heating potential. It is worthwhile to find out how to exploit this renewable energy and any possible mitigations of heat island impact.

This study measured four main heat flux components: net radiation, soil heat, sensible heat and latent heat. However, the results indicate that there is a unknown heat source and/or sink in heat budget measurement. Further study could consider exploring the source of anthropogenic heat and CO_2 in urban areas and understanding their significance in surface heat budget. A specific domain and setting of modelling for plants should be considered for a CO_2 flux simulation.

Chapter 9 : References

Abrams M., Hook, S. and Ramachandran B., 1998. ASTER User Handbook, Version 2. Jet Propulsion Laboratory, California Institute of Technology, pp 135.

Akbari H., 2002. Shade trees reduce building energy use and CO_2 emissions from power plants. Environmental pollution, 116, Supplement 1, 119-126.

Aniello C., Morgan K., Busbey A. and Newland L., 1995. Mapping micro-urban heat islands using LANDSAT TM and a GIS. Computers & geosciences, 21(8), 965-967.

Ashie Y., Thanh Ca, V. and Asaeda T., 1999. Building canopy model for the analysis of urban climate. Journal of wind engineering and industrial aerodynamics, 81(1-3), 237-248.

Baik J.J. and Chun, H.Y., 1997. A dynamical model for urban heat islands. Boundary layer meteorology, 83(3), 463-477.

Balling Jr. R.C. and Brazel S.W., 1989. High-resolution nighttime temperature patterns in Phoenix. Journal of the Arizona-Nevada Academy of Science, 23, 49-53.

Bejarán R.A. and Camilloni I.A., 2003. Objective method for classifying air masses: an application to the analysis of Buenos Aires' (Argentina) urban heat island intensity. Theoretical and Applied Climatology, 74(1-2), 93-103.

Bonacquisti V., Casale G.R., Palmieri S. and Siani A.M., 2006. A canopy layer model and its application to Rome. Science of the total environment, 364(1-3), 1-13.

Borghi S., Corbetta G. and De Biase L., 2000. A heat island model for large urban areas and its application to Milan. Nuovo cimento della socitetà italiana di fisica – C, geophysics and space, 23(5), 547-566.

Bottyán Z. and Unger, J., 2003. A multiple linear statistical model for estimating the mean maximum urban heat island. Theoretical and Applied Climatology, 75(3-4), 233-243.

Bottyán Z., Kircsi A., Szegedi S. and Unger J., 2005. The relationship between built-up areas and the spatial development of the mean maximum urban heat island in Debrecen, Hungary. International Journal of Climatology, 25(3), 405-418.

Brázdil R. and Budíková, M., 1999. An urban bias in air temperature fluctuations at the Klementinum, Prague, The Czech Republic. Atmospheric Environment, 33(24-25), 4211-4217.

Camilloni I. and Barros, V., 1997. On the urban heat island effect dependence on temperature trends. Climate Change, 37(4), 665-681.

Campbell Scientific, Inc., 2003. Instrument manual: HFT3 Soil heat flux plate. pp12.

Campbell Scientific, Inc., 2009. Instrument manual: CNR1 Net Radiation. pp40.

Carlson T.N., Dodd J.K., Benjanmin S.G. and Copper J.N., 1981. Satellite estimation of the surface energy balance, moisture availability and thermal inertia. Journal of Applied Meteorology, 20(1), 67-87.

Census and Statistics Department, 2007. Hong Kong Population Projections 2007-2036, Hong Kong Monthly Digest of Statistics. Census and Statistics Department, HKSAR.

Chandler T.J., 1965. The climate of London, (London), Hutchinson, pp292.

Chang C.R., Li M.H. and Chang S.D., 2007. A preliminary study on the local cool-island intensity of Taipei city parks. Landscape and Urban Planning, 80(4), 386-395.

Chen B., Chen J.M. and Ju W., 2007. Remote sensing-based ecosystem-atmosphere simulation scheme (EASS) – Model formulation and test with multiple-year data. Ecological Modelling, (209), 277-300.

Chen X.L., Zhao H.M., Li P.X. and Yin Z.Y., 2006. Remote sensing image-based analysis of the relationship between urban heat island and land use/cover changes. Remote Sensing of Environment, 104(2), 133-146.

Childs P.P. and Raman S., 2005. Observations and numerical simulations of urban heat island and sea breeze circulations over New York City. Pure and Applied Geophysics, 162(10), 1955-1980.

Chow W.T.L. and Roth M., 2006. Temporal dynamics of the urban heat island of Singapore. International Journal of Climatology, 26(15), 2243-2260.

Chung U., Choi J. and Yun, J.I., 2004. Urbanization effect on the observed change in mean monthly temperatures between 1951-1980 and 1971-2000 in Korea. Climatic Change, 66(1-2), 127-136.

Clarke J.F., 1969. Noctural urban boundary layer over Cincinnati, Ohio. Monthly Weather Review, 97(8), 582-589.

Dandou A., Tombrou M., Akylas E., Soulakellis N. and Bossioli E., 2005. Development and evaluation of an urban parameterization scheme in the Penn State/NCAR mesoscale Model (MM5). Journal of Geophysical Research, 110(D10102), pp14.

Deosthali V., 2000. Impact of rapid urban growth on heat and moisture islands in Pune City, India. Atmospheric Environment, 34(17), 2745-2754.

Dudhia J., Gill D., Manning K., Wang W., and Bruyere C., 2005. PSU/NCAR Mesoscale Modeling System Tutorial Class Notes and Users' Guide (MM5 Modeling System Version 3). Mesoscale and Microscale Meteorology Division, National Center for Atmospheric Research.

Dupont E., Menut L., Carissimo B., Pelon J. and Flamant P., 1999. Comparison between the atmospheric boundary layer in Paris and its rural suburbs during the ECLAP experiment. Atmospheric Environment, 33(6), 979-994.

Fan H. and Sailor D.J., 2005. Modeling the impacts of anthropogenic heating on the urban climate of Philadelphia: a comparison of implementations in two PBL schemes. Atmospheric Environment, 39, 73-84.

Fortuniak K., Kłysik K. and Wibig J., 2006. Urban-rural contrasts of meteorological parameters in Łódź. Theoretical and Applied Climatology, 84(1-3), 91-101.

Fung W.Y., Lam K.S., Hung W.T., Pang S.W. and Lee Y.L., 2006. Impact of urban temperature on energy consumption of Hong Kong. Energy, 31(14), 2623-2637.

Gallo K.P., Tarpley J.D., McNab A.L. and Karl T.R., 1995. Assessment of urban heat islands: a satellite perspective. Atmospheric Research, 37(1-3), 37-43.

Gedzelman S.D., Austin S., Cermak R., Stefano N., Partridge S., Quesenberry S. and Robinson D.A., 2003. Mesoscale aspects of the urban heat island around New York City. Theoretical and Applied Climatology, 75(1-2), 29-42.

Giridharan R., Ganesan S. and Lau, S.S.Y., 2004. Daytime urban heat island effect in high-rise and high-density residential developments in Hong Kong. Energy and Buildings, 36(6), 525-534.

Giridharan R., Lau S.S.Y. and Ganesan S., 2005. Nocturnal heat island effect in urban residential developments of Hong Kong. Energy and Buildings, 37(9), 964-971.

Giridharan R., Lau S.S.Y., Ganesan S. and Givoni B., 2007. Urban design factors influencing heat island intensity in high-rise high-density environments of Hong Kong. Building and Environment, 42(10), 3669-3684.

Gluch R., Quattrochi D.A. and Luvall J.C., 2006. A multi-scale approach to urban thermal analysis. Remote Sensing of Environment, 104(2), 123-132.

Goldreich Y., 1995. Urban climate studies in Israel – A review. Atmospheric Environment, 29(4), 467-478.

Hafner J. and Kidder S.Q., 1999. Urban heat island modeling in conjunction with satellite-derived surface/soil parameter. Journal of Applied Meteorology, 38(4), 448-465.

Hartz D.A., Prashad L., Hedquist B.C. Golden J. and Brazel A.J., 2006. Linking satellite images and hand-held infrared thermography to observed neighborhood climate conditions. Remote Sensing of Environment, 104(2), 190-200.

Hawkins T.W., Brazel A.J., Stefanov W.L., Bigler W. and Saffell E.M., 2004. The role of rural variability in urban heat island determination for Phoenix, Arizona. Journal of Applied Meteorology, 43(3), 476-486.

Hinkel K.M., Nelson F.E., Alene A.E. and Bell J.H., 2003. The urban heat island in winter at Barrow, Alaska. International Journal of Climatology, 23(15), 1889-1905.

Huang L., Li J., Zhao D. and Zhu J., 2008. A fieldwork study on the diurnal changes of urban microclimate in four types of ground cover and urban heat island of Nanjing, China. Building and Environment, 43(1), 7-17.

Ichinose T., Shimodozono K. and Hanaki K., 1999. Impact of anthropogenic heat on urban climate in Tokyo. Atmospheric Environment, 33, 3897-3909.

Iino A. and Hoyano A., 1996. Development of a method to predict the heat island potential using remote sensing and GIS data. Energy and Buildings, 23(3), 199-205.

Jáuregui E., 1997. Heat island development in Mexico City. Atmospheric Environment, 31(22), 3821-3831.

Johnson G.T., Oke T.R., Lyons T.J., Steyn D.G., Watson I.D. and Voogt J.A., 1991. Simulation of surface urban heat islands under 'Ideal' conditions at night Part1: Theory and tests against field data. Boundary-Layer Meteorology, 56(3), 275-294.

Kato S. and Yamaguchi Y., 2005 Analysis of urban heat-island effect using ASTER and ETM+ Data: Separation of anthropogenic heat discharge and natural heat radiation from sensible heat flux. Remote Sensing of Environment, 99 (1-2), 44-54.

Kalma J.D., Johnson M. and Newcombe K.J., 1978. Energy use and the atmospheric environment in Hong Kong: Part II. Waste heat, land use and urban climate. Urban Ecology, 3(1), 59-83.

Kalnay E. and Cai M., 2003. Impact of urbanization and land-use change on climate. Nature, 423, 528-531.

Kawashima S., Ishida T., Minomura M. and Miwa T., 2000. Relations between surface temperature and air temperature on a local scale during winter nights. Journal of Applied meteorology, 39(9), 1570-1579.

Khan S.M. and Simpson R.W., 2001a. Effect of a heat island on the meteorology of a complex urban airshed. Boundary-Layer Meteorology, 100(3), 487-506.

Khan S.M. and Simpson R.W., 2001b. Simulation of mixing depths incorporating the urban heat island effect. Environmental Modeling and Assessment, 6(3), 183-193.

Kidder S.Q. and Wu H.T., 1987. A multispectral study of the St. Louis area under snow-covered conditions using NOAA-7 AVHRR data. Remote Sensing of Environment, 22(2), 159-172.

Kim Y.H. and Baik J.J., 2002. Maximum Urban Heat Island Intensity in Seoul. Journal of Applied Meteorology, 41(6), 651-659.

Kim Y.H. and Baik J.J., 2004. Daily maximum urban heat island intensity in large cities of Korea. Theoretical and Applied Climatology, 79(3-4), 151-164.

Kimball B.A., Jackson R.D., Nakayama F.S., Idso S.B. and Reginato R.J., 1976. Soil-heat flux determination: Temperature gradient method with computed thermal conductivities. Soil Science Society of America Journal, 40(1), 25-28.

Kłysik K. and Fortuniak K., 1999. Temporal and spatial characteristics of the urban heat island of Łódź, Poland. Atmospheric Environment, 33(24-25), 3885-3895.

Kolev I., Savov P., Kaprielov B., Parvanov O. and Simenov V., 2000. Lidar observation of the nocturnal boundary layer formation over Sofia, Bulgaria. Atmospheric Environment, 34(19), 3223-3235.

Kuttler W., Barlag A.B. and Robmann F., 1996. Study of the thermal structure of a town in a narrow valley. Atmospheric Environment, 30(3), 365-378.

Lam J.C. and Li, D.H.W., 1996. Correlation between global solar radiation and its direct and diffuse components. Building and Environment, 31(6), 527-535.

Landsberg H.E., 1979. Atmospheric changes in a growing community (the Columbia, Maryland experience). Urban Ecology, 4(1), 53-81.

Lemonsu A. and Masson V., 2002. Simulation of a summer urban breeze over Paris. Boundary-Layer Meteorology, 104(3), 463-490.

Leung Y.K., Yeung K.H., Ginn E.W.L. and Leung W.M., 2004. Climate Change in Hong Kong. Hong Kong Observatory, HKSAR, Technical Note No. 107.

Lim Y.K., Cai M., Kalnay E., Zhou L., 2005. Observational evidence of sensitivity of surface climate changes to land types and urbanization. Geophysical Research Letters, 32, L22712, doi:10.1029/2005GL024267.

Lo C.P., Quattrochi D.A. and Luvall J.C., 1997. Application of high-resolution thermal infrared remote sensing and GIS to assess the urban heat island effect. International Journal of Remote Sensing, 18(2), 287-304.

Magee N., Curtis J. and Wendler G., 1999. The urban heat island effect at Fairbanks, Alaska. Theoretical and Applied Climatology, 64(1-2), 39-47.

Martilli A., 2002. Numerical study of urban impact on boundary layer structure: Sensitivity to wind speed, urban morphology, and rural soil moisture. Journal of Applied Meteorology, 41(12), 1247-1266.

Masson V., 2000. A physically-based scheme for the urban energy budget in atmospheric models. Boundary-Layer Meteorology, 94, 357-397.

Matson M., McClain E.P., McGinnis D.F. Jr. and Paitchard J.A., 1978. Satellite detection of urban heat islands. Monthly Weather Review, 106, 1725-1734.

Memon R.A, Leung D.Y.C. and Liu C., 2008. A review on the generation, determination and mitigation of urban heat island. Journal of Environmental Sciences, 20, 120-128.

Memon R.A., Leung D.Y.C. and Chun H.L., 2009. An investigation of urban heat island intensity (UHII) as an indicator of urban heating. Atmospheric Research, 94, 491-500.

Memon R.A., Leung D.Y.C. and Chun H.L., 2010. Effects of building aspect ratio and wind speed on air temperatures in urban-like street canyons. Building and Environment, 45, 176-188.

Mitchell J.M. Jr., 1961. The temperature of cities. Weatherwise, 14, 224-229.

Mochida A., Murakami S., Ojima T., Kim S., Ooka R. and Sugiyama H., 1997. CFD analysis of mesoscale climate in the Greater Tokyo area. Journal of Wind Engineering and Industrial Aerodynamics, 67-68, 459-477.

Montávez J.P., Rodríguez A. and Jiménez J.I., 2000. A study of the Urban Heat Island of Granada. International Journal of Climatology, 20(8), 899-911.

Ng M.C. and Wong M.S., 1998. Climatology of Ta Kwu Ling 1986-1997. Hong Kong Observatory Technical Note No. 94, Royal Observatory, Hong Kong. pp 44.

Nichol J.E., 1996. Analysis of the urban thermal environment with LANDSAT data. Environment and Planning B: Planning and Design, 23(6), 733 – 747.

Nichol J.E., 1998. Visualisation of urban surface temperatures derived from satellite images. International Journal of Remote Sensing, 19(9), 1639-1649.

Nichol J., 2005. Remote sensing of urban heat islands by Day and Night. Photogrammetric Engineering & Remote Sensing, 71(5), 613-621.

Nichol J. and Wong M.S., 2005. Modeling urban environmental quality in a tropical city. Landscape and Urban Planning, 73(1), 49-58.

Nichol J.E., 2009. An emissivity modulation method for spatial enhancement of thermal satellite images in urban heat island analysis. Photogrammetric Engineering & Remote Sensing, 75(5), 547-556.

Oke T.R., 1973. City size and the urban heat island. Atmospheric Environment, 7(8), 769–779.

Oke T.R., 1981. Canyon geometry and the nocturnal urban heat island: Comparison of scale model and field observations. International Journal of Climatology, 1(3), 237-254.

Oke T.R., 1982. The energetic basis of the urban heat island. Quarterly Journal of the Royal Meteorological Society, 108(455), 1-24.

Oke T.R., 1989. Boundary Layer Climates, London: Routledge, pp435.

Oke T.R., Johnson G.T., Steyn D.G. and Watson I.D., 1991. Simulation of surface urban heat islands under 'ideal' conditions at night part 2: Diagnosis of causation. Boundary-Layer Meteorology, 56(4), 339-358.

Parker D.E., 2006. A Demonstration that large-scale warming is not urban. Journal of Climate, 19(12), 2882-2895.

Parry M.L., Canziani O.F., Palutikof J.P., van der Linden P.J. and Hanson C.E., 2007. Climate Change 2007: Impacts, Adaptation and Vulnerability. Cambridge University Press, pp976.

Poreh M., 1996. Investigation of heat islands using small scale models. Atmospheric Environment, 30(3), 467-474.

Price J.C., 1979. Assessment of the urban heat island effect through the use of satellite data. Monthly Weather Review, 107, 1554-1557.

Rao P.K., 1972. Remote sensing of urban "heat islands" from an environmental satellite. Bulletin of American Meteorological, 53, 647-648.

Ripley E.A., Archihold O.W. and Bretell D.L., 1996. Temporal and spatial temperature paterns in Saskatoon. Weather, 51, 398-405.

Rosenzweig C., Solecki W.D., Parshall L., Chopping M., Pope Gregory and Goldberg R., 2005. Characterizing the urban heat island in current and future climates in New Jersey. Global Environmental Change Part B: Environmental Hazards, 6(1), 51-62.

Roth M., Oke T.R. and Emery W.J., 1989. Satellite-derived urban heat islands from three coastal cities and the utilzation of such data in urban climatology. International Journal of Remote Sensing, 10 (11), 1699-1720.

Roth M., 2007. Review of urban climate research in (sub)tropical regions. International Journal of Climatology, 27(14), 1859-1873.

Rozoff C.M., Cotton W.R. and Adegoke J.O., 2003. Simulation of St. Louis, Missouri, land use impacts on thunderstorms. Journal of Applied Meteorology, 42(6), 716-738.

Saaroni H., Eyal B.D., Arieh B. and Oded P., 2000. Spatial distribution and microscale characteristics of the urban heat island in Tel-Aviv, Israel. Landscape and Urban Planning, 48(1-2), 1-18.

Sabins F.F., 1997. Remote Sensing: Principles and Interpretation. Waveland Pr. Inc. pp512.

Sailor D.J. and Lu L., 2004. A top-down methodology for developing diurnal and seasonal anthropogenic heating profiles for urban areas. Atmospheric Environment, 38, 2737-2748.

Saitoh T.S., Shimada T. and Hoshi H., 1996. Modeling and simulation of the Tokyo urban heat island. Atmospheric Environment, 30(20), 3431-3442.

Sakakibara Y., 1996. A numerical study of the effect of urban geometry upon the surface energy budget. Atmospheric Environment, 30(3), 487-496.

Sang J., Liu H., Liu H. and Zhang Z., 2000. Observational and numerical studies of wintertime urban boundary layer. Journal of Wind Engineering and Industrial Aerodynamics, 87(2-3), 243-258.

Sarrat C., Lemonsu A., Masson V. and Guedalia D., 2006. Impact of urban heat island on regional atmospheric pollution. Atmospheric Environment, 40(10), 1743-1758.

Sham P., 1964. Total solar and sky radiation in Hong Kong, Hong Kong Observatory Technical Note No. 22, Royal Observatory, Hong Kong, pp14.

Stone B., 2007. Urban and rural temperature trends in proximity to large US cities: 1951-2000. International Journal of Climatology, 27(13), 1801-1807.

Streutker D.R., 2003. Satellite-measured growth of the urban heat island of Houston, Texas. Remote Sensing of Environment, 85(3), 282-289.

Takahashi K., Yoshida H., Tanaka Y., Aotake N. and Wang F., 2004. Measurement of thermal environment in Kyoto city and its prediction by CFD simulation. Energy and Buildings, 36(8), 771-779.

Terjung W.H. and Louie S.S.F., 1973. Solar Radiation and Urban Heat Islands. Annals of the Association of American Geographers, 63(2), 181-207.

Tong H., Walton A., Sang J. and Chan J.C.L., 2005. Numerical simulation of the urban boundary layer over the complex terrain of Hong Kong. Atmospheric Environment, 39(19), 3549-3563.

Tso C.P., 1996. A survey of urban heat island studies in two tropical cities. Atmospheric Environment, 30(3), 507-519.

Tumanov S., Stan-Sion A., Lupu A., Soci C. and Oprea C., 1999. Influences of the city of Bucharest on weather and climate parameters. Atmospheric Environment, 33(24-25), 4173-4183.

Unger J., Sümeghy Z. and Zoboki J., 2001a. Temperature cross-section features in an urban area. Atmospheric Research, 58(2), 117-127.

Unger J., Sümeghy Z., Gulyás Á., Bottyán Z. and Mucsi L., 2001b. Land-use and meteorological aspects of the urban heat island. Meteorological Applications, 8(2), 189-194.

Unger J., 2004. Intra-urban relationship between surface geometry and urban heat island: review and new approach. Climate Research, 27(3), 253-264.

Velazquez-Lozada A., Gonzalez J.E., Winter A., 2006. Urban heat island effect analysis for San Juan, Puerto Rico. Atmospheric Environment, 40, 1731-1741.

Voogt J.A. and Oke T.R., 1997. Complete urban surface temperatures. Journal of Applied Meteorology, 36(9), 1117-1132 .

Weng Q., Lu D. and Schubring J., 2004. Estimation of land surface temperature-vegetation abundance relationship for urban heat island studies. Remote Sensing of Environment, 89(4), 467-483.

Weng Q. and Yang S., 2004. Managing the adverse thermal effects of urban development in a densely populated Chinese city. Journal of Environmental Management, 70(2), 145-156.

Wong N.H., Tay S.F., Wong R., Ong C.L. and Sia A., 2003. Life cycle cost analysis of rooftop gardens in Singapore. Building and Environment, 38(3), 499-509.

Wong N.H. and Yu C., 2005. Study of green areas and urban heat island in a tropical city. Habitat International, 29(3), 547-558.

Yamashita S., 1996. Detailed structure of heat island phenomena from moving observations from electric tram-cars in Metropolitan Tokyo. Atmospheric Environment, 30(3), 429-435.

Zhang Jiahua, Hou Yingyu, Li Guicai, Yan Hao, Yang Limin (2005). An analysis of diurnal and seasonal variations of Beijing heat island using satellite remote sensing and factor analysis methods. Science in China (Series D), Earth Sciences (35), 187-194 (in Chinese).